HIGH RESOLUTION X-RAY SCATTERING STUDY OF THE CHARGE
DENSITY WAVES IN QUASI-ONE-DIMENSIONAL MATERIAL $K_{0.3}MoO_3$

By

JUNQING ZHANG

A DISSERTATION PRESENTED TO THE GRADUATE SCHOOL
OF THE UNIVERSITY OF FLORIDA IN PARTIAL FULFILLMENT
OF THE REQUIREMENTS FOR THE DEGREE OF DOCTOR OF PHILOSOPHY

UNIVERSITY OF FLORIDA

1993

ACKNOWLEDGMENTS

I would like to thank my advisor, Stephen E. Nagler. Without his supervision and continuous support, this work would not have been possible. The help offered by him during the process of writing this dissertation is greatly appreciated. I would like to thank him for not only being a teacher in my scientific research, but also in many aspects of my life.

The help from Stuart E. Brown can not be overstated. His expertise in charge density waves has given me great confidence in pursuing this work.

Jingfei Ma helped me a lot taking some of the data. With his company, numerous days in Brookhaven were made enjoyable.

I would like to thank Richard Adler for his technical assistance to my research. His computer knowledge provided big help to the writing of this thesis.

Robert Shannon, Jr. helped me greatly to become familiar with the lab. His kindness and patience deeply impressed me.

I thank my wife for her support in all aspects. She is always there when I need help. She walked step by step with me through these many years. I dare not think what my life would have been like without her.

I thank the Lord for His unceasing love. May His
purpose in my life prevail.

TABLE OF CONTENTS

LIST OF FIGURES

vii

High resolution x-ray scattering experiments are
performed on the quasi-one dimensional material $K_{0.3}MoO_3$ to
study the disordering of the charge density waves in the
presence of an electric field at low temperatures. The
samples are cooled down from room temperature to low
temperatures under zero electric field. After a thermal
equilibrium is reached, a dc field is applied in the chain
direction. X-ray scattering profiles of a CDW peak are then
collected. It is found that the electric field causes a
simple broadening of the scattering lineshape in the chain
direction; while in a direction perpendicular to the chain,
it splits the profile into two small peaks, which can not be
fitted well with a lorentzian function, suggesting that the
CDW lattice forms a micro domain structure after application
of the field. Furthermore, the broadened lineshape in the
chain direction has the best fit using a lorentzian

function, indicative of a correlation effect. Qualitative agreement is obtained between the data and a theoretical model, which provides convincing evidence for the intrinsic nature of the lineshape change by an electric field, disapproving of a previous suggestion that the scattering lineshape change is simply due to the electrical contacts.

It is also found that the disordering kinetics of the CDW lattice depends strongly on temperature and the field strength. At a fixed temperature and an electric field, the disordering is well described by a percolation model which has been applied previously to random magnetic systems. For the first time, we discover a one to one correlation between the transient bulk electric current and the CDW lattice disordering after an electric field is applied. Very interesting kinetics is also observed after the polarity of the external field is changed. It is found that the scattering lineshape evolves to its own mirror image, and the total scattering inside a certain region in reciprocal space shows oscillations, the origin of which requires further studies.

CHAPTER 1
INTRODUCTION

About forty years ago, Peierls [1] predicted the
possibility of charge density waves (CDW) in one-dimensional
metals that have a partially filled conduction band. His
calculation shows that the valence electrons in such systems
could arrange themselves periodically in space at zero
temperature, and that the ionic lattice undergoes a small
distortion as required by charge neutrality. When a big
electric field is applied to such a system, the electrons
forming the CDW lattice move together, or in other words,
the whole block of electrons slides in the opposite
direction of the external electric field. The underlying
ionic lattice, on the other hand, oscillates near its
equilibrium position. It was shown by Fröhlich [2] that if
the electronic lattice is incommensurate with the ionic
lattice, it costs no energy to make the electronic lattice
slide because there is no preferred relative position
between the two lattices. Since electrons form electric
current when they move, Fröhlich predicted that an
incommensurate CDW system can be a perfect electrical
conductor. However, this is only true for the case of a
perfect crystal with no impurities. In practice, there

always exist different kinds of lattice defects and a crystal can never be made completely pure. These imperfections act as pinning centers to the electronic lattice and make it nonmovable unless an electric field larger than some threshold field is applied. Because of these pinning centers and a relatively simple electronic band structure, a CDW system has very rich unusual properties, some of which have been well studied and understood, some are yet to be understood. These properties include the non-Ohmic behavior above a threshold electric field as just mentioned, large dielectric constants, and many others. We will discuss some of them in Chapter 2.

Since Peierls made the prediction, many CDW materials have been found [3,4,5]. Most of them are quasi-one dimensional materials with a finite transition temperature T_p. While many properties of these materials are studied by electrical transport measurements [6,7,8], many investigators have taken advantage of the presence of the ionic lattice distortion to study the static and dynamic properties of the CDW lattice using structural probes, such as elastic x-ray scattering [9,10] and neutron scattering [11]. Optical reflectivity [12], photoemission [13] and many other experiments have also been done. CDW systems are shown to be describable by a two component order parameter $|\psi|e^{i\phi}$, corresponding to an XY Ising model [14]. The amplitude η is related to the number of electrons that

participate in forming the CDW lattice (as in the case a superconductor, there are always normal electrons at a finite temperature), and the phase ϕ shows how the electronic lattice orders in space. Scattering experiments can probe both the amplitude and the phase [14,15].

It is extremely interesting to study the change of the electronic lattice and its counter partner, the ionic distortion, when the external environment changes. One can change the temperature, pressure, or apply an electric field, or dope the crystal with various methods such as with different chemical elements or bombarding the crystal with high energy particles. One can also compare the results obtained on different materials to search for universal behaviors if any. It is certainly quite important for understanding this particular class of systems which possess a collective response.

In the present work, we performed high resolution x-ray scattering experiments to study the statics and kinetics of the CDW lattice deformation in the presence of an external electric field at low temperatures. Our results clarified the confusion in the explanation of the observed lineshape change in the CDW scattering peak profiles by an electric field, and showed that the lineshape change arises from intrinsic effects, pinning. We also found that the externally applied electric field breaks the CDW lattice into micro domains. During the kinetics study, we observed

a one to one correlation between the structural disordering of the CDW lattice and the transient of the bulk electric current. Our results suggest that the relaxation of a CDW system under the driving force of an electric field is very similar to that of a random magnetic system, and the CDW domains relax independently of one another.

The statics have been studied in previous experiments [16,17]. However, due to the way that the electrical contacts were made, the explanation of the observed results was controversial. We carefully did the contacts and obtained clear and convincing data that clarified the ambiguity and demonstrated the intrinsic nature of the observed lineshape change. In the meantime, our data showed the need for more theoretical and experimental investigations of the problem. For the kinetics study, previous experiments have mainly been transport measurements [18,19], with one primitive structural study [20], which built no link between the structural observation and the transport data.

I should point out that CDW is one of the important collective modes which have been well studied. Another system of this kind is superconductors. One of the differences between a CDW system and a superconductor is the way that the electric current is conducted: in a CDW system, all the localized electrons move together like one block; while in a superconductor, electrons form Cooper pairs, and

each pair acts as if it were one particle.(by "localized electrons", I mean those forming the CDW lattice. Strictly speaking, these electrons can move around some equilibrium positions.)

This dissertation is divided into six chapters. Chapter 2 talks about the properties of a CDW system and specifically, blue bronze ($K_{0.3}MoO_3$), which is the sample used in this work. Chapter 3 briefly discusses the fundamental principles of the x-ray scattering technique and makes a comparison between x-ray scattering and neutron scattering. The last part of chapter 3 talks about how x-ray scattering technique can be used to study CDW systems. Chapter 4 discusses the experimental setup and data acquisition procedures employed in this work. Chapter 5 discusses the results of the statics study and Chapter 6 presents those of the kinetics study. The last chapter summarizes the major conclusions of this work and the future work that are needed.

CHAPTER 2
CHARGE DENSITY WAVES IN GENERAL

In this chapter, fundamentals of charge density waves
are discussed: what is the physical origin of charge density
waves? what properties does a system with CDWs have? The
second half of the chapter discusses the special properties
of blue bronze, which is the material used for this work.
The chapter ends with a brief description of the motivation
of this work.

The Origin of the CDWs

A pure gas stored in a container will have a uniform
distribution after an equilibrium is reached. In the same
way, electrons in a normal metal will distribute themselves
uniformly, just as the ions in a solid. In these cases, the
number density of particles is constant throughout the
system. A charge density wave state in a solid is, however,
different from the above in the sense that the electrons
distribute themselves in a strange way and the number
density varies spatially like a sinusoidal wave, $n = n_0 \cdot \sin(\mathbf{Q} \cdot \mathbf{r} + \phi)$. Such a state has been observed in many quasi-one

dimensional systems. But what is the physical origin for such a state?

It is well known that in a normal metal, unless an electron's wave vector **q** is very close to a Bragg plane, its energy in a non-degenerate case differs from that of an electron of the same wave vector in a free space only within the second order of the ionic potential. However, if the electron's wave vector is near a Bragg plane **K**/2, where **K** is a reciprocal space lattice vector, then the energy of the electron is given by [21]:

$$E = \frac{1}{2}(\varepsilon_q^0 + \varepsilon_{q\cdot K}^0) \pm [(\frac{\varepsilon_q^0 - \varepsilon_{q\cdot K}^0}{2})^2 + |U_K|^2]^{1/2} \qquad (2\text{-}1)$$

where $\varepsilon_q^0 = \frac{\hbar^2 q^2}{2m}, \varepsilon_{q\cdot K}^0 = \frac{\hbar^2 (q-K)^2}{2m}$ are the energies of an electron in a free space with wave vectors **q** and **q-K** respectively, and U_K is the Fourier transform of the ionic potential given by the following:

$$U_K = \frac{1}{v} \int e^{-iK \cdot x} U(x) d^3 x \qquad (2\text{-}2)$$

where the integration is over a unit cell of volume v. If **q**=**K**/2, eqn. (2-1) becomes:

$$E = \varepsilon_q^0 \pm |U_K| \qquad (2\text{-}3)$$

Therefore, there is an energy gap of $2\Delta=2|U_K|$ near the Bragg plane **K**/2 for the energy levels of the electron. For a reason that becomes clear later, we write $|U_K|$ in the following form:

$$\Delta = \left| U_{K} \right| = \frac{1}{V}\int d^3x \ \psi^*_{K/2} U(\mathbf{x}) \psi_{-K/2} \tag{2-4}$$

where $\psi_{\pm K/2}$ are the wave functions of an electron of wave vectors $\pm K/2$, respectively, when the ionic potential does not exist (they are simply plane waves).

For simplicity, from now on, without affecting the major conclusions, we restrict ourselves to one dimensional case and suppose that we have an infinite chain of atoms with periodicity a. We now distort the lattice a little and study how the energy spectrum of the system changes due to the distortion. This evidently depends on what kind of distortion we do to the lattice. One simple case is to displace every rth atom a little from its equilibrium position. This will reduce the translational symmetry and the new unit cell constant becomes ra. Correspondingly, the reciprocal unit cell becomes

$$-\frac{\pi}{ra} < k < \frac{\pi}{ra} \tag{2-5}$$

Similar to the case where the addition of a periodic ionic potential to the free electron gas produces an energy band gap near the Bragg planes, the potential change (or the extra potential) introduced by the periodic distortion also opens band gaps in each old reciprocal unit cell $(-\pi/a, \ \pi/a)$ near the new Bragg planes $k_{\rho}=\pm\rho\pi/ra$ with $\rho=1,2, \ \ldots, r-1$ besides the big band gaps near $\pm\pi/a$ due to the original ionic potential. The small energy gap Δ_s at $\pm\rho\pi/ra$, similar to (2-4), is given by the following:

$$\Delta_s = \frac{1}{V} \int d^3x \ \Psi_{k\rho}^* \cdot \delta V(x) \cdot \Psi_{-k\rho} \qquad (2\text{-}6)$$

where $\Psi_{k\rho}$ is the wave function of the electrons in the case where no distortions exist, and $\delta V(x)$ is the change of the potential caused by the distortion.

In figure 2-1, the electrons filling the energy levels on one side of the breaks have lower energies than the free electrons of the same wave vector because of the new energy gaps at the breaks; those filling the levels on the other side of the breaks have higher energies due to the same reason. If the states on either side of one of the breaks are filled with electrons, the total energy of the electrons will not be affected to the first order of δV (see eqn. 2-3). But if such a break coincides exactly or very close to the Fermi wave vector, then the states whose energies are displaced downwards will be filled and those displaced upwards will be empty. The result of the distortion is then a net reduction of the energy. This implies that a one dimensional metal with a partially filled band (so that k_F is between 0 and π/a) is not stable since one can always find a value for r such that $\rho\pi/ra \approx k_F$. So the solid can always distort itself in a way to lower its total electronic energy. A pure one-dimensional metal is not stable. Here, we only discussed the case where the electron-electron interactions are very weak. Depending on the strength and the range of electron-electron interactions, and the detailed band filling, a one-dimensional electron gas
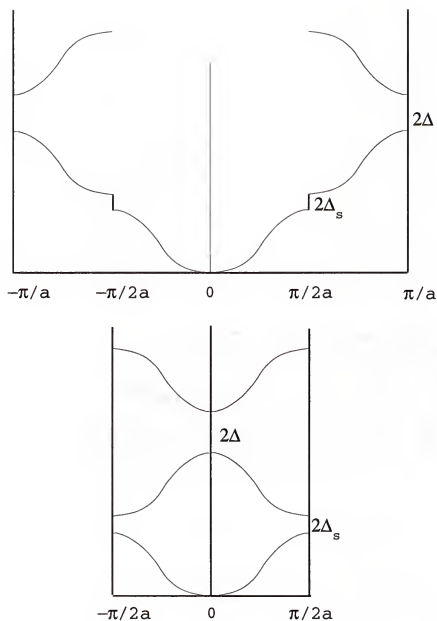
Figure 2-1   A periodic lattice distortion causes a new
band gap near the new Bragg planes $p\pi/ra$. The size of
the new gap depends on the change in the ionic potential.

exhibits an instability toward either a CDW, a spin density wave (SDW) or a superconducting ground state [22,23].

In a three dimensional system with very weak electron-electron interactions, the same argument of the above can be applied. However, the conclusion can be quite different because the band structure is now more complicated (bands along different wave vector directions can overlap thus the Fermi level can cross many bands, which makes the above argument very hard to use). In general, a three dimensional metal can be stable as is well known.

The above argument using electronic band structure is due to Peierls and the distortion is called Peierls distortion. It is worth noting that in order to produce the sub-band structure beyond the usual one, the distortion has to be periodic. Otherwise, there would be no new Bragg planes and the whole argument in the above would not apply.

Charge density waves are a special kind of distortion which normally takes place in quasi-one-dimensional materials. The electronic charge distribution is sinusoidal:

$$\rho = \overline{\rho} + \rho_1 |\eta| \cos[\mathbf{Q} \cdot \mathbf{r} + \phi(\mathbf{r})] \tag{2-7}$$

The uniform distribution $\overline{\rho}$ in (2-7) is due to the electrons that are not condensed in the crystal and $\eta e^{i\phi(r)}$ is the order parameter describing the distortion. In a real system, the periodicity $2\pi/Q$ may or may not be commensurate with the underlying ionic lattice. The commensurate case can be

understood using Peierls' argument discussed above. For the incommensurate case, one can think of it in the following way: if the Fermi surface still contains pairs of finite parallel portions even though these flat parts may not necessarily lie on the Bragg planes in general, there will exist some nesting vectors (the vectors that connect two parallel portions on the Fermi surface) to make the distortion possible. In many real quasi-one dimensional systems, the CDW is incommensurate along the chain direction and commensurate in the other directions [24].

From the above discussion, we see that the origin for the CDW formation in many quasi-one dimensional systems is the electronic energy reduction that arises from the distortion. In other words, the electrons try to lower their total energy by making the ions distort to produce the necessary small periodic potential. However, this is not always possible in a real system because there are other degrees of freedom which must also be taken into account. One of them is entropy, which always tries to eliminate any super-structure beyond the uniform distribution of the ionic charges at a finite temperature. A purely one-dimensional lattice is well known that it can not have any ordered superstructure beyond a uniform distribution, because the entropy term in the free energy is proportional to the macroscopic size of the system and can always kill the ordered structure. However, real systems are never purely

one-dimensional, and since the correlation length is very long along the chain direction, a moderate inter-chain interaction can make the ordered structure possible and this is the case. Such a transition has been observed in many materials by various methods: neutron scattering [25,26], NMR [27] and many other techniques. Of course, since the term involving entropy in the free energy becomes bigger as temperature gets higher, one can imagine that at a high enough temperature, this term will be dominant and the CDWs will die out. The transition temperature of $K_{0.3}MoO_3$ is $T_c=180K$ [28]; monoclinic TaS_3 has two CDW transitions at 240 K and 160 K [29,30]; $NbSe_3$ also has two transitions at 59 K and 145 K respectively [31,32,33]. The reason why TaS_3 and $NbSe_3$ have two transitions is that there are different chains in the crystals.

Besides the entropy effects on the CDWs, the other important degree of freedom is the elastic energy. This comes to play an important part in the CDW ordering since the ions are charge carriers and they favor staying at their equilibrium positions or keeping a uniform density distribution due to their mutual repulsive forces. Therefore, it costs elastic energy to move them away from their equilibrium positions. The electron-electron interactions are also against forming any superstructure. So in a real system, the situation is the total electronic energy competing with the above degrees of freedom: entropy,

elastic energy of the ionic lattice and of the electronic lattice. This normally ends up with a finite transition temperature, only below which CDWs are possible. Of course, there are also other things affecting the CDW ordering such as crystal lattice defects, impurities, etc. So real systems can be quite complicated.

Electron-Phonon Coupling

The above argument shows that by having a periodic lattice distortion of wave vector $2k_F$, the system electronic energy can be reduced. Therefore, the ionic lattice has an instability with respect to such a distortion. This instability is realized through electron-phonon coupling in real materials. When the temperature is above the transition temperature T_c, the distortion appears as a Kohn anomaly in the phonon spectrum on a particular phonon branch which is linearly coupled to the electron gas. Using a linear response function, the calculation using the Random-Phase-Approximation method yields the following result:

$$\omega_q^2 = \Omega_q^2 \left[1 - \lambda_q \chi_e(q)\right] \qquad (2.8)$$

where λ_q is the electron-phonon coupling constant, and $\chi_e(q)$ is the response function of the electron gas. For a purely one-dimensional lattice, $\chi_e(q)$ is peaked at $q=2k_F$ [21], which causes an anomaly in ω_q. When the temperature T

approaches T_c from above, ω_q decreases to zero at $2k_F$, which produces a new acoustic phonon branch, the phason branch.

Phasons, Amplitudons and Phase Slip

Lee et al. [34] studied theoretically the excitations of a CDW system in detail. Their results show that there are two excitations, namely, the phasons and the amplitudons. Inelastic neutron scattering experiments [35] find below T_c a new acoustic-like phonon branch near $2k_F$ in $K_{0.3}MoO_3$ (it is found that ω_q decreases but does not vanish at q=0). This is the phason branch, originated from the softened Kohn anomaly. Experiments [36,37] also find the amplitudon below T_c, the frequency of which at $q=2k_F$ does not soften in $K_{0.3}MoO_3$ at T_c, as expected for a mean-field-like second-order transition ($\omega_A^2 \propto (T_c^{MF} - T_c)$).

When a big electric field is applied in the crystal **b** direction, the CDW lattice slides. Transport measurements find that the sample volume dependence of the current oscillation amplitude can be explained if one assumes that the CDW lattice is composed of many independent domains in the presence of a big electric field and the CDW inside each domain oscillates at one frequency and the relative phase of neighboring domains is random [38] (we will discuss further what is meant by a CDW domain in Chapter 5). This assumption is reasonable since there are $N_s \approx \exp(A \cdot N_d)$

possible arrangements (a huge number) of the relative phase
of two neighboring domains, where N_d is the number of
domains in the system and A is a constant of order unity
[39]. In order to keep the current flow, condensed
electrons have to convert to free electrons on the contacts,
where wave fronts of the CDW lattice are lost at one contact
and produced at the other. Such a process is called phase-
slip process. It must occur on the contacts to keep the
current flow. It also releases some strain in the system
caused by lattice deformation by the applied field.

Properties of the CDWs

Systems that have CDWs have drawn tremendous interest
because of their rich electrical transport properties. As
discussed in the previous section, the CDW is a charged
lattice. When it slides, it generates electric current. It
was first pointed out by Fröhlich [2] that the
incommensurate CDWs can slide freely across the underlying
ionic lattice without costing energy when no barriers such
as pinning centers exist. Fröhlich superconductivity is
quite easy to understand since an incommensurate CDW lattice
has no preferred relative position to the ionic lattice,
thus it can move freely across the underlying ionic lattice
without costing any energy. In a real system, however,
potential barriers are always there and a CDW system has a

finite resistance. The most common barrier in CDW electric conduction is pinning centers. This has been studied by many groups both experimentally and theoretically [40,41,42]. In a quasi-one dimensional system, the condensed electrons distribute themselves sinusoidally along the unique chain direction. When an electric field is present, the electrons try to move opposite to the field direction, corresponding to changing the phase $\phi(\mathbf{r})$ in the charge density (2-7). The pinning centers, however, try to pin the phase at some locally favorable values. So, what one observes is the result of this competition. One can easily imagine that when the externally applied electric field is very weak, pinning will win and the CDWs can not slide; when the applied electric field exceeds some threshold value E_T, the pinning centers can no longer pin the CDWs and one will observe a contribution to the electric current from these condensed electrons. This idea is discussed by many groups theoretically as well as experimentally. One of the detailed theoretical discussions can be found in ref. 46, where Lee and Rice talked about what a dislocation in the CDW lattice does during the electric current conduction.

Besides the contribution to the electric current from the CDWs, the non-condensed electrons (also called quasi-particles or simply free electrons) in the system are the charge carriers. These free electrons are present because

of the transition from a valence band to the conduction band by thermal activation. The experimentally measured electric current is a sum of the free electron contribution and that of the CDWs when the external field exceeds the threshold field. Normally, the interaction between the free electrons and condensed electrons can be ignored. As we shall see later, the temperature dependence of the resistivity of the free electrons the same as in a normal semiconductor.

Figure 2-2 shows a dc current-voltage (I-V) curve which I measured at 35 K on a blue bronze sample. It is clear that when the voltage exceeds some value, the curve starts to deviate from a linear relation. This is the threshold voltage (or the threshold electric field, to be more general). When the applied electric field is stronger than this value, the CDWs begin to contribute to the electric current. However, as the voltage approaches another value (13 V in this case), the current starts to increase much more sharply, as if the sample was going to lose all its electric resistance. This is the so-called "switching process." Such a process is possible only at very low temperatures, and the way to approach such a state at different temperatures can be quite different. Figure 2-3 shows the I-V curve of a blue bronze sample on a LOG-LOG scale for four different temperatures [43]. The coexistence of a strongly damped regime and a free sliding regime at higher temperatures is not well understood.
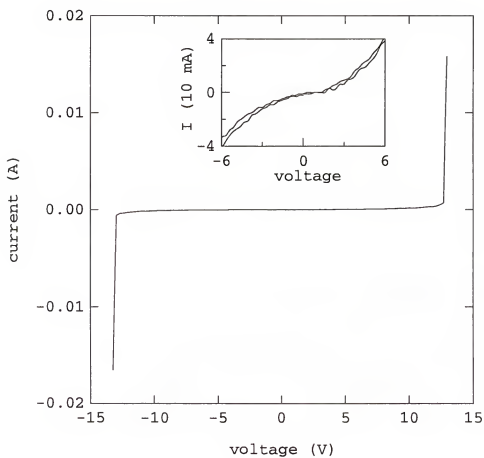
Figure 2-2 The DC I-V curve of a blue bronze sample
at 35 K. Inset: an enlarged view of the region near
the origin. Please note the hysteresis.
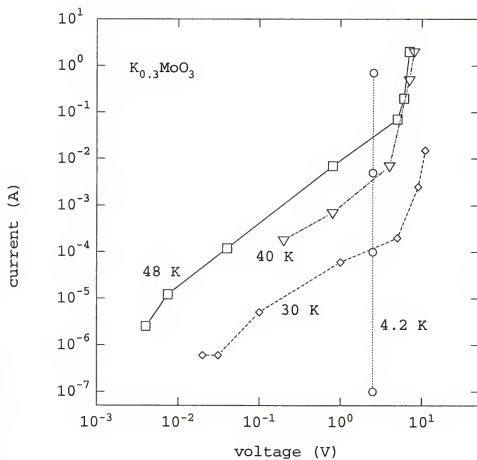
Figure 2-3   Current-voltage   characteristics of a blue
bronze sample at different temperatures.   Note the zero
differential resistance at 4.2 K, 40 K and 48 K.   (from
ref. 41)

Activation Behavior

Fleming et al. [44] studied the temperature dependence of the CDW current under the assumption as mentioned earlier that there is no coupling between the CDWs and the free electrons. Their result was shown in figure 2-4. Also plotted is the temperature dependence of the current due to the free electrons under the same dc electric field. It is obvious that the CDWs are not quite different from the free electrons as far as the temperature dependence of their electric currents is concerned. They both show a thermally activated behavior. It is easy to understand the case of the free electrons: the origin is interband transition by thermal energy as in a normal semiconductor (in fact, since the order parameter and therefore the Peierls band gap varies with temperature above 90 K, even the free electrons should not have a thermal activation behavior. However, since blue bronze is a dirty system, possessing many energy levels because of the lattice defects, activation behavior is always observed in this material). For the condensed electrons, however, the observed activation behavior is not easy to understand since they form a long-range-ordered lattice. If all the condensed electrons participate in the transition, it will be impossible to still keep the long range order. In fact, even if only a small portion of the
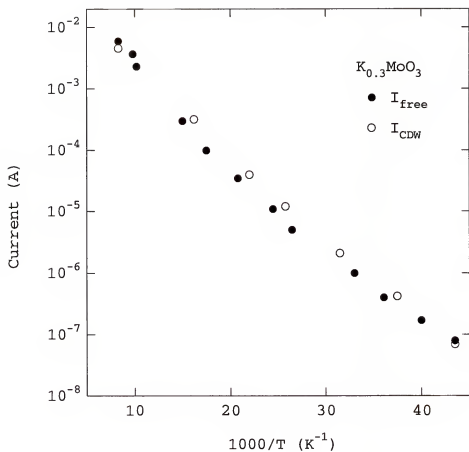
Figure 2-4   Temperature dependence of the CDW and
the quasi-particle current at a fixed bias voltage
in a blue bronze sample. (from ref. 44)

condensed electrons get activated, the long range would be destroyed.

Therefore, it makes little sense that the number of condensed electrons N_{CDW} changes with temperature. Many experiments have been done to investigate this issue and the results suggest that N_{CDW} does not change for a wide range of temperatures. For instance, electron diffraction experiment carried out by Wang et al. [45] strongly suggests that in TaS$_3$ which has its CDW transition temperature $T_c \approx 240$ K, N_{CDW} remains constant for all temperatures below 200 K. Therefore, we are confronted with two experimental results that seem to yield opposite conclusions: Fleming's results seem to suggest that N_{CDW} depends on temperature in the same way as the free electrons, while other experiments suggest N_{CDW} is temperature independent over a wide range below the transition temperature. Currently it is believed that N_{CDW} does not depend on temperature if it is way below the transition temperature and that the seemingly temperature dependent behavior of N_{CDW} observed by Fleming et al. is actually due to the temperature dependence of the CDW sliding velocity, which is proportional to the CDW current [27,46].

Current Oscillations

One of the famous discoveries in CDW transport measurements is the observation of distinct oscillations in

NbSe$_3$ [47]. This is commonly referred to as narrow-band-
noise (NBN). If one applies a dc electric current along the
chain direction of the sample by a current source, one will
find oscillations in the voltage output across the sample.
Furthermore, for every dc current value, there is a well
defined fundamental frequency in the ac voltage response.
If one plots the current and the corresponding fundamental
frequency, one gets a linear correlation. Figure 2-5 shows
the results measured at 42 K on NbSe$_3$ by Zettl and Gruner
[48].

The oscillations are believed to result from an overall
periodicity in the potential energy functional of the CDW.
So, when a constant field drives the condensed electrons to
move through the potential, the velocity is modulated in
time. There are two possible major effects that contribute
to this potential: one is the pinning potential of
impurities; the other is the phase slip near the contacts
which occurs on a periodic basis. The one that is dominant
depends on various things like sample geometry, the strength
and density of impurities, etc.

Memory Effects of CDW systems

CDW systems are interesting also because of their
fascinating memory effects. This was observed in the study
of electron irradiation effects on the CDW transport
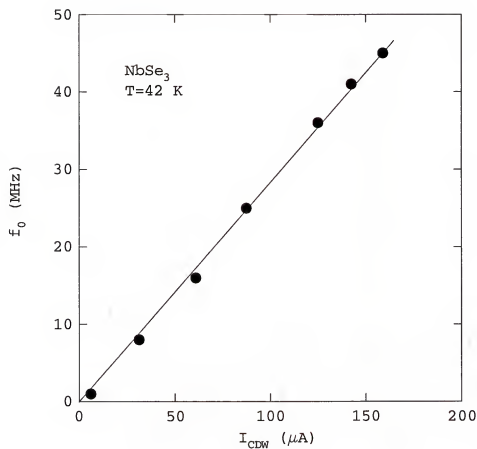
Figure 2-5   Fundamental frequency of the ac voltage response vs. the dc current level. The straight line is to show the linear correlation.

properties in blue bronze by Mutka et al [49]. They first cooled a blue bronze sample from about 120 K to 40 K at a constant rate and recorded the sample resistance during the process. Then they warmed the sample at the same rate back to 120 K after the temperature reached 40 K. They found that if the sample was kept at some intermediate temperature T_i for a few hours and then continued to cool down to 40 K, the sample seemed to "remember" the relaxation process at T_i when it was warming up. This phenomenon was observed both in the pure and in the electron-irradiated samples. Their data are shown in figure 2-6. Another important feature shown by the figure is the hysteresis effect. Such an effect is also observed in dc I-V curve measurements as shown by figure 2-2 (the inset). These properties of CDW systems strongly suggest that there exist many metastable states. During a thermal cooling/heating process or under the influence of an external electric field, the CDWs evolve from one metastable state to another. As will be discussed in chapter 5, structural data also support such an idea. Therefore, metastable states are generally believed to be one of the important features of a CDW system.

Other Properties of CDWs:

Besides the interesting properties briefly mentioned above, many other properties of the CDWs are also quite interesting and important, such as their response to an
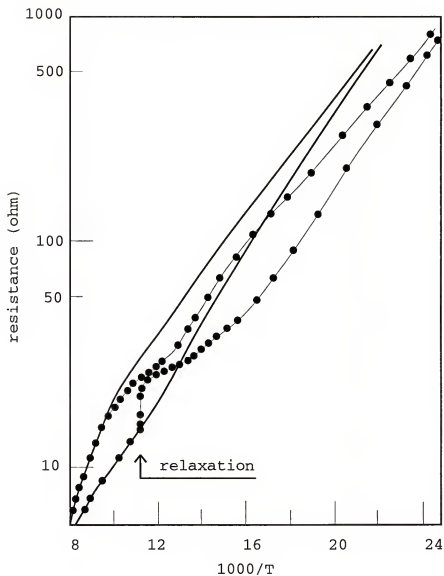
Figure 2-6 Resistance as a function of temperature during constant cooling and heating for an electron irradiated blue bronze sample. The continuous line shows the cycle with the temperature varying at a constant rate. The arrow shows the relaxation for several hours at 90 K.

external ac electric field [50,51]; what effects externally introduced impurities such as irradiation damages [52,53,54] or chemical doping cause to the ordering of the CDW superlattice and its transport properties [14]. Since these properties are not directly related to the present x-ray scattering experiments, I leave them out here.

Properties of $K_{0.3}MoO_3$

$K_{0.3}MoO_3$ is a model compound that exhibits CDW state at low temperatures. At room temperature, it is a metal with the crystal b* direction having the highest electric conduction. Below the Peierls transition temperature of 183 K, it becomes a semiconductor, like many other CDW materials. The electrical resistivity in figure 2-7 shows clearly such a transition [28]. Measurements of other properties such as Young's modulus also show the transition [55].

Crystal Structure of $K_{0.3}MoO_3$

$K_{0.3}MoO_3$ has a monoclinic crystal structure with a space group C2/m [56]. The unit cell parameters at room temperature are the following: a=18.249 $\overset{\circ}{A}$, b=7.560 $\overset{\circ}{A}$, c=9.855 $\overset{\circ}{A}$ and β=117.5°. A cartoon of the crystal structure is shown in figure 2-8. The unique direction is the crystal
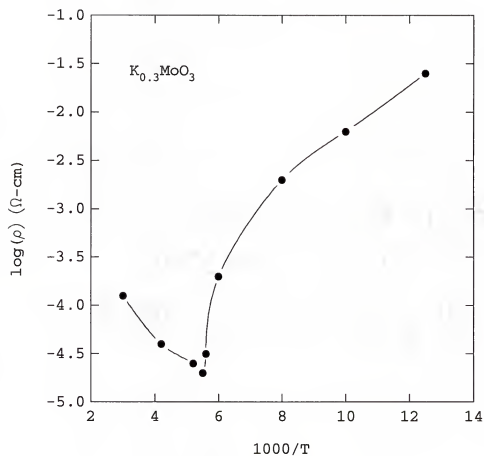
Figure 2-7 Temperature dependence of the electrical resistivity of blue bronze in the chain direction. (from ref. 28)

b direction, where chains of MoO_6 octahedra are connected
through corner sharing. This direction has the strongest
inter-atomic interactions. Figure 2-9 shows a cross section
view of the crystal structure in the **a-c** plane. On the
planes that are perpendicular to the **b*** direction, there is
a unique feature: it is a layered structure. The MoO_6
octahedra are connected in each layer and the K^+ ions sit
between the layers. The normal direction to the layers is
along the $2a*-c*$ direction. Because the ions are separated
farthest in this direction, it is not surprising that the
ionic and the electronic interactions are the weakest. Such
a crystal structure determines that this material is highly
anisotropic. Besides the **b*** and the $2\mathbf{a}*-\mathbf{c}*$ directions, the
third direction to characterize the crystal may be taken as
the $2\mathbf{a}+\mathbf{c}$ direction. To the order of magnitude, the ratio of
the CDW correlation lengths in these three directions (**b***,
$2\mathbf{a}+\mathbf{c}$ and $2\mathbf{a}*-\mathbf{c}*$) at a temperature much lower than T_c is
approximately 8:2:1 as we will see later.

<u>Band Structure of $K_{0.3}MoO_3$</u>

The high anisotropic crystal structure of $K_{0.3}MoO_3$ makes
it a very good one-dimensional material. Its electronic
band structure has been calculated by Wangbo et. al. [57].
Their results are shown in figure 2-10. It is clear that it
has two nearly degenerate conduction bands. With three free
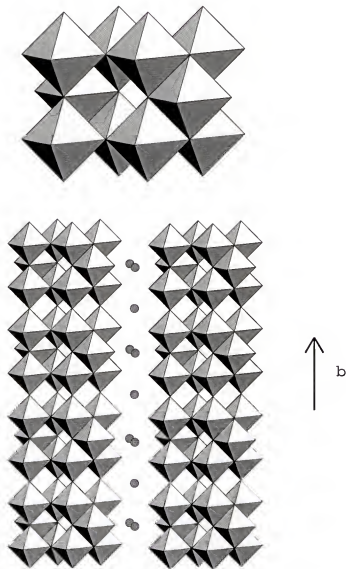
Figure 2-8   Crystal structure of blue bronze: The top
is a unit cell, consisting of ten MoO$_3$ octehedra.   The
bottom shows the chain structure of the crystal in the
crystal b direction. ●: potasium ions.
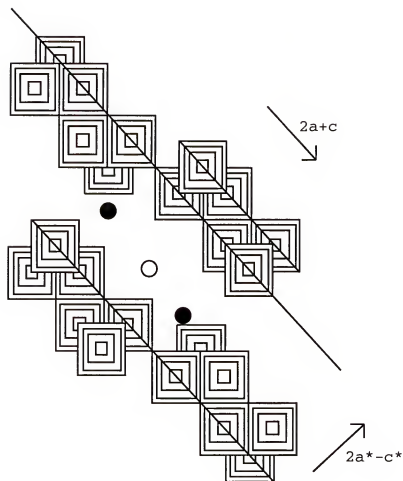
Figure 2-9   Cross section view of the crystal strcuture of blue bronze in the plane that is perpendicular to the chain direction, the **a-c** plane.

electrons in a unit cell (donated by the K atoms), their
calculation shows that the Fermi energy E_f is 0.012 eV below
the bottom of the third band as shown by the figure. This
is believed to be crucial to explain the temperature
dependence of the distortion wave vector of the CDWs that
form below the Peierls transition temperature, because the
magnitude of this distortion vector is just twice the Fermi
wave vector, which solely depends on the number of electrons
in the conduction band(s) by the following:

$$N = 2 \times \int_{-k_f}^{k_f} \frac{2\,b\,dk}{2\pi} \qquad (2-9)$$

where N is the number of electrons in the conduction bands
per unit cell, which is three for the present case. The
factor 2 in front of the integral on the right hand side
takes care of the fact that for blue bronze, there are two
conduction bands. Eqn. (2-9) gives the distortion wave
vector magnitude $q_b = 2k_f = \frac{3}{4}b^*$. This says that the CDW

lattice is commensurate with the underlying ionic lattice.
However, this is not the case in reality since such a
calculation assumes a perfect stoichiometry which does not
happen experimentally due to potassium deficiency in the
crystals.

<u>Motivation</u>

The present work is performing x-ray scattering
experiments to study the role of an externally applied
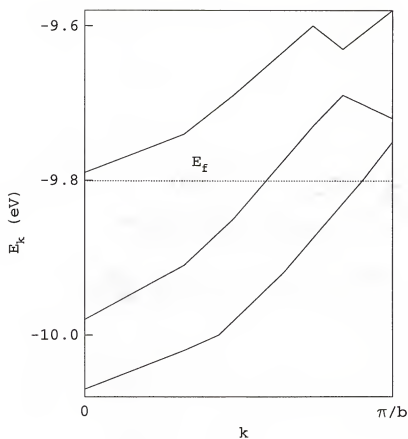
Figure 2-10 The three lowest bands of $Mo_{10}O_{30}$ in the b* direction. Note that the Fermi level is just below the bottom of a third band when there are three electrons in a unit cell as in $K_{0.3}MoO_3$. (from ref. 57)

electric field in the CDW lattice disordering. At the time when this work was proposed, a few similar experiments had been done to investigate this important phenomena. It has been found that at low temperatures, an electric field applied along the unique one-dimensional direction broadens the CDW scattering peak profile and, in some occasions, there is also a peak position shift in the transverse direction [16,58], which depends on the polarity of the applied field. Although short range order has been suggested [17] to explain such a phenomena, it is also suggested that the change of the CDW peak lineshape is caused by the inhomogeneity in the electric field [16]. The argument is the following: many of these experiments used electrical contacts applied on the surface of the crystals. Since these materials have a highly anisotropic electrical conductivity tensor, the current flow inside the crystals is inhomogeneous as shown by Figure 2-11. Since different parts of the crystal possess different electric current, or in other words, the CDW sliding velocity varies in space inside the crystal, this causes a spatial distribution of the CDW peak wave vector and a shift of the peak position [16,58].

The above argument attributes the observed peak broadening and position shift to extrinsic effects, and ignores any possible intrinsic origin for the observed lineshape change. However, this should be explored further
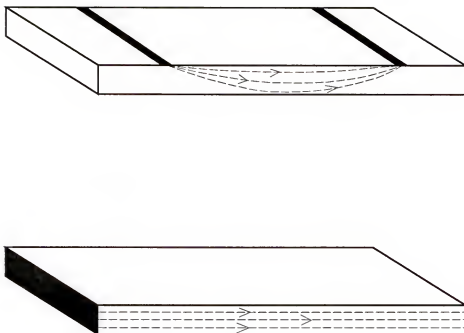
Figure 2-11   Application of electrical contacts on the surface of the crystal causes inhomogeneous flow of the electric current. The question is: if the contacts can be made such that the current flow is uniform (bottom), is there still change in the scattering spectra?

to answer the open question: does the lineshape change have any intrinsic nature or does it completely arise from extrinsic effects such as contact nonuniformity? In other words, if we could make the electrical contacts such that the electrical current flow inside a crystal is completely uniform, would an applied electric field still cause a change in the CDW peak lineshape? Our results demonstrate that the answer is yes: the lineshape change due to an electric field is intrinsic! We also find that the CDW relaxation under an external electric field is very sensitive to both temperature and the strength of the applied electric field. It is very similar to the relaxation phenomena in random magnetic systems.

CHAPTER 3
X-RAY SCATTERING TECHNIQUE

In this chapter, the fundamental principles of X-ray
scattering technique are discussed in the frame work of
quantum mechanics. Also discussed is the information this
technique probes. Then, x-ray scattering is compared with
neutron scattering. The last part of the chapter discusses
how x-ray scattering can be used to study a CDW system.

X-ray Scattering Principles

X-rays are high energy photons. They are a propagating
electromagnetic wave, possessing an electric field and a
magnetic field. Therefore, they interact with charge
particles such as electrons and with a magnetic moment.
Classically speaking, a charge particle will be accelerated
by the electric field of the incident beam and emit
electromagnetic radiation of the same frequency according to
the laws of electrodynamics.

Now, consider a solid composed of ions at $\mathbf{r}_i$,
i=1,2,..., N. The core electrons of the ions can be assumed
to be localized at $\mathbf{r}_i$ to the first order approximation. The

Hamiltonian for these electrons in a quantized
electromagnetic field is the following [59]:

$$\mathcal{H} = \mathcal{H}_0 + \mathcal{H}_r + \mathcal{H}' \tag{3.1}$$

where,

$$\mathcal{H}_0 = \sum_i \frac{\mathbf{P}_i^2}{2m} + \sum_{ij} V(\mathbf{r}_{ij}) + \frac{e\hbar}{2(mc)^2} \sum_i \mathbf{s}_i \cdot (\nabla \phi \times \mathbf{P}_i),$$

$$\mathcal{H}_r = \sum_{k\lambda} \hbar\omega_k [C^+(k\lambda)C(k\lambda) + 1/2],$$

and

$$\mathcal{H}' = \frac{e^2}{2mc^2} \sum_i A^2(r_i) - \frac{e}{mc} \sum_i A(r_i) \cdot P - \frac{e\hbar}{mc} \sum_i \mathbf{s}_i \cdot [\nabla \times \mathbf{A}(r_i)] - \frac{e^3\hbar}{2m^2c^4} \sum_i \mathbf{s}_i \cdot [\dot{\mathbf{A}}(r_i) \times \mathbf{A}(r_i)]$$

$$= \mathcal{H}'_1 + \mathcal{H}'_2 + \mathcal{H}'_3 + \mathcal{H}'_4 \tag{3.2}$$

In the above, ϕ and $\mathbf{A}$ are the scalar and the vector
potentials of the incident beam respectively, P is the
momentum operator, and $\mathbf{s}$ is the spin of the electrons and V
represents the interactions between the electrons. C and C^+
are the annihilation and creation operator for photons.

The scattering cross section is readily obtained by
calculating the transition probability between the initial
and the final states induced by $\mathcal{H}'$. Suppose that before the
transition, there is one photon and the solid is at a state
|a> which is an eigenstate of $\mathcal{H}_0$ with energy E_a. After the
transition, the system is excited to a state |b> with a
photon $k'\lambda'$. The transition probability per unit time is
given by perturbation theory to the second order [60,61]:

$$w = \frac{2\pi}{\hbar} \left| < f|\mathcal{H}'|i> + \sum_n \frac{<f|\mathcal{H}'|n><n|\mathcal{H}'|i>}{E_i - E_n} \right|^2 \times \delta(E_i - E_f) \tag{3.3}$$

where, $|i> = |a,k\lambda>$, $|f> = |b,k'\lambda'>$; $E_i = E_a + \hbar\omega_k$, $E_f = E_b + \hbar\omega_{k'}$.

Putting in the expressions for $\mathscr{H}'$ yields the cross section [59]:

$$\left(\frac{d^2\sigma}{d\Omega dE}\right)_{\substack{a\to b\\ \lambda\to\lambda'}} = \left(\frac{e^2}{mc^2}\right)^2 \left|f_0 + f_m + f_{res} + f'\right|^2 \delta(E_a - E_b + \hbar\omega_k - \hbar\omega_{k'})$$

$$(3.4)$$

where,

$$f_0 = \left\langle b\left|\sum_j e^{i\mathbf{K}\cdot\mathbf{r}_j}\right|a\right\rangle \boldsymbol{\varepsilon}'\cdot\boldsymbol{\varepsilon} \tag{3.5}$$

$$f_m = -\frac{i\hbar\omega}{mc^2}\left\langle b\left|\sum_j \mathbf{s}_j e^{i\mathbf{K}\cdot\mathbf{r}_j}\right|a\right\rangle\cdot\boldsymbol{\varepsilon}'\times\boldsymbol{\varepsilon} \tag{3.6}$$

$$f_{res} = \sum_c \sum_{ij} \frac{\hbar^2}{m(E_a - E_c + \hbar\omega_k - i\Gamma_c)}\left\langle b\left|\left(\frac{\boldsymbol{\varepsilon}'\cdot\mathbf{P}_i}{\hbar} - i(\mathbf{k}'\times\boldsymbol{\varepsilon}')\cdot\mathbf{s}_i\right)e^{-i\mathbf{k}'\cdot\mathbf{r}_i}\right|c\right\rangle\cdot$$

$$\left\langle c\left|\left(\frac{\boldsymbol{\varepsilon}\cdot\mathbf{P}_j}{\hbar} + i(\mathbf{k}\times\boldsymbol{\varepsilon})\cdot\mathbf{s}_j\right)e^{-i\mathbf{k}\cdot\mathbf{r}_j}\right|a\right\rangle$$

$$(3.7)$$

$$f' = \sum_c \sum_{ij} \frac{\hbar^2}{m(E_a - E_c - \hbar\omega_k)}\left\langle b\left|\left(\frac{\boldsymbol{\varepsilon}\cdot\mathbf{P}_j}{\hbar} + i(\mathbf{k}\times\boldsymbol{\varepsilon})\cdot\mathbf{s}_j\right)e^{i\mathbf{k}\cdot\mathbf{r}_j}\right|c\right\rangle\cdot$$

$$\left\langle c\left|\left(\frac{\boldsymbol{\varepsilon}'\cdot\mathbf{P}_j}{\hbar} - i(\mathbf{k}'\times\boldsymbol{\varepsilon}')\cdot\mathbf{s}_i\right)e^{-i\mathbf{k}'\cdot\mathbf{r}_i}\right|a\right\rangle \tag{3.8}$$

where $\mathbf{K}=\mathbf{k}-\mathbf{k}'$ is the momentum transfer of the incident photon to the solid and it is also called the scattering vector; $\boldsymbol{\varepsilon}$ and $\boldsymbol{\varepsilon}'$ are the polarization vector of the incident photon and the scattered photon, respectively.

Thompson Scattering Cross Section

The first term f_0 (3.5) is due to the electric charge of the electrons. We suppose that the solid does not change its state after the scattering, i.e., |a>=|b> (elastic scattering) and that the unit cell of the solid can be

described by a Bravis lattice $\mathbf{R_l}=l\mathbf{a}+m\mathbf{b}+n\mathbf{c}$ plus a basis of p ions sitting at positions $\mathbf{d_\gamma}$ inside a unit cell, γ $=1,2,3,\ldots,p$. Then f_0 can be rewritten

$$f_0 = \left\langle a \left| \sum_j e^{i\mathbf{K}\cdot\mathbf{r}_i} \right| a \right\rangle = \sum_{j,\gamma} \exp[i\mathbf{K}\cdot(\mathbf{R}_j + \mathbf{d}_\gamma)]$$

$$= (1 + \sum_{\gamma=1}^{p} e^{i\mathbf{K}\cdot\mathbf{d}_\gamma}) \cdot \sum_j e^{i\mathbf{K}\cdot\mathbf{R}_j} = S(\mathbf{K}) \cdot \sum_j e^{i\mathbf{K}\cdot\mathbf{R}_j} \qquad (3.9)$$

$S(\mathbf{K})$ is called the structure factor. It depends on the symmetry of the solid. The sum can be simplified by writing the scattering vector $\mathbf{K}$ in terms of the unit cell vectors $\mathbf{a}^*$, $\mathbf{b}^*$ and $\mathbf{c}^*$ of the reciprocal space, $\mathbf{K}=x\mathbf{a}^*+y\mathbf{b}^*+z\mathbf{c}^*$:

$$\sum_j e^{i\mathbf{K}\cdot\mathbf{R}_j} = \sum_{lmn=0}^{N_1N_2N_3}\exp[i(2\pi lx +2\pi my + 2\pi nz)]$$

$$= \frac{1 - e^{i2\pi N_1 x}}{1 - e^{i2\pi x}} \cdot \frac{1 - e^{i2\pi N_2 y}}{1 - e^{i2\pi y}} \cdot \frac{1 - e^{i2\pi N_3 z}}{1 - e^{i2\pi z}}$$

$$= (-1)^{(N_1-1)x+(N_2-1)y+(N_3-1)z} \cdot \frac{\sin(\pi N_1 x)}{\sin(\pi x)} \cdot \frac{\sin(\pi N_2 y)}{\sin(\pi y)} \cdot \frac{\sin(\pi N_3 z)}{\sin(\pi z)}$$

f_0 is the dominant term in (3.4). If one only considers this term, the scattering cross section is given by $|f_0|^2$, or

$$\frac{d\sigma}{d\Omega' dE'} \propto |S(K)|^2 \cdot \frac{\sin^2(\pi N_1 x)}{\sin^2(\pi x)} \cdot \frac{\sin^2(\pi N_2 y)}{\sin^2(\pi y)} \cdot \frac{\sin^2(\pi N_3 z)}{\sin^2(\pi z)} \qquad (3.10)$$

In (3.9), we have assumed that all the ions are all perfectly localized without any spatial deviations. This is an oversimplified assumption since no real solids are static. Therefore the sum over γ in (3.9) should be replaced by an integral of the number density of electrons

in space, and the structure factor $S(\mathbf{K})$ becomes the following:

$$S(\mathbf{K}) = \int_{cell} dV \rho(\mathbf{r}) e^{i\mathbf{K} \cdot \mathbf{r}} \qquad (3.11)$$

where the "cell" means that the integration is over a complete unit cell and $\rho(\mathbf{r})$ is the charge density of the electrons in the solid (electron charge e has been set to be unity).

(3.11) shows that the structure factor $S(\mathbf{K})$ is just the Fourier transform of the electronic charge density! This is true in a general case where there exist different types of atoms in the solid. So, one can rewrite the charge density in (3.11) and obtain the following:

$$S(\mathbf{K}) = \sum_{n} \int_{cell} dV \rho_n(\mathbf{r} - \mathbf{d}_n) e^{i\mathbf{K} \cdot \mathbf{r}}$$
$$= \sum_{n} f_n e^{i\mathbf{K} \cdot \mathbf{d}_n}$$

where $\mathbf{d}_n$ is the position of the nth ion inside the unit cell, and $f_n = \int_{cell} dV \rho_n(\mathbf{r}) e^{i\mathbf{K} \cdot \mathbf{r}}$ is called the atomic scattering factor of the nth ion.

Finite Size Effects

The function $\dfrac{\sin^2(\pi N x)}{\sin^2(\pi x)}$ is sketched in figure 3-1 for N=20. It peaks sharply near the points x=integer. Therefore as long as the structure factor $S(\mathbf{K})$ does not vanish, the scattering cross section (3.10) has sharp peaks
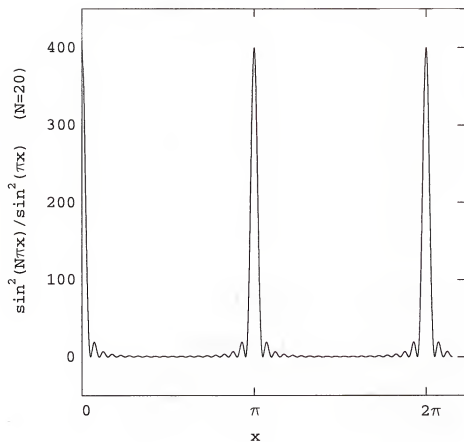
Figure 3-1   A sketch of the function of the
scattering cross section.. It sharply peaks at
positions where x is an integer.

at the reciprocal lattice points x=l, y=m, z=n, where l, m, n are all integers . The positions of these sharp peaks are determined by the crystal structure or., the unit cell vectors of the solid. At these peak positions, the scattering amplitude is mainly dependent on the structure factor (and the square of the crystal volume) through the following:

$$\frac{d\sigma}{d\Omega' \, dE'} = |S(K)|^2 \cdot N_1^2 \cdot N_2^2 \cdot N_3^2 \qquad (3.12)$$

For a real solid, N_1, N_2 and N_3 are very big numbers and the cross section behaves like a sum of differently weighted δ-functions centered at the reciprocal lattice points. When the momentum transfer K is not equal to a reciprocal lattice vector, the cross section drops dramatically. However, for a small single crystal, the finite size effect on the line width of the scattering peaks is not negligible. Ignoring other effects, solving the equation $\frac{\sin^2(\pi Nx)}{\sin^2(\pi x)}=N^2/2$ (assuming a big N) gives

x=0.422/N+integer

This yields that a crystal of sizes $L_1 \times L_2 \times L_3$ will have a half width at the half maximum intensity (HWHM) of

$$\Delta q_i = \frac{0.422a^*}{N_i} = \frac{2.65}{L_i}, \quad i=1,2,3 \qquad (3.13)$$

along the three crystal directions. For a 10μm cubic crystal, eqn (3.13) shows that the finite size effect will cause a line width 2.7×10^{-5} Å^{-1} (HWHM). Usually, a single crystal is not perfect but composed of several small grains

that orient slightly different from one another. Finite
size effects play a role in the scattering peak line width
in these situations.

<u>Strain Effects</u>

Another important source for the scattering lineshape
arises from the strain effects. This is very common as it
can arise from the growth or mishandling of the crystal.
Strain makes the lattice constants vary slightly from region
to region in the crystal. Putting it in another way, the
reciprocal space lattice deviates from a perfect Bravis
lattice, and the well defined peak positions in the
reciprocal space get smeared slightly thus the scattering
peak profile gets broadened. Mathematically, this can be
easily estimated with some simplifying assumptions. If we
assume a gaussian distribution for the lattice constants in
all three directions because of strain,

$$P(a_i) = \frac{1}{\sqrt{\pi}\xi_i} \exp[-(a_i - a_i^0)^2 / \xi_i^2] \qquad (3.14)$$

then the dot product of $\mathbf{a}_i$ and $\mathbf{a}_i^{0*}$ (equal to $2p_i$ below) will
also have a gaussian distribution accordingly,

$$P(p_i) = \frac{1}{\sqrt{\pi}\sigma_i} \exp[-(p_i - \pi)^2 / \sigma_i^2] \qquad (3.15)$$

With this, eqn. (3.10) will read like the following for a
Bragg peak $\mathbf{K} = (x\mathbf{a}_2^{0*} + y\mathbf{a}_2^{0*} + z\mathbf{a}_3^{0*})$ if one neglects the change
within each unit cell (assuming $S(\mathbf{K})$ is constant in (3.10)):

$$\frac{d\sigma}{d\Omega \cdot dE'} \propto \left|S(\mathbf{K}_0)\right|^2 \cdot \frac{1}{\pi^{3/2}\sigma_1\sigma_2\sigma_2} \cdot \int_v d^3p \cdot \frac{\sin^2(p_1N_1x)}{\sin^2(p_1x)} \cdot \frac{\sin^2(p_2N_2y)}{\sin^2(p_2y)}$$

$$\cdot \frac{\sin^2(p_3N_3z)}{\sin^2(p_3z)} \cdot \exp[-(p_1 - \pi)^2 / \sigma_1^2 - (p_2 - \pi)^2 / \sigma_2^2 - (p_3 - \pi)^2 / \sigma_3^2]$$

The above contains the following integral that is multiplied in three dimensions:

$$I = \frac{1}{\pi^{1/2}\sigma} \cdot \int dp \cdot \frac{\sin^2(Npx)}{\sin^2(px)} \cdot \exp[-(p - \pi)^2 / \sigma^2]$$

Letting u=px and approximating the quotient near the peak position l_0 by a Gaussian function which has the same maximum ordinate and the same area [62]:

$$\frac{\sin^2(Nu)}{\sin^2(u)} \rightarrow N^2 \exp[-N^2(u - l_0\pi)^2 / \pi] \tag{3.16}$$

Calling $(u-l_0\pi)$ by a new variable v, one has:

$$I = \frac{N^2}{\pi^{1/2}\sigma x} \int dv \exp[-\frac{N^2}{\pi}v^2 - \frac{(l_0\pi + v - \pi x)^2}{(\sigma x)^2}] \tag{3.17}$$

$$= \frac{N^2}{\sqrt{\omega}} \exp[-\frac{(x - l_0)^2}{\Gamma^2}]$$

where $\omega = 1 + \frac{(Nx\sigma)^2}{\pi}$ and $\Gamma = \sqrt{\frac{1}{\pi N^2} + \frac{\sigma^2 x^2}{\pi^2}}$. To the first order approximation, x can be set to be the peak position l_0 in ω and Γ, and the scattering cross section becomes,

$$\frac{d\sigma}{d\Omega \cdot dE'} \propto \left|S(\mathbf{K}_0)\right|^2 \prod_{i=1,2,3} \frac{N_i^2}{\sqrt{\omega_i}} \exp[-(x_i - x_i^0)^2 / \Gamma_i^2] \tag{3.18}$$

where i denotes the three directions, x_i^0 is the peak position for the strain-free case (which is the same when strain is present), and

$$\omega_i = 1 + \frac{(N_i x_i^0 \sigma_i)^2}{\pi} \text{ and } \Gamma_i = \sqrt{\frac{1}{\pi N_i^2} + (\frac{\sigma_i x_i^0}{\pi})^2} \tag{3.19}$$

It is clear from (3.19) that strain has two effects on the scattering lineshape: decreasing the peak amplitude and

broadening the profile. The broadening due to strain depends on the scattering wave vector as shown by (3.19). This makes it possible to distinguish the lineshape broadening from strain effects and that from finite particle size, which causes a width of $\frac{1}{\sqrt{\pi}N_i}$, independent of the scattering vector.

<u>Scattering from a Powder Sample</u>

A powder sample contains many small single crystals oriented in all possible directions (at least, this is an ideal case). These small crystallites scatter the incident photons independently or incoherently. The total scattering spectrum is the sum of all the individual scattering. However, in an actual scattering experiment, only a small number of crystallites can satisfy the Bragg condition (momentum transfer equal to a reciprocal lattice vector). Because of the random orientation of the little crystallites, the scattered photons will be distributed on a cone for each Bragg reflection with the cone center directly facing the incident beam [62]. Normally, if a single detector (such as a crystal scintillation detector) is used to collect the spectrum, the sample is rotated half the amount that the detector is rotated during data acquisition process in order to make sure that the scattered photons come from the same crystallites in the sample (this is often

called a θ-2θ rock). The scattering from a powder sample
is, of course, only a function of the magnitude of the
scattering vector **K**. As discussed earlier, for a fine
powder which consists of many very tiny single crystals, the
small finite size will cause a line width in the scattering
profile. Assuming a gaussian distribution for the sizes of
the small crystallites in a powder with the average size
being L, the finite size effect will cause the following
HWHM in the 2θ rocking curve [63,64]:

$$HWHM(2\theta) = \frac{0.47\lambda}{L\cos\theta} \tag{3.20}$$

which is called Scherrer equation [65,66]. It is basically
the same as eqn. (3.13), which, in terms of angles, is
simply, $HWHM(2\theta) = \frac{0.42\lambda}{L\cos\theta}$. The small difference in the

constant is due to the assumption of the size distribution
in deriving eqn. (3.14). Scherrer equation shows that a
10μm powder will have at least a width 0.0005° (HWHM) for a
peak at θ=45° on a Cu rotating anode x-ray source.

The overall signal is normally weaker for a powder
sample than a single crystal. It is difficult to use the
powder diffraction method alone to fully determine the
crystal structure of an unknown material since under normal
conditions, there are many Bragg peaks too weak to observe.
Furthermore, for a powder sample, scattering profiles of the
Bragg peaks having different Miller indices but the same
magnitude will overlap with one another. It is hard to get

very detailed information about an unknown material. Despite these shortcomings, powder diffraction remains a powerful technique in crystallography for preliminary studies because it is easier to do than single crystal scattering and it can indeed provide a lot of information.

The term f_m and f_{res} in (3.4) are related to the interactions between the incident photon and the magnetic moment of the electrons in the solid. A brief discussion of this important application of x-ray scattering is provided in APPENDIX A.

We have seen that x-ray scattering is a powerful technique for crystal studies. It provides information about an unknown solid such as the space groups and lattice parameters, the residual stress or the strain distribution in the crystal and the average grain size, and in some special cases, it can probe the magnetic ordering as well.

X-ray Scattering and Neutron Scattering

X-ray scattering is one of the important structural probes. Because its wavelength (a few Angstroms) is of the same order of magnitude as the lattice constants of many solids, it is widely used in crystal structural study. Besides x-rays, thermal neutrons are also often used for the same purpose. Table (3.1) lists the physical properties of an x-ray photon (Cu K_α^1 photon is used) and a thermal

neutron for comparison. These two kinds of particles are very different in nature and have very different interaction with a solid. It is natural to ask the following question: Under what circumstances one technique is better than the other? Table (3.2) shows the similarities and differences of these two scattering techniques. One nice thing about neutron scattering is that, as mentioned in table 3.2, it depends on the atomic number very weakly. This provides big contrast of light atoms. This is extremely important in studies of biological systems, which usually contain many hydrogen atoms (in reality, people take advantage of the fact that deuterium has a much bigger neutron scattering length than hydrogen and substitute some of the hydrogen atoms by deuterium to get an even better contrast).

X-ray Scattering and Charge Density Wave

X-ray scattering is a widely used technique to study CDW systems [10,67]. This is because below the CDW transition temperature, the ions distort from their equilibrium positions and form a superlattice structure under the requirement of the electronic energy reduction, as we discussed in Chapter 2. This superstructure which can be studied by x-ray scattering contains rich information about the CDW ordering, such as the degree of ordering, the length

Table 3.1 Physical Properties of an x-ray
photon and a thermal neutron (Z is the atomic number)

Properties	Cu K_α^1 photon	thermal neutron
energy	8048 eV	1-500 meV
charge	0	0
rest mass	0	937 MeV
magnetic moment	0	$-1.913\mu_B$
interaction with a solid	electromagnetic	nuclear interaction; magnetic
cross section/atom	~ 100 barns	~ 1 barn

Table 3.2 Comparison of x-ray and neutron scattering

Properties	x-ray scattering	neutron scattering
availability	Available in house	requires a reactor
flux intensity	high flux	low flux (10^4 smaller)
resolution ($\overset{\circ}{A}^{-1}$)	10^{-4}	10^{-3}
form factor angle dependence	sensitive to 2θ	insensitive to 2θ
Atomic number Z dependence	intensity $\propto Z^2$	very weak
magnetic study	not good [1]	good
isotope sensitive	no	yes
Phonon study	not applicable	yes

Note[1] x-rays can be used to study magnetic systems under
some special cases.

scale for the ordering, etc. The scattering structure
factor for an incommensurate CDW system has been derived by
Giuliani and Overhauser [68]. X-ray scattering experiments
allow one to obtain the CDW order parameter $|\eta|$ by measuring
the integrated intensity of a superlattice peak, which is
proportional to $|\eta|^2$. The scattering line width of a CDW
peak along a certain direction, on the other hand, is
related to the inverse of the CDW coherent length or the
domain size in that direction. Furthermore, the position of
a superlattice peak provides information about the number of
electrons in the conduction band [15], as discussed in
chapter 2.

The above discussion is widely applied below T_c. Above
T_c, the Kohn anomaly in the phonon spectrum gives rise to
diffuse scattering, which can be studied by x-ray or neutron
scattering. This can be understood by considering how the
diffuse scattering intensity is related to the electron
response function of a one-dimensional electron gas, which,
we know, is peaked at wave vector $2k_F$. The CDW response
function $\chi_\rho(\mathbf{q})$ is given by the following:

$$\chi_\rho(\mathbf{q}) = \frac{\chi_e(\mathbf{q})}{1 - \lambda_q \chi_e(\mathbf{q})} \tag{3.21}$$

and $\chi_\rho(\mathbf{q})$ is proportional to the displacement-displacement
correlation function $S(\mathbf{q})$, $S(\mathbf{q}) \propto \lambda_q k_B T \chi_\rho(\mathbf{q})$. This relates the
scattering intensity with $\chi_e(\mathbf{q})$ by the following:

$$I_d(\mathbf{q}) \propto |F_d(\mathbf{q})|^2 \frac{\chi_e(\mathbf{q})}{1 - \lambda_q \chi_e(\mathbf{q})} \tag{3.22}$$

which has an anomaly at the same wave vector as $\chi_e(\mathbf{q})$,
$q=2k_F$.

For a three dimensional system, eqn. (3.20) and (3.21) still hold, and $\chi_e(\mathbf{q})$ can also have a peak at some wave vector $\mathbf{Q}$. One mechanism to achieve this is through 'nesting' if there exist two parallel portions on the Fermi surface which would get superimposed on each other upon translation by the vector $\mathbf{Q}$ [69]. Such a property is possessed by the quasi-one-dimensional electron spectrum in the tight-binding approximation for simple chain structures [70]. This is the case in blue bronze, which has two electronic bands with wave vectors K_F^I and K_F^{II}, respectively. The two portions of the same curvature from each band can be nested by the wave vector $\mathbf{Q}$, whose component in the b* direction is equal to $K_F^I + K_F^{II}$, as shown in figure 3-2. Such a nesting produces an anomaly in $\chi_e(\mathbf{q})$ and makes possible a lattice distortion of wave vector $\mathbf{Q}=(1, K_F^I + K_F^{II}, -0.5)$, where the components of $\mathbf{Q}$ in the directions perpendicular to the chain are also determined by the nesting.

In this chapter, I did not discuss how a scattering experiment is actually accomplished such as how to get x-rays, how to perform an experiment, etc. These important aspects about x-ray scattering is discussed in the next chapter.

(a)
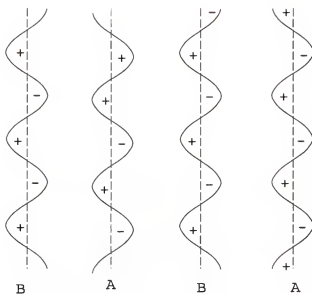
(b)
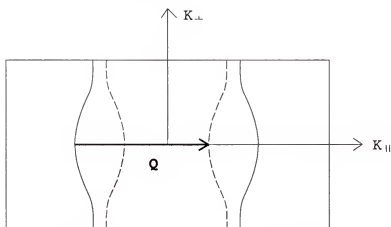
Figure 3-2 Coupling between the condensed
electrons on different chains. The two kinds
of CDWs (A and B) have band structures that
can be nested by a wave vector $\mathbf{Q}$ as shown in
(b), where the Fermi surfaces of the two bands
are shown in reciprocal space.

CHAPTER 4
EXPERIMENTS

In this chapter, experimental details are explained:
how the samples are prepared; what devices are used as well
as the sample mounting. The last part of the chapter
discusses the experimental procedures.

Sample Preparation

The samples used in this work are $K_{0.3}MoO_3$ (commonly
known as blue bronze). There are two commonly used methods
to grow the signal crystals. One is called electrocrystal-
lization, and the other, thermal gradient method [71].
Here, we briefly discusses the second method. In this
method, carefully mixed powders of K_2O and MoO_3 are put at
one end of a quartz tube which is sealed at both ends and
filled with inert gas (usually argon gas). This tube is
then put inside a furnace which is controlled in such a way
that the temperature of the quartz tube varies from one end
to the other during the process. The end where the powders
sit is kept at a high temperature (about 550 $^{\circ}$C). The
powders are melted and they slowly flow to the other end and

condense, forming single crystals. Figure 4-1 shows the set up schematically.

The samples prepared using such a method usually can not have a perfect stoichiometry since the powders made by manufacturers can not be make perfectly pure and the powders can never be mixed with a perfect stoichiometry. One can estimate the impurity concentration using electron paramagnetic resonance (EPR) or Auger Scanning Microscopy (ASM) methods. Under normal conditions, the major lattice defects are due to deviation from stoichiometry and attributed to the displacements of the Mo ions from the correct lattice points, with concentrations around ten parts in a million Mo sites [72]. The other type of defects is potassium deficiency, which is also caused by deviation from stoichiometry. The real chemical stoichiometry is more like $K_{0.3-x}MoO_3$ than $K_{0.3}MoO_3$. As discussed in eqn. (2-9), the Peierls distortion wave vector depends on the number of electrons donated by the K^+ ions, it is generally believed that this K^+ deficiency is the main reason why this material has incommensurate charge density waves [15].

X-ray Experimental Apparatus

A scattering apparatus usually contains a source of probing particles, a diffractometer and a sample. In this work, two kinds of x-ray generators are employed. The first
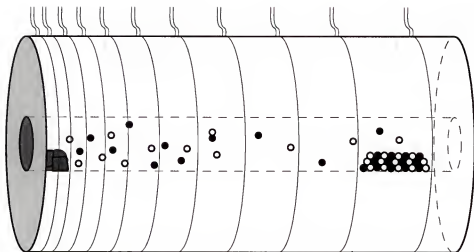
Figure 4-1 Schematic of the aparatus for crystal
growth using Temperature Gradient Method. Strictly
arranged heating coils are mounted on the furnace
and connected to an external current source.

one is a rotating anode source and the other is an accelerator.

Rotating anode source

A simple diagram in figure 4-2 shows how x-rays are generated from a rotating anode source. Briefly, hot electrons from a filament get speeded up by a strong electric field and hit a target. The common target materials are Cu, Co and Fe. In this work, Cu is used. For this case, some of the K-shell electrons of Cu are kicked out of the core level by the high energy electrons and become free electrons in the metal. This leaves a hole in the K-shell. When electrons in L_{III} shell $(2 \ ^2P_{3/2})$ fall into this hole, Cu $K\alpha^1$ x-rays are generated. If the electrons in L_{II} shell $(2 \ ^2P_{1/2})$ fill the hole in the K shell, Cu $K\alpha^2$ x-rays will be generated. Cu $K\alpha^1$ x-ray has a wavelength of 1.540 $\overset{\circ}{A}$ and Cu $K\alpha^2$, 1.542$\overset{\circ}{A}$. The flux ratio of these two characteristic lines of Cu is approximately 2:1. The characteristic lines of commonly used target materials and their relative intensities are all tabulated [73].

Chilled water is made flow through the anode to cool the copper target. In order to avoid locally overheating the target by the fast electrons, the anode is designed such that it can rotate at a high speed. Further cautions include that the whole housing where the anode sits is kept
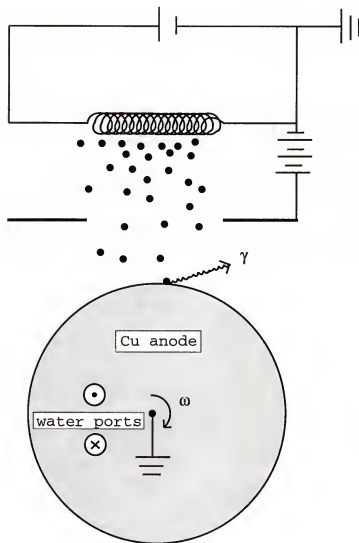
Figure 4-2 Schematic of a rotating anode x-ray source.
It mainly contains two parts: a metal target and a fast
electron gun.

at a very high vacuum to reduce the collisions between the high energy electron beam and air molecules in order to achieve a high x-ray flux and a small beam size.

Synchrotron Radiation

The idea of synchrotron radiation is quite simple: an accelerated charged particle emits photons. The electric field component of the emitted photon has the following relation with the acceleration of the charged particle:

$$E_x = \frac{-q}{4\pi\varepsilon_0 c^2 r} a_x (t - \frac{|\mathbf{R} - \mathbf{r}(t')|}{c})$$

where x represents the direction that is perpendicular to ($\mathbf{R} - \mathbf{r}(t')$), and the other quantities in the above are shown in figure 4-3, where the charged particle is an electron e⁻:
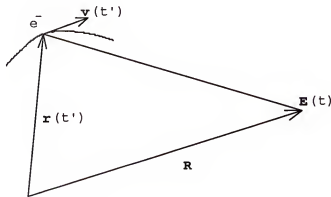
Figure 4-3

What is done in practice is that electrons are confined inside a circular accelerator after their energy is boosted to some value. Of course, the radiation flux emitted are proportional to the number of electrons in the orbit, which decreases in the course of time due to inevitable losses such as collisions between the electrons and the residual air molecules inside the accelerator besides the anticipated energy loss due to photon emissions. Radiation produced in this way is a continuous spectrum, and the flux slightly depends on the wavelength. To select the desired wavelength, one should use an extra monochromator to eliminate the higher order photons compared with the case of a rotating anode source where the flux peaks sharply at a few well defined photon energies. A common synchrotron source can provide a photon flux of $10^{12} \sim 10^{13}$ photons/mm^2/s. This is compared with a rotating anode source running at a power of 15 kW, which has flux of $10^8 \sim 10^9$ photons/mm^2/s. Besides this four orders of magnitude higher flux, another big advantage of synchrotron radiation is its small beam divergence, which assures a high system resolution. The small beam spot is another advantage. Of course, the tunability of photon energies in a synchrotron source makes possible many experiments that can not be done on a rotating anode source. Both sources are used in this work.

Scattering Set-up

An x-ray scattering set-up normally contains three
crystals: a monochromator, a sample and an analyzer. As
discussed earlier, the monochromator crystal picks up the
desired x-ray wavelength for the study. The analyzer
crystal is added in order to achieve a good system
resolution and cut down the background noise in the data.
Besides using an analyzer crystal, one can also use soller
slits, which are a series of parallel plates to collimate
the scattered beam. Of course, when the resolution is not
very critical or when a user needs a big intensity but can
live with a sloppy resolution, he does not have to use an
analyzer or soller slits. During the present work, Ge (111)
surface is used as the monochromator and the analyzer
crystals for all the statics studies and some of the
kinetics studies. Most of the kinetics data discussed below
are taken using two Si (111) crystals for the monochromator
crystals (synchrotron radiation is used) without an analyzer
because a multi-channel position sensitive detector (PSD) is
used instead of a single detector. The system resolution of
a scattering experiment depends on the divergence of the
incident beam when it reaches the sample if the wavelength
distribution can be narrowed down very well, which is
normally the case. The smaller the beam spot or the beam
divergence is, the better the system resolution. In order

to achieve a good resolution, four sets of slits are used to collimate the beam before it hits the sample. The first set of slits sit before the monochromator; the second set sit at the monochromator; the third set sit right after the monochromator and the last set sit right before the sample. For all the experiments done in this work, an extra set of slits are also put on the beam path: they are put after the sample but before the analyzer crystal. This set help to cut down the background noise and further improve the system resolution. The incident beam intensity is monitored by putting a detector right after the monochromator and measuring the flux scattered off a piece of mylar thin film when the rotating anode source is used. In the synchrotron case, an ion chamber is used to monitor the incident beam intensity. In either case, a four circle diffractometer is used to rotate the sample and the detector. It can change any of the three Euler angles of the sample. Counting the detector arm as another axis, such a four-circle diffractometer has four degrees of freedom. But a reciprocal peak with Miller indices h, k, l is completely determined with three degrees of freedom. This extra degree of freedom provided by the four-circle makes possible several modes to perform a scattering experiment. For the experiments in this work, Ω_0 mode is always used. In this mode, the Euler angle Ω is always equal to $-\theta$. A cartoon

of the set-up with an analyzer crystal is drawn in figure 4-4.

For the rotating anode source ($\lambda \approx 1.5$ Å), the Ge-Ge setup can achieve a resolution of full width at half maximum (FWHM) of 8×10^{-4} Å^{-1} along a transverse direction (perpendicular to $\mathbf{q}$) and 5×10^{-3} Å^{-1} in the radial direction (parallel to $\mathbf{q}$) at wave vector $\mathbf{q}=(14,2,-7)$. Along third direction, the resolution is much worse because it is out of the scattering plane. The beam spot is usually about 5 mm × 1 mm at the center of rotation (COR) of the diffractometer for the Ge-Ge set-up in our case and can be varied by the slits.

Sample Mounting

Rectangular-shaped samples are glued with GE varnish onto a sapphire rod which sticks above a copper holder. Figure 4-5 shows the sample holder schematically. As mentioned in Chapter 2, the major goal of the present work is to study the possible intrinsic effects in the CDW disordering by an electric field applied along the crystal chain direction. In order to apply an electric field to a sample, it has to be electrically insulated from the environment. For this reason, a sapphire rod is placed between the Cu base and the sample. The reason that a sapphire rod is chosen as the electrical insulator is
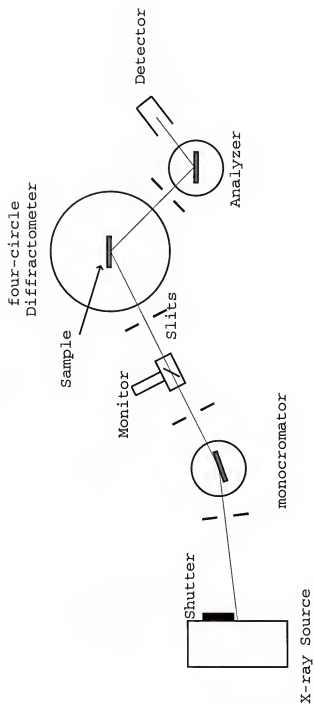
Figure 4-4   Schematic of an x-ray scattering experiment aparatus.
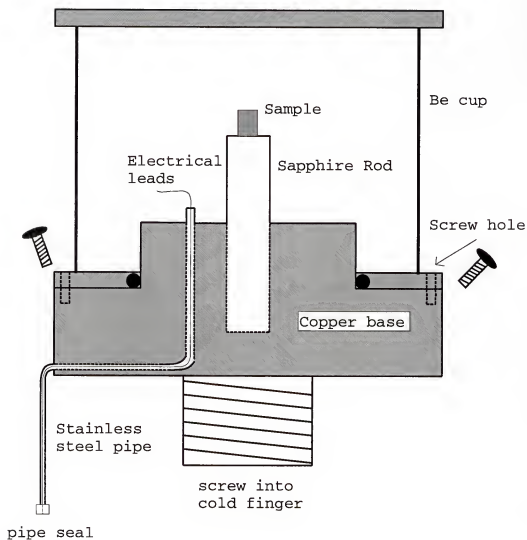
Figure 4-5 Sample mounting and electric field application. The Be cup is filled with He gas during an experiment. ● : Indium O-ring.

because it is also a good thermal conductor. This is also
very important to the success of the experiment because we
need to conduct away the Joule heat caused by the applied
electric field in order to get as close as possible a
temperature reading on the sample as well as a uniform
temperature inside the sample. A sensor is mounted near the
sample to monitor the sample temperature. The samples
studied are usually thin plates with a very narrow edge
touching the top surface of the sapphire rod. As we shall
see in Chapter 5, although the thermal conduction is not
excellent, it is pretty good since both the sapphire rod and
the copper wires (the electrical leads) can conduct away the
heat imposed by the applied field. In order to further
improve the situation and also to reduce the temperature
gradient within the sample, a Be cup filled with He gas is
used during the kinetics studies. This whole assembly is
mounted onto the cold finger of an APD Displex.

One big problem encountered in mounting the sample is
that a perfectly aligned sample at room temperature moves
out of the COR when it is cooled. This is because the
crystal has a quite different thermal expansion coefficient
than the material it is attached to. Moreover, the glue
used to connect these two has a different expansion
coefficient from either of them. These differences could
make the alignment very tedious if caution was not made. A
commonly used way to mount the sample to study the

reflection scattering peaks is to glue the sample onto the surface of a half-cylinder. This turned out to be a bad method for our experiments because the sample gets out of the center of rotation when the apparatus becomes cold. With our mounting method, the alignment gets greatly simplified due to the high symmetry of the sample holder: when the whole assembly (including the Displex center rod) thermally contracts at low temperatures, the sample moves a small amount mainly in the direction parallel to the Displex rod (not twisting around) and can be easily traced by the beam.

<u>Temperature Control</u>

The experiments are performed at low temperatures and the cooling device is a closed cycle He refrigerator driven by a compressor. A diagram of the refrigerator (Displex) is shown in figure 4-6. It is a conventional cooling machine. The basic principle is that the temperature of a compressed gas decreases when it expands to a vacuum. He gas is used because it can provide the lowest temperature in this mechanism because it has the lowest boiling temperature (4 K). The ultimate temperature the used device can reach is about 8 K and it depends on the size of the sample holder. To stabilize the temperature, a Lakeshore temperature controller (model 81-C) is used in connection with the
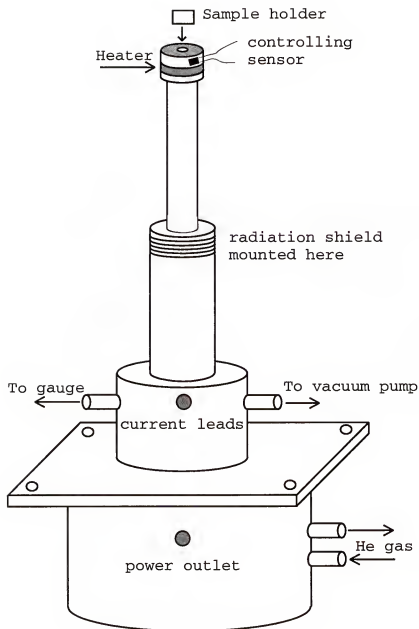
Figure 4-6 A schematic of the Displex used to cool the sample. It always works with an APD compressor during operations.

Displex assembly. The controller adjusts the input heating power to a resistor heater based upon the difference between the measured temperature and the set point (all temperature sensors used are silicon diode). The controlling temperature sensor is attached beside the heater on the cold finger of the Displex. The compressor is kept on during the measurement. This assembly can achieve a temperature stability of ± 0.5 K at the cold finger when it is at 10 K. The sample temperature is much more stable than ± 0.5 K. A typical value for it is ± 0.1 K. If He gas is used to help the thermal conduction, a temperature stability of 0.05 K can be easily achieved.

Experimental Procedures

Beam Collimation

Here, I only discuss Ge-Ge set-up. PG-PG set-up is the same except that the Ge crystals are replaced by highly oriented pyrolitic graphite crystals, for the monochromator and the analyzer, using the (001) planes. This causes the system resolution to get worse by about a factor of ten, but the scattering intensity increases by about the same factor.

The spectrum from the Cu rotating anode source, which is a superposition of a continuum and the characteristic lines of Cu, is first monochromated by a Ge (111) surface

which sits on a goniometer, which can be translated and rotated in many directions. Without any sample sitting on the diffractometer, which is a four-circle huber, the monochromatic beam is first focused on a fluorescent pad which gives out visible light when shone by x-rays. With the help of a telescope, the beam is aligned by moving the diffractometer, such that the beam center passes through the COR of the diffractometer. Then a piece of thick brass plate which has a very narrow slit at the center is put up at the COR. The huber is then again adjusted to make the portion of the beam with the highest intensity pass through the slit on the brass plate. When this part is done, the analyzer is then put up on the detector arm (2θ arm) and is adjusted to maximize the counts collected in the detector. A 2θ scan without a sample is shown in figure 4-7 when no analyzer is present and all slits are wide open.

After the beam is centered well, the first three sets of slits are done to improve the system resolution and to cut down the background. The order to do the slits is from the anode source to the sample to the detector. Figure 4-8 shows the same scan as in the previous figure but with an analyzer present. A much narrower peak profile is obtained. The two curves in fig. 5-8 were obtained respectively, with a non-collimated beam (all the slits open) and a well collimated beam. The smaller peak in the first curve results from the Cu $K\alpha^2$ characteristic line. For the

rotating anode setup used in this work, Cu $K\alpha^2$ can be cut down significantly by doing slits with the $K\alpha^1$ radiation unchanged. In fact, one can get rid of $K\alpha^2$ completely by slitting with a 20% down in the intensity of the Cu $K\alpha^1$ in our case. Of course, the longer the distance between the sample and the x-ray source, the easier to separate these two characteristic lines because they will be further separated in space.

We have carefully studied the static behavior of the lineshape change after an electric field is applied. By static, I mean that a thermal equilibrium has been reached phonemically, that is, no further change can be observed in laboratory time. We also studied the time dependence of the CDW lattice disordering. We call this kinetics study.

Static Data Acquisition Procedure

For the statics studies, Ge-Ge setup is exclusively used except otherwise specified. The sample is first studied in detail at room temperature to determine its lattice parameters and its orientation relative to the four-circle diffractometer. Then it is cooled down to low temperatures. After a thermal equilibrium is reached, scans of the superlattice peaks along different symmetry directions are carried out after an orientation matrix is
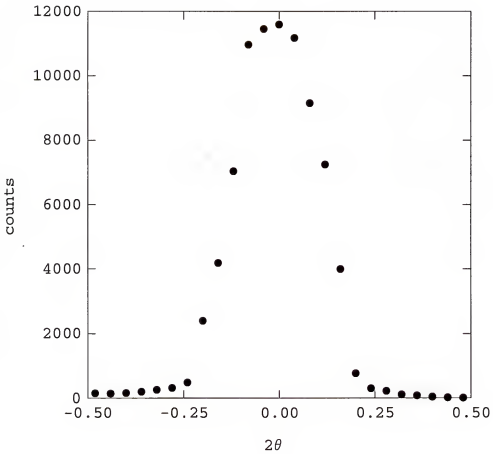
Figure 4-7 Twotheta scan profile without an analyzer.
No sample is put on the diffractometer. (A Ge (111)
single crystal is used as the monocromator).
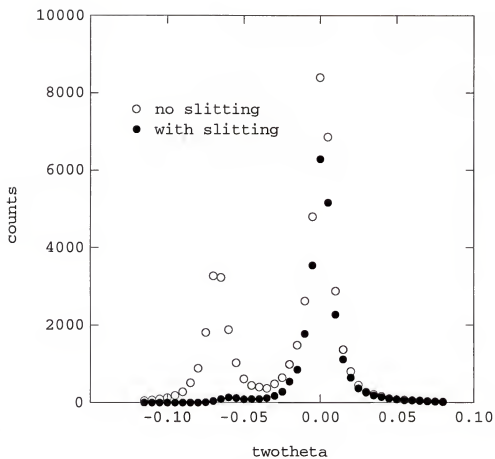
Figure 4-8 Twotheta scan with a Ge (111) analyzer. Note that doing slits can cut down Cu $K\alpha^2$ component substantially without affecting $K\alpha^1$ component much.

obtained at the same temperature using two Bragg peaks. A dc electric field is then applied along the crystal chain direction using a wide-wave function generator. Since the external electric field inputs a small heating power to the sample, the data are collected about half an hour later after the electric field was turned on (for some experiments, the field is turned off during data acquisition). When the scans are finished, the strength of the electric field is increased in some experiments. With each field value, the same scans are repeated. In some experiments, the field strength is kept constant and the field polarity is changed.

After all the x-ray data are taken, a dc I-V curve will be measured at the same temperature. The samples are then warmed up to room temperature.

Kinetic Data Acquisition Procedures

During the kinetics study, the samples are first studied using the setup described above. Then, before application of an electric field, the analyzer crystal is removed from the scattering apparatus and a silicon diode array PSD is put on the beam path after the sample in order to catch the fast change of the superlattice peak profile upon application of an electric field. Electric transport measurements are carried out simultaneously in order to

build any possible correlations between the structural change of the CDW lattice to the electrical transport properties of the samples.

The PSD is has 1024 channels, with a window of 2.705 cm long and 2.5 cm wide. During the experiments, it is set 80 cm away from the sample, spanning a 2θ angle of approximately $1.947°$. Figure 4-9 shows schematically how a scan spectrum collected by the PSD looks in reciprocal space. The diagram only shows two directions since the third direction has been integrated over as far as the signal is concerned. The ellipse in the figure represents the system resolution. During a scan, the ellipse moves approximately along the straight line in Fig. 4-9 and the detector (PSD) collects all the photons scattered into the region it passes (a straight line is a good approximation only near the peak position. In reality, the trace of the ellipse is a curve in reciprocal space). After a dc electric field is applied, the CDW peaks start to broaden and may also shift to one side of the peak position, and the number of photons that remain scattered into the scanning region of the PSD will become smaller and smaller as time goes by. Therefore, this number can reflect the disordering of the CDW lattice.

Typically, it takes about an hour for the sample to reach a thermal equilibrium after the cold finger of the
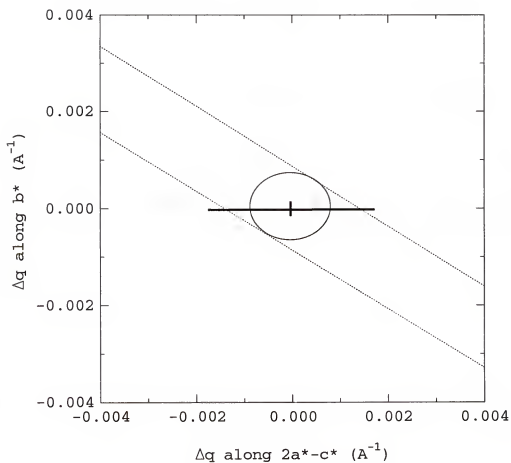
Figure 4-9 Schematic of the trace of a psd scan in reciprocal space. The ellipse is the resolution. A scan collects all the photons scattered into the region between the dotted lines.

Displex reaches the desired temperature in the case He gas is used. If no He gas is used to improve the thermal conduction, it could take up to four hours for the sample temperature to stabilize. This may depend on the temperature controller.

CHAPTER 5
RESULTS/DISCUSSION I - STATICS

This chapter discusses the lineshape change by an electric field. It deals with the static change only, namely, the final stage of the lineshape change of a scattering spectrum. The time dependent change of spectrum will be discussed in next chapter.

Zero Field Data

Quite a few samples have been studied in this work. As mentioned in chapter 4, the crystals are first studied at thermal equilibrium after cooling to low temperatures. Figure 5-1 shows the scan profile of a CDW peak along the chain (b*) direction of a single blue bronze crystal (all data shown below are taken on sample #1, except otherwise indicated), which has a mosaic spread of 0.01° (FWHM). The scan of a Bragg peak along the same direction is also shown in the figure for comparison. The temperature is approximately 35 K. It is clear that the superlattice peak has approximately the same widths as the Bragg peak in the chain direction The slightly narrower width of the superlattice peak is caused by the system resolution (and

Figure 5-1 Scan profiles of the CDW peak $(15, -\epsilon, -7.5)$ and of the Bragg peak $(14, 2, -7)$ in the b* direction. The temperature is 35 K. The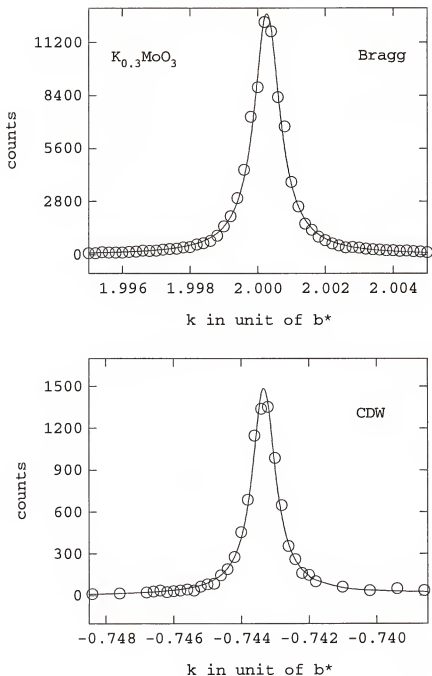 curves are fits using a lorentzian function. The CDW scan is zero field cooled data and the Bragg scan is under an electric field that is about 1/3 of the threshold field.

the finite grain size effect, which also affects the Bragg peak), as shown by Appendix E.

Figure 5-2 shows the peaks along the 2a*-c* direction, which is a direction that is perpendicular to the chain direction and to the layers. Contrary to the case in the crystal chain direction, the CDW peak now has a broader profile than the Bragg peak. Although the system resolution at the CDW peak position is worse than at the Bragg peak, quantitatively, the system resolution (and the finite-grain-size effect) alone can not account for the broader linewidth of the CDW peak (see appendix E), and there have to be other effects causing the difference. One possibility is that although the CDW lattice is long range ordered in the chain direction, it does not achieve a long range order in the (2a*-c*) direction. Other experiments [17] find that above 100 K, which is far below the transition temperature T_c=183 K, the system does not have a long range order. A similar situation is observed in previous experiments in $K_2Pt(CN)_4 0.3Br \cdot xH_2O$ (KCP) [26], where the incomplete transition in the transverse direction was believed to be due to the disorder of Br^- ions. However, in the present case, the temperature is 35 K and the system has been observed to be long range ordered at very low temperatures [20]. The failure to achieve a three dimensional long range order in this sample (#1) might be, similar to the case of KCP, due to disorders of the Mo^{4+} ions. As discussed in
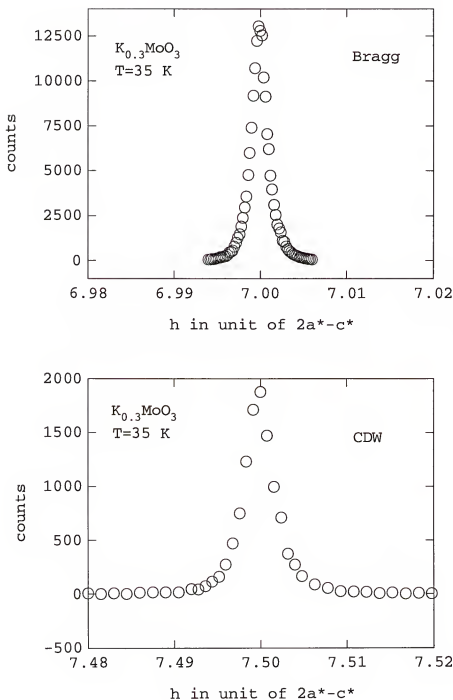
Figure 5-2 Scan profile of the CDW peak (15, -ε, -7.5) and that of the Bragg peak (14, 2,-7) along the (2a*-c*) direction under zero electric field.
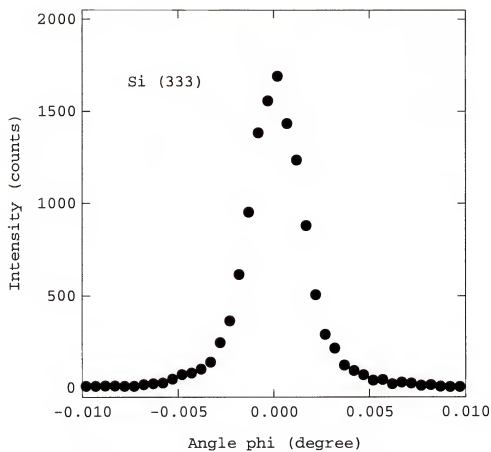
Figure 5-3 Phi rock of a Si (333) single crystal at
room temperature. The system setup is the same as in
figure 5-1.
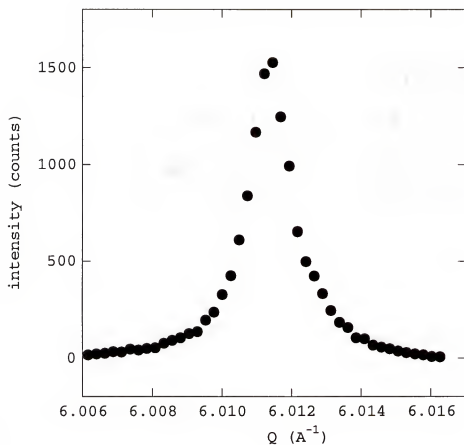
Figure 5-4   Radial scan of the (3,3,3) peak of a Si
single crystal. The system setup is the same as that
of figure 5-1.

chapter 4, disorders of the Mo^{4+} ions are one of the major defects in blue bronze crystals.

Having mentioned that, the widths of the scattering peaks, however, are mainly from the system resolution as shown in figure 5-3 and 5-4, where a ϕ rocking curve and a radial scan curve of the (333) peak of a perfect single crystal silicon ($Q\approx5.9$ $\overset{o}{A}^{-1}$) are plotted. The other factor that contributes to the widths of the peaks is the grain size. For example, in the longitudinal direction (// $\mathbf{Q}$), the Bragg peak (14,2-7) has a width of 9.3×10^{-4} $\overset{o}{A}^{-1}$ (see Appendix E), and the system resolution deduced from figure 5-4 in this direction is 7.0×10^{-4} $\overset{o}{A}^{-1}$. Subtracting these two widths in quadrature yields a grain size of 5.2×10^{3} $\overset{o}{A}$ in this direction (parallel to $\mathbf{Q}$). The CDW domain size is of the same order of magnitude as the grain size because the superlattice peaks have approximately the same widths as the Bragg peaks. For a Ge-Ge setup with proper slit settings, the widths of the CDW peaks are about $2.5 \times 10^{-3}\overset{o}{A}^{-1}$ (HWHM) in the $2a^*-c^*$ direction and $4 \times 10^{-4}\overset{o}{A}^{-1}$ (HWHM) along the chain direction.

The positions of the superlattice peak shown in the figures 5-1 and 5-2 correspond to a CDW distortion wave vector $Q=(1,0.7447,-0.5)$. So, the distortion is commensurate with the underlying ionic lattice along the $2a^*-c^*$ direction and incommensurate along the b^* direction. This incommensurability was observed in all the reported
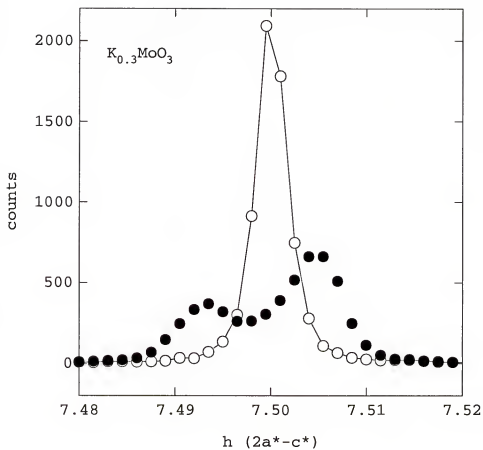
Figure 5-5 Scan profile of the CDW peak (15, -0.7445, -7.5) at T=35 K. The ○ is the zero field cooled data. The ● is collected 30 min after a field of 6.8 V/cm was applied. The curve is a guide to the eye.
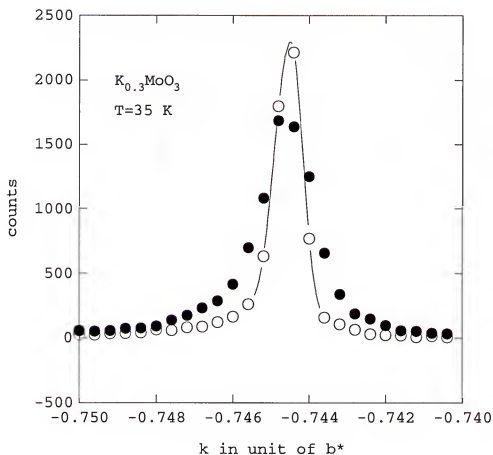
Figure 5-6 Scan profile of the CDW peak (15, k,-7.5) before and after an electric field is applied (E=6.8 V/cm). The curve is a guide to the eye.

blue bronze samples and arises from the K$^+$ deficiency when the crystals are grown as we already see in chapter 2.

Field Data

Figures 5-5 and 5-6 showed the scan profiles of the CDW peak (15, -ε, -7.5) taken after a dc electric field of 6.8 V/cm was applied at a temperature of 35 K. As discussed in Chapter 4, the way to apply the electric field is the following: first, cool the sample in zero field from room temperature to 35 K. Then, wait for the system to reach a thermal equilibrium. Then turn on the electric field and collect the scattering spectra after having waited for another 30 minutes or so (the time needed for the system to reach a thermal equilibrium again after application of the field).

Two features are obvious in the data: First of all, the overall breadth of the superlattice peak was broader after application of the electric field compared with the same scans before the field was applied. This is true for the scans in both directions. Second, the scan profile along the 2a*-c* direction split into two small peaks. Comparison of the widths of these small peaks with their zero field parent peak shows that the widths of the small peaks are approximately larger than the zero field peak by a factor of 2.5.
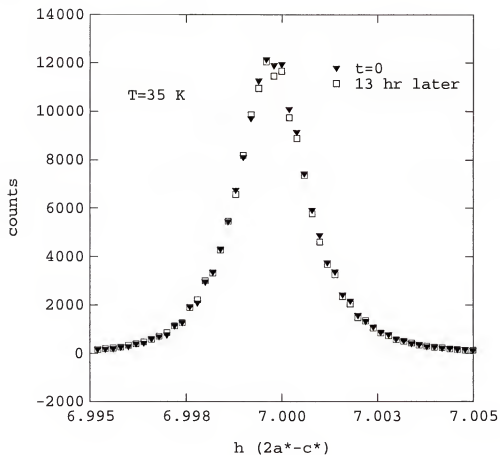
Figure 5-7 H-scan profiles of the Bragg peak (14,2,-7) in the (2a*-c*) direction. The two sets of data are taken 13 hrs apart, during which a field of 13.6 V/cm has been applied with both positive and negtive polarities.

The lineshape change of the CDW peaks is not from strain, because the Bragg peaks, which would also change if there was strain building up inside the sample, do not show any change before and after the field application. This is shown by figure 5-7, where the scan of the Bragg peak (14,2,-7) in the (2a*-c*) direction is plotted, clearly showing no sign of change. Since for this wave vector, a scan in the (2a*-c*) direction is very much like a θ-2θ scan, which would show a lineshape change in case there is strain building up in the sample, the data provide evidence that the observed lineshape change can only arise from the change of the CDW lattice, not from the underlying ionic lattice.

The zero field data are fitted best with a single lorentzian in the chain direction and with a lorentzian squared in the 2a*-c* direction. It is the same case as the Bragg peaks. After the electric field is applied, the two small CDW peaks in the 2a*-c* direction have the best fit with a gaussians as shown in figure 5-8. Fits by other functions with the associated χ^2 values are also shown in the figure for comparison. In the chain direction, the data are still described best by a single lorentzian after the field. The raw profile in the chain direction, and the fits by several functions with their normalized χ^2 values, are all shown in figure 5-9.
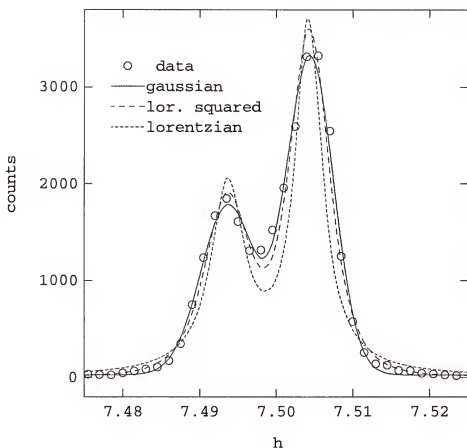
Figure 5-8 Scan profiles of the CDW peak (15, ε,-7.5) at 35 K in the (2a*-c*) direction in the presence of a field 6.8 V/cm. The curves are fits by the sum of two gaussians, two Lorentians or two lorentzian squared functions. The χ^2 for the fits are 10.4, 11.9 and 83.0 respectively.
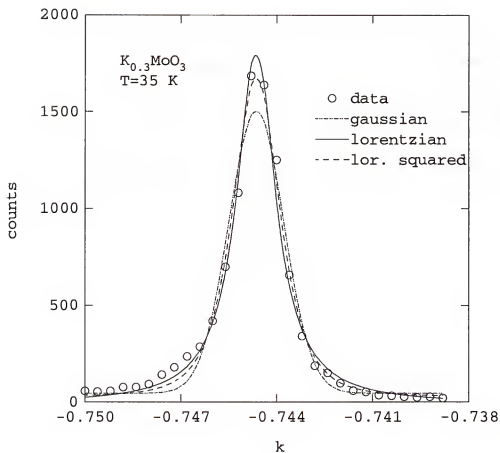
Figure 5-9 Scan profile of the CDW peak (15, k, -7.5) along the chain direction in presence of a field 6.8 The curves are fits by a gaussian, a lorentzian and a lorentsian squared functions. The fitted χ^2 are 20.7, 8.8 and 9.2 respectively.

The fact that the scan profiles have different lineshapes after an electric field is applied has aroused some interest [17,36]. It is argued that the CDW disordering caused by an electric field in the chain direction may be different in nature from that in the transverse directions. Normally, a gaussian or a lorentzian squared lineshape (they are not easy to distinguish experimentally) corresponds to a micro domain structure. If the domain sizes have a gaussian distribution, the scattering peak profile will have a gaussian lineshape; while a random size distribution yields a lorentzian squared lineshape. A lorentzian fit, however, usually arises from a correlation effect [17].

When discussing scattering data, what is meant by a microdomain is a region within which the superlattice is well ordered (it needs not be perfectly ordered). Two neighboring domains must be distinguishable in the sense that all the domains can be assigned a sequential number in principle, and the correlations between these must be very weak. The well known Fukuyama-Lee-Rice model which only discusses the phase of the CDW lattice [40,74] can not offer such a picture. Coppersmith [75] argued that when a big electric field is applied, the CDW lattice will break into different small regions, and that stationary and moving regions may coexist. For a CDW system, if the relative phase between different domains is random, the scattered x-

rays from many domains will be completely incoherent and the scattering profile will broaden because of the finite size of the domains (the coherent terms drop out because the structure factor of a domain depends on its phase ϕ_0 through a factor $e^{i\phi_0}$ [68], which eliminates the cross terms due to the randomness of the relative phases when averaged over many domains). While our data in the transverse direction clearly indicate that the CDW lattice is composed of different independent regions, the data can not tell if such a coexistence is the case since x-ray scattering is a snap shot and can not show if the studied superstructure is moving.

The data seem to indicate that the ordering is different along the chain direction from the transverse direction. If the lorentzian fit represents the true physics, what happens is that the correlation length ξ_b becomes shorter after application of an electric field. But this is not exclusive because the lorentzian squared fit is not much worse than the lorentzian fit. If the true physics is described by a lorentzian squared fit, the chain direction will also have a domain structure with a decreased domain size due to the applied field. Since a CDW domain can not be larger than a crystal grain, it is finite in all three directions.

The scattering peak lineshape of the disordered CDW lattice is highly reproducible over thermal cycling as shown
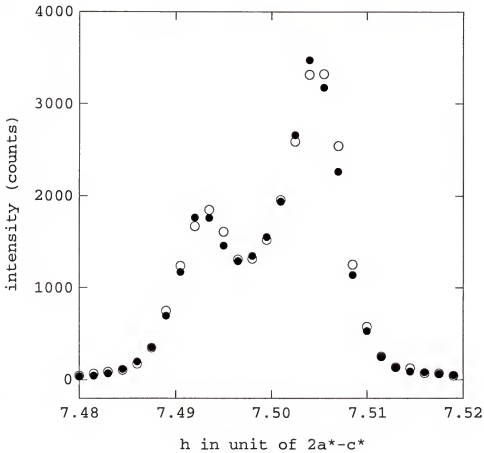
Figure 5-10 Scan profils of the CDW peak $(15,\epsilon,-7.5)$ taken during two different thermal cycles. The electric field is 6.8 V/cm and the temperature is approximately 35 K in both cases. The sample histories are discussed in the text.

by figure 5-10, where scan profiles of the superlattice peak (15, 0.7443, -7.5) taken during two different thermal cycles are plotted. There was no change at all. Of course, all the parameters were the same. These include the temperature, the strength of the applied electric field and the scattering setup or the system resolution.

The splitting in the superlattice peak lineshape along the 2a*-c* direction was repeatedly observed with several different electrical contacts. Figure 5-11 shows the scan profiles of the peak (15, ε, -7.5) taken at the same temperature when the same electric field was applied in the chain direction with different contacts. In one of the two cases, the edges of the crystal where contacts were affixed were cleaved mechanically to make sure that the new contacts would be fresh. As shown in the figure, in both cases, the splitting of the peak in the 2a*-c* direction is obvious and the breadths of the peak are approximately the same. There is difference, however, in the intensity distribution in the two cases. Such an intensity asymmetry comes about even without a contact change. As long as the sample was taken down and remounted onto the diffractometer, the intensity distribution was found to change to some extent. As argued later, this might be related to the pinning of the CDWs by the contacts. So, the electrical contacts or sample mounting do affect the lineshape to some extent. In spite of the many changes in these extrinsic effects, the peak
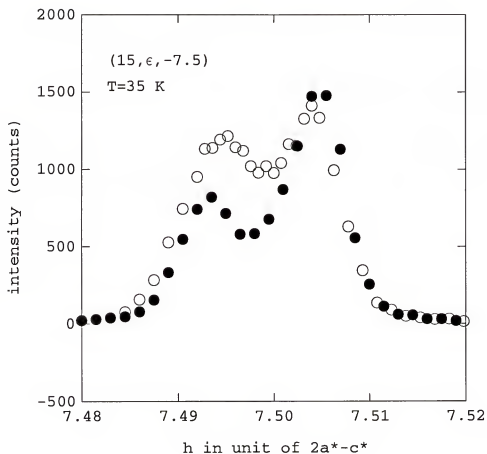
Figure 5-11 The same scan profile taken with different
electrical contacts. The applied electric field is 6.8
V/cm in both cases. The sample histories are explained
in the text.

splitting in the 2a*-c* direction was always observed and the overall breadth of the CDW peak in the presence of an electric field does not seem to depend on the contacts at all.

To map out the detailed intensity distribution, a contour plot of the superlattice peak (15, -.7443, -7.5) on the reciprocal plane containing b* and 2a*-c* directions is shown in figure 5-12. It is clear that the intensity peaks at two positions : (14.99,-ε,-7.495) and (15.01,-ε,-7.505) in the transverse direction. In the b* direction, however, no splitting could be observed.

The broadened or the split lineshape of the superlattice peaks is metastable. When the applied electric field is turned off, the disorder either slowly evolves in the course of time, and in many cases, remains unchanged in hours, as illustrated in figure 5-13. The first curve in figure 5-13 was taken with the electric field on and the second spectrum was collected about two hours after the electric field was turned off. No appreciable change in the scan profile could be seen. A previous experiment shows that the disorder of the CDWs in blue bronze induced by an electric field applied in the chain direction can be eliminated by thermal heating above some temperature [17]. The fact that the disorder is frozen at low temperatures and can be got rid of by heating to some temperature much lower than the transition temperature has been used to support the
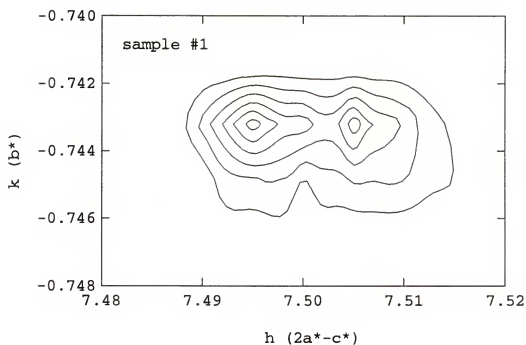
Figure 5-12 A contour plot of the CDW peak (15,-ϵ, -7.5) collected with an electric field of 6.8 V/cm after waiting 25 min at aprroximately 35 K.
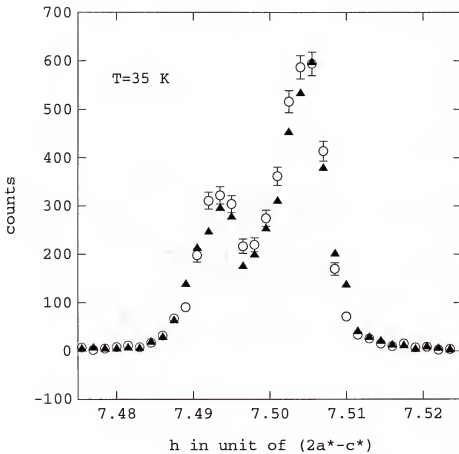
Figure 5-13 Scan curves of superlattice peak (15, -ε, -7.5) along the (2a*-c*) direction. The ▲ curve was collected with an electric field on and the ○ was collected 2 hr after the field was off.

hypothesis that there exist metastable states in a CDW
system. According to this hypothesis, an externally applied
electric field causes the CDWs to change from one metastable
state $\{\phi_i(\mathbf{r})\}$ to another.

Voltage Dependence

Figure 5-14 shows the scan profile of the superlattice
peak (15, -0.7433, -7.5) in the 2a*-c* direction under
electric fields of different strengths. The electric field
was applied in an increasing manner: starting from 170 mV/cm
to 10.2 V/cm after the sample was cooled in zero electric
field from room temperature to about 35 K. As shown in the
figure, the 170 mV/cm electric field only caused a
broadening of the superlattice peak and a noticeable
position shift to small $\mathbf{Q}$ value in the 2a*-c* direction.
After this small field, the field strength was increased to
255 mV/cm, 340 mV/cm and up to 680 mV/cm and no further
change could be observed in the lineshape of the peak
profile. Moreover, when the electric field was turned off,
the lineshape was frozen. This strongly supports the idea
of metastable states as mentioned earlier. After the field
of 680 V/cm, a field of 1.36 V/cm was applied. This time,
the peak lineshape changed dramatically in a period of three
hours: the peak broadened more and more, and the peak
amplitude decreased in the course of time. The curve shown
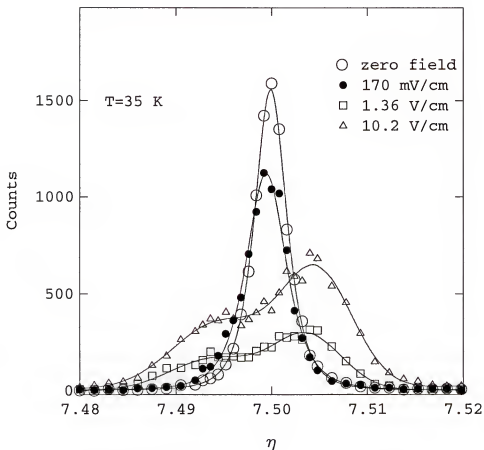
Figure 5-14   Scan profiles of superlattice peak
(15, -ε, -7.5) along the (2a*-c*) direction.   The
profilesare normalized to counts/min   excep that
of 10.2 V/cm, which is counts/4 min. The curves
are fits by a single Lorentzian squared function
for the 0 V/cm and the 170 mV/cm, and by a sum of
two gaussians for the 1.36 V/cm and 10.2 V/cm.

amplitude decreased in the course of time. The curve shown in figure 5-14 for this field value corresponds to the lineshape at the final stage, where again, no further change in the lineshape of the superlattice peak could be seen at this field strength. It already started to show a double peak structure. Such a structure became more obvious in the curve corresponding to the field of 10.2 V/cm in the figure.

As shown by figure 5-14, when the applied electric field is small, the center of mass for the scattering profile shifts to smaller wave vector side. When the field strength is increased, it starts to shift to the higher wave vector side. This same phenomena have been observed in other samples. Figure 5-15 (a) shows the same scan done on another sample (#7) at T=25 K for the peak (15, 2-ε,-7.5) or (16,2,-8)-**Q** and (b) shows the scan for the peak (15,2+-ε,-7.5) or (16,2,-8)+**Q**. For either peak, the field causes the center of mass for the peak position to shift in different directions for the two different field strengths. Furthermore, as shown in figure 5-16, under the same field, all CDW peaks associated with +**Q** shift in the same direction, and all those associated with -**Q** shift in the opposite direction. Another feature shown by the figures from 5-14 to 5-16 is that application of an electric field decreases the area under the scan curve in the (2a*-c*) direction. The larger the applied field is, the more area under the scan curve will be missing. Since the total
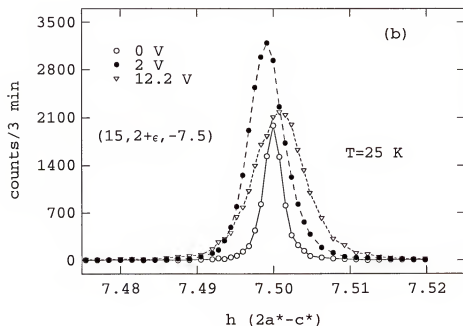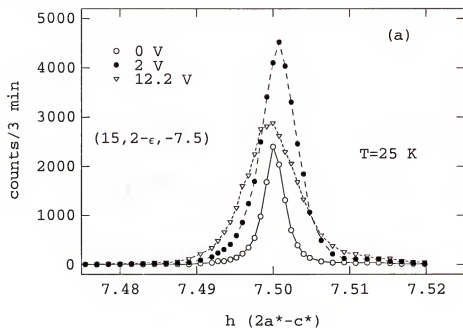
Figure 5-15 Scan curves of CDW peaks in the (2a*-c*) direction for sample #7. The zero field data are counted three times shorter than the other scans in each graph.
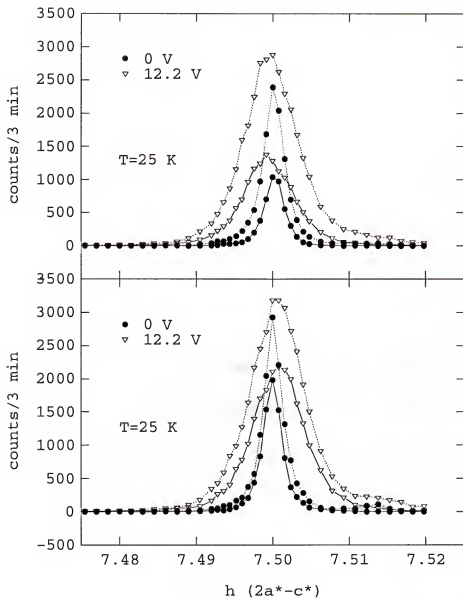
Figure 5-16 Scan curves of CDW peaks associated
with -Q (top) and with +Q (bottom) on sample #7.
Curves of the same line type in each graph belong
to one wave vector but under different fields. The
zero field data (•) are counts/min.

spectrum has to be conserved, there are only two possible reasons for this phenomenon: either there are more scattering in the other two directions, or the crystal absorbs more photons after application of a field. The reason is not clear at this moment.

Although the lineshape change is frozen at 25 K in the sense that turning off the electric field causes no noticeable change in the lineshape, it is quite sensitive to temperature, as shown by figure 5-17. When the temperature is raised from 25 K to 33.5 K under zero field, the profile shifts back to almost the same peak position as the zero field cooled data (the little structure near h=7.513 in figure 5-17 is due to the Cu K_α^2 x-rays). Even after a small electric field is applied, the profile does not shift away from the zero field cooled position by an appreciable amount, as shown by figure 5-17 (application of big fields are prohibited by the tremendous Joule heating they cause to the sample). Another feature shown by figure 5-17 is that raising temperature after application of an electric field increases the area under the scan curve in the (2a*-c*) direction, suggesting that the CDW lattice relaxes towards the zero field cooled state. Previous measurement shows that raising temperature above 100 K can eliminate all the effects on the scattering lineshape of an electric field applied at low temperatures [17].

Sample #7 did not show a clear peak splitting in the
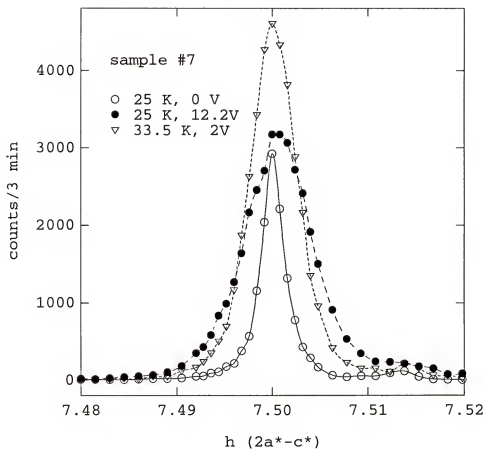
Figure 5-17 H-scan of the CDW peak $(15, \epsilon, -7.5)$ at different temperatures and electric fields. The zero field cooled data are counts/min. The curves are guides to the eye. The small peaks near h=7.513 are due to Cu K_{α}^{2} x-rays.

(2a*-c*) direction after a big electric field was applied.
We studied five different samples, three of those showing
the splitting and the other two do not. A clear explanation
is still lacking at this time. However, as shown by figure
5-17, in order to study the lineshape change, some special
caution should be taken, since both the strength of the
applied field and temperature can affect the result greatly.
My guess is that if one applied a huge electric field at a
very low temperature, splitting should be expected. The
trouble of doing this is that if the applied electric field
exceeds the low-temperature threshold field E_T^2, there will
be tremendous amount of heating and the sample temperature
will increase drastically and kills the lineshape change, as
shown by figure 5-17.

Besides field strength and temperature, the lineshape
of the scattering peak profile is also sensitive to the
polarity of the applied electric field. Figure 5-18 shows
two scan curves of the CDW peak (13, -2+ε, -6.5) of sample
#1, taken under the same electric field 13.6 V/cm but of
opposite polarity. One can see that the two scan curves
look like the mirror image of each other. We will discuss
this a little more in next chapter.

Sample Dependence:

The peak broadening along the chain direction in blue
bronze was also observed by other groups [20]. However, the
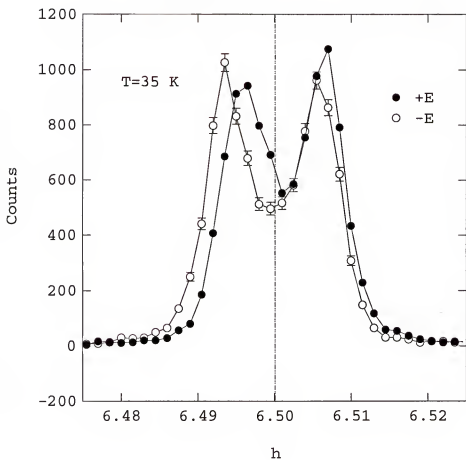
Figure 5-18 Scan profiles of the CDW peak (13, -2+ε,-6.5) along the (2a*-c*) direction. The data were taken under the same field but of opposite polarities. The central line indicates the zero field peak position. (E=13.6 V/cm)

splitting of the superlattice peaks along the 2a*-c* direction was never observed before. With the high reproducibility upon thermal cycling and electrical contact change on one single crystal which had a mosaic spread of 0.01° (FWHM), we repeated the measurements on three other crystals and the peak splitting was also observed in the new samples. Figure 5-19 shows the results taken on one crystal that had a mosaic spread of 0.012° (FWHM). The scan profiles of the superlattice peak $(13,-\varepsilon,-6.5)$ in the 2a*-c* direction are plotted before and after an electric field was applied. Although the peak splitting was not as obvious as in the previous sample, it was undeniable and the two small peaks were approximately at the same positions as in other crystals.

<u>Heating:</u>

In all the above experiments, the Joule heating caused by the applied field can be shown not to be a problem. Certainly, the peak splitting was not caused by heating, which at such temperatures (around 35 K), could only narrow the broadened peak profile induced by the electric field [17]. Another fact that supports this is that the peak lineshape does not change after the electric field is turned off. A simple estimate given in Appendix B also shows that the heat imposed by the external electric field to the sample can be easily conducted away.
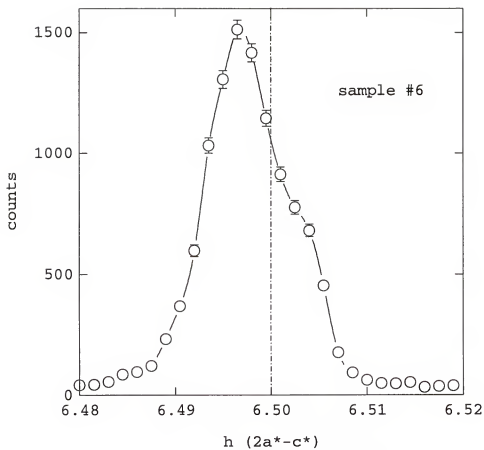
Figure 5-19   Scan   profile of the CDW peak (13, -ε, -6.5) on sample #6 which has a mosiac spread of $0.012°$ (FWHM). The central line indicates the peak position of zero field data.   The curve is a guide to the eye.

Ginzburg-Landau Free Energy Argument

Summarizing the experimental observations discussed above, we have the following results: the peak broadening in the chain direction and the broadening or the splitting (for big electric fields) in the transverse direction are very reproducible upon thermal cycling and change of electrical contacts, and they are metastable in the sense that the disorder is frozen at low temperatures. The lineshape also depends on the strength and the polarity of the applied field. It is not caused by strain as would cause changes in the Bragg peaks.

All these suggest that the observed lineshape change of the CDW peaks by electric fields is an intrinsic effect. Though artificial factors have effects on the CDW lattice disordering, the very nature of the lineshape change in the presence of an electric field is intrinsic. The split structure in the transverse direction can not be related to a simple reduction of the coherence length, which would have yielded a simple broadening only. The overall behavior suggests a domain structure. The fact that the two small peaks in the transverse direction can only be fitted well with a gaussian supports such an idea. But what mechanism could be responsible for such a phenomenon that seems to suggest two nearly degenerate states? This is certainly not

due to the change in the number of condensed electrons since it is well established by x-ray scattering experiments that application of an electric field does not change the amplitude of the order parameter [9]. So the observed phenomena arise from a change in the CDW phase.

One possibility is that the pure system simply has a different ground state for $\mathbf{E}=0$ and $\mathbf{E}\neq0$, with the latter situation corresponding to a reduction in symmetry. The second possibility which I favor at the present time is that the double-peaked structure is a signature of the domains that form because the CDW is pinned by defects in a manner that causes the effective wave vector to shift. An idea of how this may work can be obtained as follows:

In the incommensurate CDW state characterized by wave vector $\mathbf{q}$, the positions of ions in the lattice are given by the following [68]:

$$\mathbf{R}_{i\gamma}=\mathbf{R}^0_i+\mathbf{d}_\gamma+\mathbf{A}_{0\gamma}\cdot\sin[\mathbf{q}_0\cdot(\mathbf{R}^0_i+\mathbf{d}_\gamma)+\phi_{0\gamma}]$$

where $\mathbf{R}^0_i$ is the position of the unit cell, $\mathbf{d}_\gamma$ is the position of an ion inside the unit cell, $\mathbf{q}_0$ is the CDW wave vector and $\phi_{0\gamma}$ is the CDW phase, which should be independent of $\mathbf{R}^0_i$ in the absence of an external field. The total phase describing the ion positions is given by $\phi_{tot}=\mathbf{q}_0\cdot(\mathbf{R}^0_i+\mathbf{d}_\gamma)+\phi_{0\gamma}$ and the CDW wave vector can also be written as $\mathbf{q}=\nabla\phi_{tot}$. For $K_{0.3}MoO_3$, $\mathbf{q}=(1,0.75-\varepsilon,-0.5)$, where the b* is in the chain direction, the (2a*-c*) is in the direction normal to the layers (and also to the chain direction), and ε is a small

irrational number for the incommensurate CDWs. The phase $\phi_{0\gamma}$ is constant on sheets perpendicular to b* (apart from the trivial phase shift of π between neighboring chains).

An applied field in the b* direction may cause the ions to shift slightly along the chains. A defect at some site on a given chain may prevent the shift from occurring on that chain, and inhibit the shift on neighboring chains. If the shift is allowed to relax from total suppression at the defected chain in a linear fashion, i.e., $\Delta\phi_{0\gamma}=\kappa(\mathbf{R}^0_i-\mathbf{r}_{im})$, where $\mathbf{r}_{im}$ is the position of the defect, then the effective wave vector arising from that region will be changed to $\mathbf{q}'=\mathbf{q}+\kappa\hat{\mathbf{x}}$. Since the pinning will relax both above and below the chain (see figure 5-20), in fact, there will be two wave vectors, $\mathbf{q}'_{\pm}=\mathbf{q}\pm\kappa\hat{\mathbf{x}}$. In $K_{0.3}MoO_3$, the softest direction for relaxation is the 2a*-c* direction. It is clear how pinning might, in principle, produce a peak splitting in this direction, corresponding to different CDW wave vectors.

Another pinning mechanism is the domain boundaries. If the CDW phase changes in space inside a domain but keeps pinned on the domain boundaries, one half of the domain will have smaller wave vectors and the other half, bigger ones (see figure 5-21). Furthermore, if the phase change is linear in space inside the domain (looking like a greater sign ">"), two clear wave vectors are present and the split structure should form in the CDW scattering peak profiles.
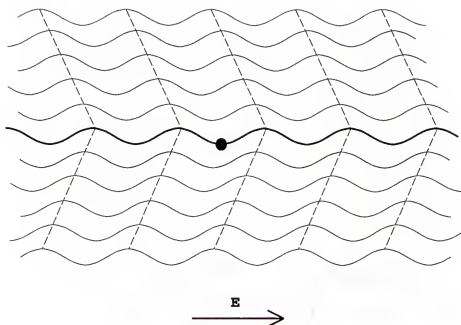
Figure 5-20 Schematic of impurity pinning of the CDW phase. The impurity site on the central (thick) chain pins the phase of the CDW on that chain, and through interchain interactions, it also affects the CDW phase on adjacent chains. The further away from this site, the weaker the pinning. (**E** is the electric field).
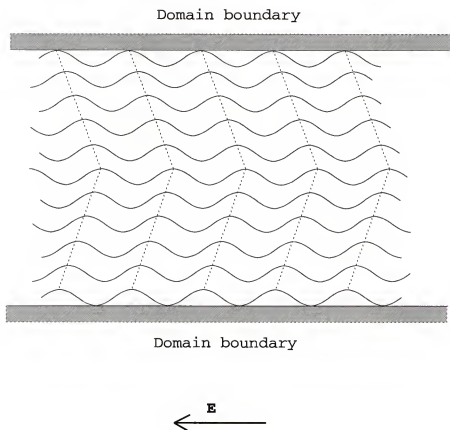
Figure 5-21 Schematic of domain boundary pinning of
the CDW phase. The CDW phase changes in space under
an external dc field. However, it is pinned on the
domain boundaries. This causes a spatial variation
of the phase. The dashed lines indicate the wave
fronts of equal phase. (**E** is the electric field).

A crude estimate of the size of the peak position shift in the (2a*-c*) direction can be obtained using Ginzburg-Landau free energy argument [40,74], as shown in Appendix C. It assumes that the CDW lattice is composed of different regions after application of an electric field, and the correlations between these regions can be neglected. The theory gives an overall broadening of 1×10^{-2} A^{-1} in the (2a*-c*) direction for an electric field of 7 V/cm whereas the experiment gives a breadth in the peak, 0.8×10^{-2} A^{-1} in the same direction. To the order of magnitude, the agreement is pretty good. The calculation also predicts that the peak broadening is larger for stronger fields, which also agrees with the experiment. Last of all, it is found experimentally that the peak broadening saturates when the applied field gets quite large. This can also be accounted for by the theoretical argument. The reason is the following: the peak broadening is predicted to be proportional to a function (f(E) in eqn. (C6)), which is the subtraction of two terms: $\frac{eE}{\pi\overline{v}_f}-\alpha\dot\phi$. When the electric field is smaller than E_T, the second term is zero and f(E) is proportional to the electric field. However, when the electric field exceeds the threshold value, $\alpha\dot\phi$ thus f(E) is no longer proportional to the applied field and f(E) increases at a smaller and smaller rate than a linear relation as E increases. This is due to the non-Ohmic behavior of the CDW current, which is proportional to $\dot\phi$.

Despite the many successes of the theory, it also has problems. For example, it does not predict a clear peak splitting in any crystal direction while the splitting is observed experimentally in the 2a*-c* direction on at least two samples. As discussed on pages 108 and 109, if the CDW phase changes in space linearly as shown by figures 5-20 and 5-21 This, I believe, is due to two reasons: first, we assumed a complete pinning of the phase by the impurities and by the domain boundaries, which is a simple but not a good approximation. The fact is probably that both the impurities and domain boundaries only partially pin the phase. The second and maybe more important reason for the discrepancy between the theory and the experiment is that we assumed completely harmonic interactions between the ions. There is no reason to believe that no anharmonic interactions exist in this quasi-one dimensional material. In any case, it is clear that further theoretical studies are needed to clarify the situation.

Comments

Fleming et al studied the electric field induced disordering in blue bronze in 1985 [17]. They mainly did two experiments:

1>. apply an electric field ($3E_T$) for 1 s in the chain direction at a temperature of 65 K;

2>. cool the sample under an electric field of $3E_T$ applied in the chain direction from room temperature to 10 K.

In both cases, they found that the electric field broadened the superlattice peak in a transverse direction. Along the chain direction, no change was seen in the superlattice peak lineshape. The failure of their experiments to see the peak broadening in the chain direction or the peak splitting in the normal direction to the layers (one of the transverse directions) was likely due to the fact that the applied electric field was too small and the application time was too short (only 1 s). As shown by the calculation, the expected splitting for the electric field they applied was at least four times smaller than what we observed. Considering the fact that their resolution was not as good as ours, to observe the splitting was obviously very difficult for them. For the field cooling experiment, they did not scan along the symmetry direction. This alone might be able to explain why they only saw a simple broadening instead of a split structure in the transverse direction. After all, they did a different experiment from what was done in the present work (where the sample was cooled under zero field and then the field was applied.

During the process of writing this dissertation, DiCarlo et al. [76] studied how the CDW wave vector $\mathbf{Q}$ varies inside the sample along the chain direction in $NbSe_3$. They used a small synchrotron beam to study how $\mathbf{Q}$ varies from one

spot of the sample to another as the beam moves along the chain direction. They found that the chain component of **Q** varies linearly with the distance from the center spot of the sample. If one carries out the calculation in one dimension, he will obtain such a linear prediction. Figure 5-22 shows the CDW phase and the equal-phase fronts in the chain direction in the presence of a dc electric field applied in the chain direction. The authors in ref. 70 did a detailed study of the role of the electrical contacts. By averaging over the transverse directions, they found that the CDW phase changes in a quadratic manner (or **Q** changes linearly) in space in the chain direction after application of a big electric field, and it depends on a quantity which they call "phase-slip voltage", which is basically the function $f(E)$ (see eqn. C6) in our calculation, except for a term proportional to E_T, which is very small compared with the external field in our experiments. However, if one does not average over the transverse directions, as demonstrated in Appendix C, one will find that the spatial variation of the CDW phase is different from a simple quadratic form, although when only harmonic interactions are considered, the result is not significantly different from a quadratic dependence on distance.

One thing that one should keep in mind is that the samples which DiCarlo et al. studied is quite different from the sample we studied. They used $NbSe_3$, which is much more

one-dimensional than $K_{0.3}MoO_3$ and $NbSe_3$ crystals are usually
like hairs: it can be extremely long in the chain direction,
but very short in the transverse directions (the sample used
in ref. 59 has a dimension of 8mm x 40μm x 7μm).
Furthermore, $NbSe_3$ is a very clean system, in strong
contrast to $K_{0.3}MoO_3$, which is generally a dirty crystal. So
the impurity pinning is much less prominent in their case,
which somewhat justifies the theory they used to explain
their data since that theory ignores the role of impurity
pinning when it discusses the spatial variation of the CDW
phase in the chain direction, and only considers the
electrical contacts [77]. Of course, the difference between
$NbSe_3$ and $K_{0.3}MoO_3$ is quantitative, not qualitative. The
spatial variance of the wave vector observed in $NbSe_3$ is
just a simplified situation. In terms of the calculation
presented here, it corresponds to the limiting case, $L_x \approx L_y \approx$
0, and $L_z \rightarrow L_o$, where L_o is a length comparable to the sample
size in the chain direction.

Temperature Effects on CDW Correlations

As mentioned in chapter 2, most of the known materials
that exhibit a CDW transition have a transition temperature
lower than room temperature. The main reason is that the
entropy term in the system free energy in creases rapidly
with temperature, and at sufficiently high temperatures,

chain direction
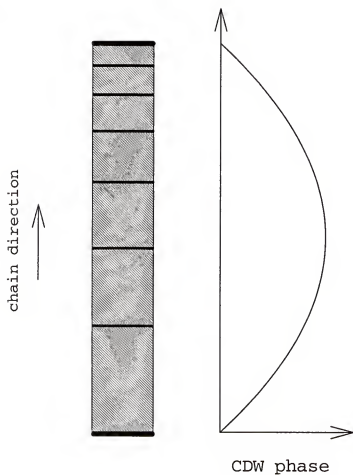
CDW phase

Figure 5-22 Schematic of the spatial variation of
the CDW phase and equal-phase fronts between two strong
pinning centers (the two ends in the graph).

this "chaotic" term completely decomposes the superlattice structure. However, as the transition temperature is approached from above, one can imagine that the CDW correlation length in the systems will gradually increase to infinity because the transition is a second order phase transition. Figure 5-23 shows such a trend clearly. As discussed in Chapter 3, the correlation length is the inverse of the resolution-corrected width of the scattering peak profile if the scattering peak linewidth is mainly caused by the finite correlation length of the system. A simple way to obtain the correlation length from the measured linewidth is the following method:

$$\xi = \pi \sqrt{HWHM^{-2} - \sigma_{res}^2}$$

where ξ is the corrected (true) correlation length, and σ_{res} is the system resolution, which can be taken as the HWHM below the transition temperature at the present case. Below T_c, the CDW scattering peak line width remains constant, as expected (since below T_c, the long range order in the chain direction establishes).

Figure 5-23 also plots a fit using the known power law function $\xi \propto (\frac{T}{T_c} - 1)^{-2\beta}$, where β is set to be 1/3 [78,79,80].
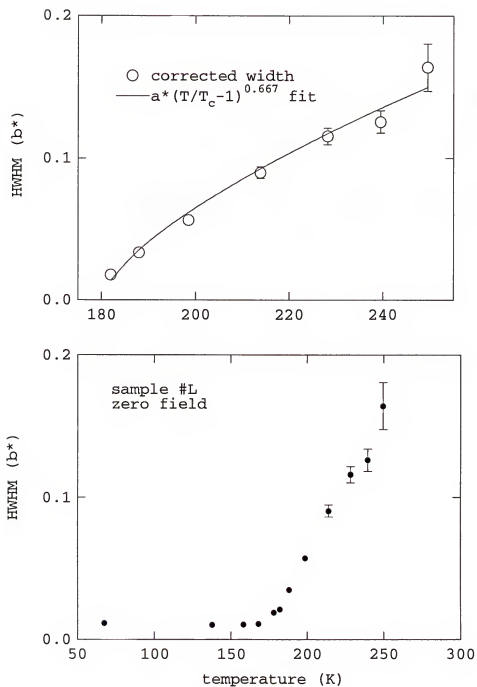
Figure 5-23 Temperature dependence of the CDW scattering peak width. The curve in a) is a fit using the critical power law with a power of 2/3.

CHAPTER 6
RESULTS/DISCUSSION II - KINETICS

The disordering of a CDW lattice by a dc electric field
at low temperatures occurs on a finite time scale. We have
characterized the interesting kinetics at different field
strengths and temperatures. It is found that the relaxation
time scale depends sensitively on temperature and the
strength of the applied electric field. The data are
analyzed and suggest that the structural disordering is due
to a polarization process.

CDW Lineshape Evolution

As I pointed out during the discussion of figure 5-14,
the scattering peak lineshape of the CDW lattice could
change dramatically upon application of an electric field.
Figure 6-1 shows three scan profiles taken after a field of
1.36 V/cm is applied at a temperature of 35 K. The sample
history is the same as in figure 5-14. It is evident that
the peak lineshape was evolving over the studied period of
three hours. It became broader and broader as time
progressed.
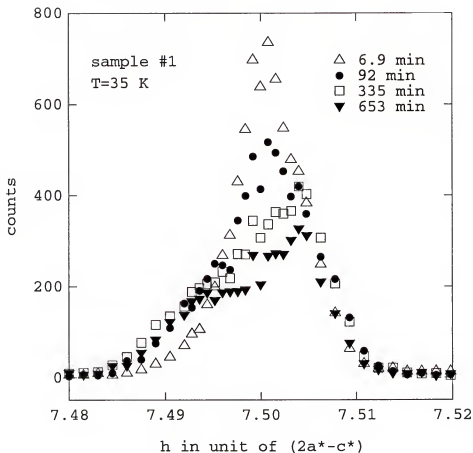
Figure 6-1 Scan profiles of the CDW peak (15,-ε, -7.5) along the (2a*-c*) direction. The scans are collected the specified times after a field o 1.36f V/cm is applied.

The lineshape of CDW peaks depends on the polarity of the external field as shown in figure 5-14. The kinetics that shows the transition from one lineshape to the other after switching the polarity is very interesting and is illustrated in figure 6-2. The scans are for the (15, -0.7445, -7.5) CDW peak. The zero field scan is shown in part (a). An initial dc field of 6.8 V/cm was applied along the b* direction and the scan in the presence of this field is shown in part (b). After this, the field was turned off for two hours. With zero field, the lineshape did not change over this time period. Following this, a field of 2.7 V/cm with opposite polarity was applied. The scan shown in part (c) was collected starting 21 min. after the application of the second field and that in part (d) was taken after 90 min. The clear trend is present towards a trade off intensity in the two small peaks, or the lineshape to its own mirror image. As I mentioned during the discussion of figure 5-15, a CDW peak of wave vector **G**+**Q** looks approximately like the mirror image of **G**-**Q** (**Q** always represents the CDW distortion vector in this dissertation). It is reasonable to conclude that there are two wave vectors, each independently leading to a CDW peak, which agrees with the picture presented by figures 5-20 and 5-21. For the present case, when the polarity of the external field is changed, the change of the CDW phase due to the
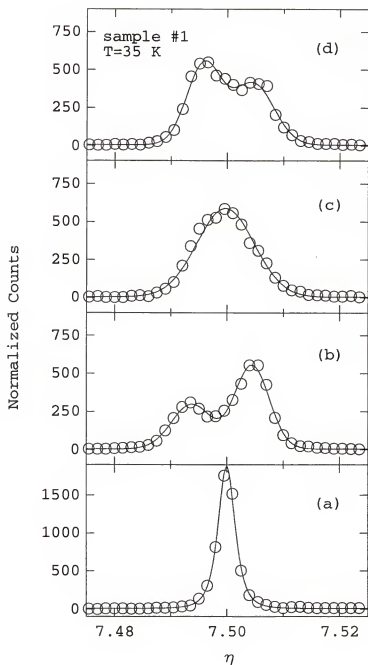
Figure 6-2   Scan profiles of CDW peak   (15, -ε, -7.5) along the (2a*-c*) direction. a) is zero field cool data; b) is taken 30 min after a field of 6.8 V/cm is applied; c) is collected 21 min after a field of -2.7 V/cm is applied after the field 6.8 V/cm is turned off for 2 hr. The curves are fits described in the text.

external field changes sign, therefore we observe a tradeoff between the two small peaks.

Intensity & Electric Current Evolution

The disordering kinetics is studied in more detail using a PSD in order to catch the fast change in the CDW lattice disordering. After the sudden application of an electric field, the PSD collects scan spectra along a direction of approximately (1.84,-1,0) in the reciprocal space near the CDW superlattice peak (13, 0.7495, -6.5). By summing up the counts above background in all detector channels, one obtains the number of photons that are scattered into a finite region in the reciprocal space near the peak position (see figure 4-9). After application of an electric field, the CDW peak gets broader and broader, and more and more photons are scattered outside the region the PSD scans in. So, the above summed response can be used as a quantity (called intensity below) to measure how much the CDW has been disordered by the field.

Figure 6-3 shows four spectra taken by the PSD at four different times after an electric field of 25 V/cm is applied on sample #K. It is obvious that the peak amplitude decreases in the course of time. The change in the lineshape is, however, not very obvious. This is due to the coarse resolution of the system. Another feature shown by

130
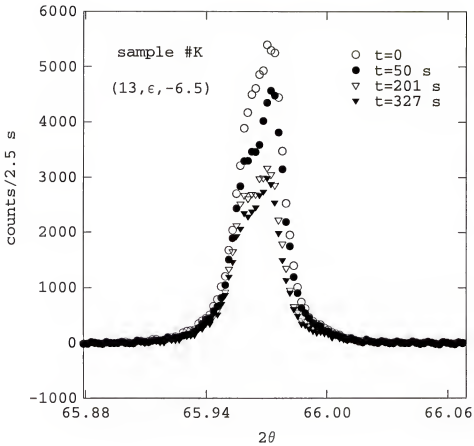
Figure 6-3 PSD spectra collected after an electric
field of 25 V/cm is applied. The four curves are
at four different times after the field application.
The temperature is 18.9 K.

the data is that the scattering profile is not symmetric about the peak position. This is caused by the non-perfect alignment of the detector relative to the scattered beam. This makes analysis of the lineshape change extremely difficult. Therefore, the discussion given below only concentrates on the intensity, which does not depend on the lineshape of the spectra since it is a summed quantity.

Figure 6-4 shows the time dependence of the intensity. The monotonic decrease with time is obvious. Figure 6-5 shows the time-evolution of the bulk electric current, which was obtained in-situ with the x-ray scattering spectra. Overall, the response is like a lossy dielectric, i.e., there is a large current at short times, decaying to a non-zero constant at long times. The asymptotic value at long times is a result of the non-zero temperature of the sample and the steady sliding of the CDW. The noise-like response on top of the monotonically decaying response in the current is due the oscillations or the so called narrow band noise (NBN). As we discussed in chapter 2, this arises from the periodic potential experienced by the CDWs [81,82]. Figure 6-6 plots a small portion of the early current data and shows the oscillations clearly. We have studied the oscillation frequencies under two different electric fields and find that the frequency is approximately proportional to the electric current. For example, at T=19.95 K, the oscillation frequency is 0.54 Hz
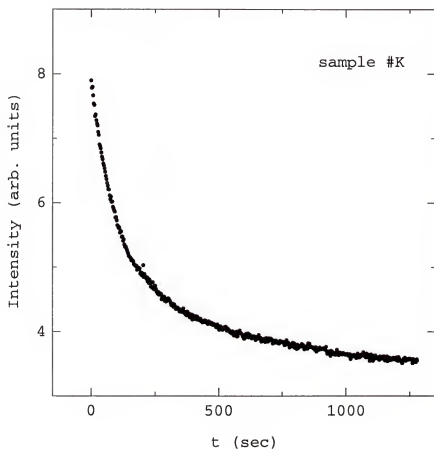
Figure 6-4 Evolution of the CDW peak intensity after application of an electric field of 25 V/cm at 18 K. The error bar is about the size of the symbols.
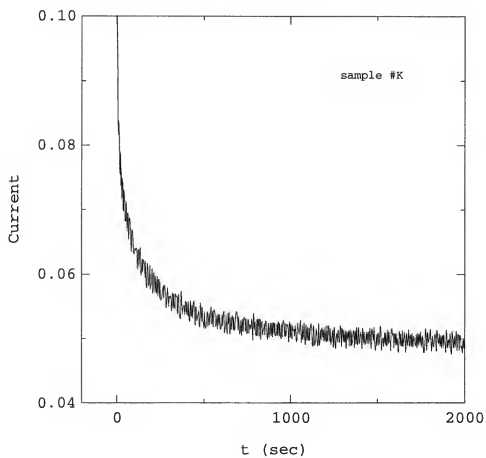
Figure 6-5 Electric current evolution after the application of an electric field of 25 V/cm at a temperature of 18.9 K.
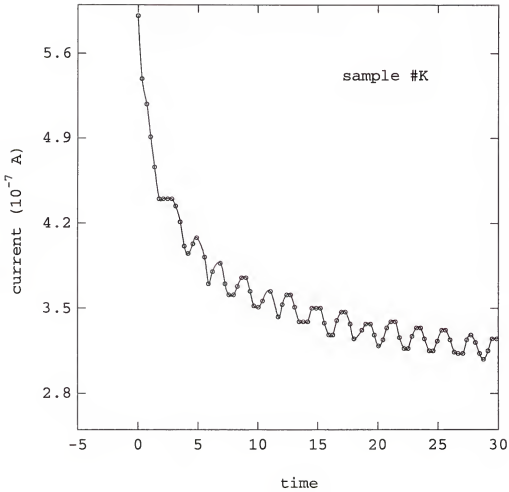
Figure 6-6 Evolution of electric current. T=19.5 K and E=41 V/cm. The clean oscillations provide evidence that the current injection is homogeneous.

when the electric current is 0.287 µA. The frequency-current ratio is, 0.537Hz/0.287µA=1.87×10⁷ (Hz·A⁻¹); while at T=18.9 K, the oscillation frequency is 0.96 Hz when the electric current is 0.051 µA, and the frequency and current ratio is, 0.96Hz/0.051µA=1.88×10⁷ (Hz·A⁻¹). If we use the current density instead of current, we get the following value for the ratio of the frequency over the current density:

$$\frac{f_0}{j} = \frac{0.96\,Hz}{0.051\,\mu A \,/\, 0.4\,mm^2} \approx 7.53 \;(Hz \cdot m^2 \cdot A^{-1})$$

which is in very good agreement with previous measurements [44]. One thing that I need to mention is that the small temperature difference in the above two cases does not have much effect on the frequency-current ratio. This has been well proved to be case [44].

Structure-Transport Correlations

The simultaneous measurements of the electric current and the structural disordering provide a direct probe to the correlations between the transport property and the CDW lattice structure. Figure 6-7 shows such a correlation, where the CDW peak intensity is plotted versus the electric current. Except the first few points which lasted for about 30s, the two quantities are clearly correlated. This shows strong evidence that the long time behaviors of both arise
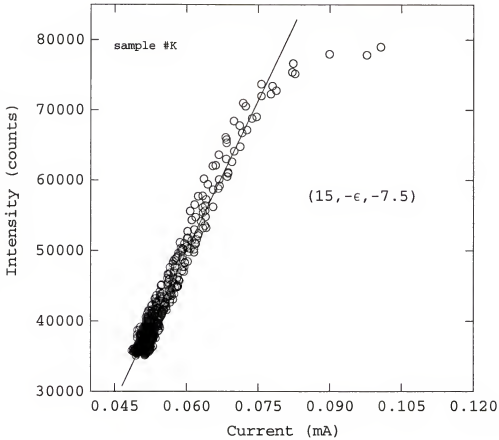
Figure 6-7 CDW peak intensity vs. electric current measured in-situ after an electric field of 25 V/cm is applied at 18.9 K. The straight line shows the correlations between the two quantities.

from the same process. The difference at short times suggests that there could be two distinct processes governing the dominant behaviors of each. However, at very early times when the peak profile is narrow and well center at the peak position, the measured intensity may be somewhat sensitive to the system resolution (a limiting case is that the system resolution is much broader than the CDW peak width. At such a case, no change in the intensity can be observed. The reason is that the integrated intensity can not be changed by the electric field since it is determined by the CDW distortion amplitude which is gapped.

The disordering kinetics of the CDW can be understood in terms of the polarization process in the system, which occurs when an electric field is applied. The argument is the following: the applied field causes the CDW lattice and the ionic distortion to deform and builds up a polarization. Since at such a low temperature, the CDW sliding is highly viscous, there is a long period of transient before a final steady state is reached. During this process, the polarization, which is big due to the large dielectric constant of the system, increases monotonically. The Maxwell's equation gives the following relation between the current and the polarization:

$$\boldsymbol{j}(\boldsymbol{r}, t) + \frac{\partial \boldsymbol{p}(\boldsymbol{r}, t)}{\partial t} = 0$$

Integrating the above over the whole sample yields a simple relation between the bulk electric current and the total

polarization: $I(t) = \dfrac{dP}{dt}$. On the other hand, the polarization

is linearly related to the displacements of the ions from

their equilibrium positions, and the CDW peak intensity is

correlated with such displacements. This explains why the

current is correlated with the intensity.

Description of the CDW Relaxation

In order to better understand the kinetics of the CDW

lattice relaxation, fits to the time dependence of the

intensity with several canonical functions have been tried.

These include power law, single exponential and stretched

exponential fits. We find that these functions can not

describe the data very well: the power law and the single

exponential are obviously bad fits. The stretched

exponential (five adjustable parameters) describes the data

very well at late times, yet it misses the data at early

times to a big degree. The result forces us to try other

functions. The fitting curves and the raw data are plotted

in figure 6-8 and table 6-1 shows the quantity $\chi^2 - 5 + N_{free}$,

where, χ^2 is the normalized least chi squared and N_{free} is the

number of free adjustable parameters of the fits. The

double exponential is an excellent fit. This seems to

suggest that the system indeed has two processes if this

function describes the true physics. One thing that is

worthy mentioning about this fit is that the early times
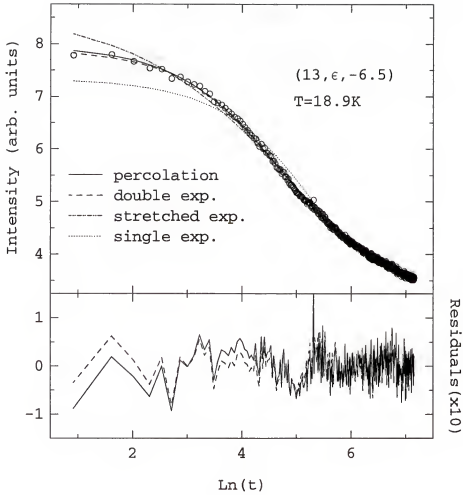
Figure 6-8   CDW peak intensity vs Ln(t). The ∘ is the raw data and the curves are fits described in the text. The bottom shows the residuals for the double exponential and the percolation fits.

constant for the current obtained from the fit is much
shorter than that for the intensity, and for late times,

Table 6-1 Fitting results

function	χ^2-5+N_{free}
double exponential (see text)	1.90
percolation model (see text)	0.99
stretched exponential $(S(t)=S_i\exp[-(t/\tau)^\beta]+S_0)$ $\tau=136.4,\quad \beta=0.591$	3.67
simple exponential $(I_i\exp(-t/\tau)+I_0)$	23.8
power law $(S_i\cdot t^{-\beta}+S_0)$	29.5

the time constants for the two quantities are quite close.

One can imagine two distinct processes arising from
different pinning strengths, such as from extended defects
versus point defects, or from different mechanisms such as
phase deformation and phase slipping. Since the applied
electric field is higher than the threshold field, the CDW
is sliding and phase slip process is also occurring. In
principle, we might observe phase slip at short times (any
relaxational response associated with phase slip should be
fast compared to phase deformation), and the phase
deformation process afterwards.

As mentioned in chapter 2, a CDW system with impurities
is known to possess a large number of metastable states due
to the presence of impurities. This is similar to a random

magnetic system. Random systems are not generally describable by a single time constant. Time dependent properties in random systems are often parametrized by a stretched exponential [83]. It is questionable whether a CDW system could be described by only two time constants. Because there is no clear rationale for only two time scales, we tried another function which has been employed to explain the relaxation of disordered magnetic systems, including spin glasses [84,85]. There are two basic assumptions one has to make when using this function:

1). The CDW system is composed of domains and these domains relax independent of one another;

2). The relaxation rate of a specific domain depends on its physical size exponentially and smaller domains relax more slowly.

The domain size distribution has been calculated by a percolation model [86]. The microscopic relaxation occurs through dispersive excitations, which for the present case could be related to the long-wavelength deformations of the CDW (phasons). For three dimensional systems, the function characterizing the relaxation is the following:

$$S(t) = S_i \int_0^\infty x^{10/9} \exp(-x^{2/3} - t\gamma e^{-c/x}) dx + S_0 \qquad (6)$$

The fit using the above function is also an excellent fit
and it has one fewer adjustable parameter than the double
exponential fit.

At this stage, we are unable to explain why the system
should relax according to Eqn. (6), because it is not clear
physically what an individual domain would be for the CDW
state. However, both the kinetics and the statics studies
of this work suggest that the CDW system is a domain
structure in the presence of an external field. Whether or
not the observed kinetics is caused by the domain structure
remains as an open question. More theoretical work is
needed to clarify the situation.

Other Characteristics of CDW Relaxation

The CDW relaxation in the presence of an electric field
is found to be extremely sensitive to the strength of the
external field and temperature. For example, At the same
temperature 18.8 K, when the applied electric field is
increased by a factor of two, the relaxation rate and the
bulk electric current increase by a factor of 15 ! Of
course, more experiments need to be done before we can make
any claim about the possible correlation between the
relaxation rate and the current. Temperature also effects
the relaxation rate greatly. Figure 6-9 is a primitive
investigation of such dependence, where relaxation rate is
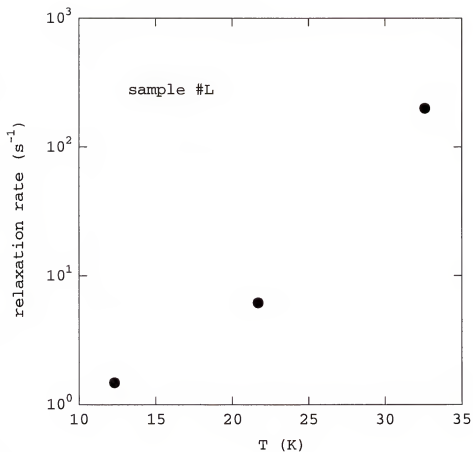
Figure 6-9 Temperature dependence of the relaxation rate of the electric current after application of an electric field
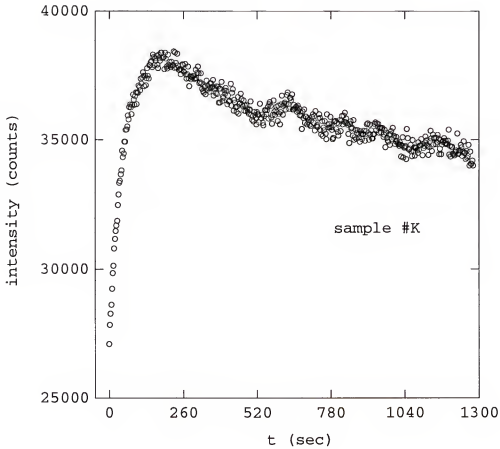
Figure 6-10 Intensity evolution of the CDW peak (13, -ε, -6.5) after the polarity of the applied electric field is changed. The applied field is 25 V/cm and the temperature is 18.9 K.

plotted versus temperature on a logarithmic scale. It is clear that the relaxation exponentially depends on temperature approximately, if not stronger.

Figure 6-10 shows the interesting evolution of the intensity after the polarity of the external field is changed. The intensity increases at beginning and then decreases monotonically. This indicates that the ordering of the CDW lattice first gets restored to some degree (it is far from being fully restored since the intensity is always much smaller than the intensity before any electric field is applied), and then the lattice get disordered again by the new field. This is not hard to understand if we draw an analogy to a spring: when we stretch it with a force larger than its critical force, a spring will deform a little. After this, if we begin to compress it, the deformation will become smaller first, and then gets larger if the compressing force is larger than the maximum load of the spring.

The more interesting phenomenon suggested by the figure, however, is the oscillations that coexist with the monotonic decay in the intensity. If these are not noise, it is possible that the increase in the beginning is just the first cycle of the oscillations, and the CDW lattice seems to do the following after the polarity change of the applied electric field: order-deform-order-deform- ····. Since the PSD only collects the photons in a certain region

near the CDW peak position, this could also correspond to an
oscillation in the peak position: as the spectra shift out
of the scanning region of the PSD, the intensity decreases;
when the spectra shift back toward the scanning region, the
intensity increases. We have seen similar phenomena in
figures 5-14 to 5-17, where the center of the spectrum
shifts to smaller Q when the applied field is small (e.g.,
E=170 mV/cm), and it shifts to higher Q when the field gets
larger (e.g., for E>1.36 V/cm). These data seem to suggest
that under one electric field, the change of the CDW
ordering may not be pure monotonic. Instead, it may change
through oscillations. This is certainly worthy further
investigations both experimentally and theoretically.

We did two experiments using synchrotron radiation to
study the kinetics of the CDW lattice disordering after
sudden application of an electric field. All the figures
presented so far are from the first experiment done on
beamline X20C in the National Synchrotron Light Source.
Figure 5-25 through 29 are the data taken during the second
trip to Brookhaven and the experiment was carried out on
beamline X16B, and the sample used during the second run was
sample #L, grown in the University of California at Los
Angeles.

Figure 6-11 shows the time dependence of the electric
current after a dc voltage of 15 V is applied in the chain
direction of the crystal at T=21.7 K. As in the case of
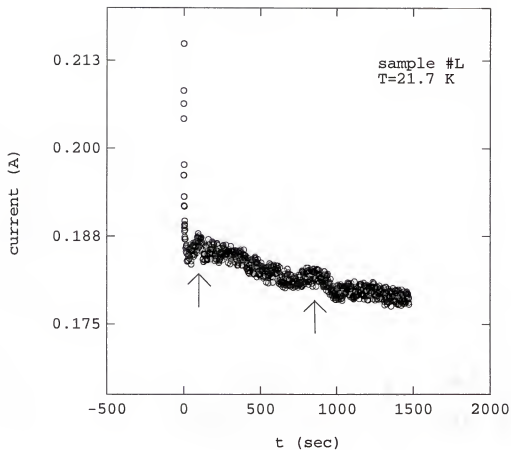
Figure 6-11 Time evolution of the electric current after application of a dc voltage of 15 V. Note the small bumps near the arrows.
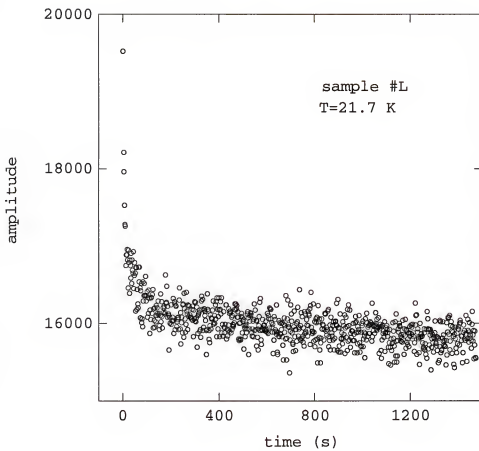
Figure 6-12   Time evolution of the scattering
amplitude after application of a dc voltage of
15 V.
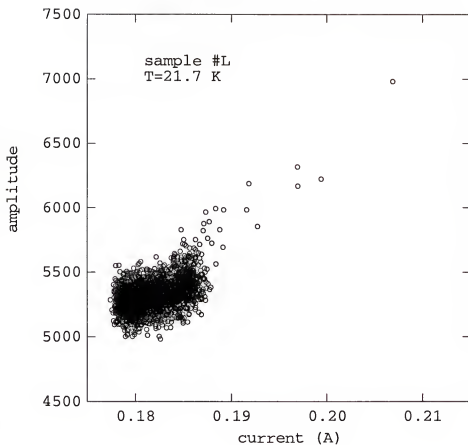
Figure 6-13 Scattering amplitude vs. current measured in-situ after application of a dc voltage of 15 V.

figure 6-5, the average electric current decreases in the course of time. However, in the present case, during the process of slow decreasing in the late times, there exist some fine structures, as indicated by the arrows in the figure. This is not understood at the present time.

Figure 6-12 plots the amplitude in the scattering profile, which is measured in-situ with the electric current shown in the previous figure. The behavior is similar to that of the intensity in figure 6-4. Figure 6-13 shows the scattering amplitude plotted vs. the electric current. Although the data are not very nice at extremely late times, the correlation is still undeniable. One thing to keep in mind is that what is plotted here is the peak amplitude, not the intensity as in figure 6-7. It is a quite different quantity.

Figure 6-14 shows the electric current measured at T=25.3 K after a dc voltage of 6 V is applied in the crystal chain direction. The data are very clean, showing the usual behavior: fast decrease in the beginning then slow decrease during a long period. However, there seems to be something slightly different in the present case: there are no oscillations in current! This is not true in reality because the data do have some noise in it. However, it is hard to understand why the oscillation amplitude is so small in this case (too hard even to extract the oscillations because the signal is very weak). Figure 6-14 also plots
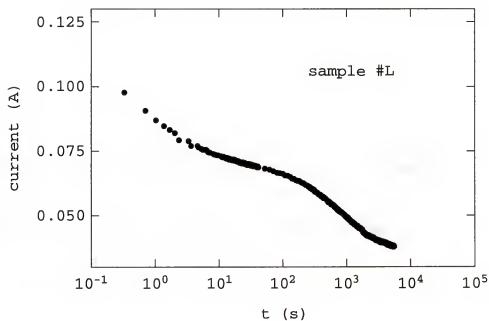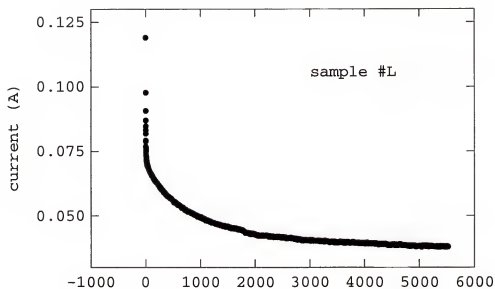
Figure 6-14 Time evolution of the electric current after appliction of a dc voltage of 6 V at 25.3 K.
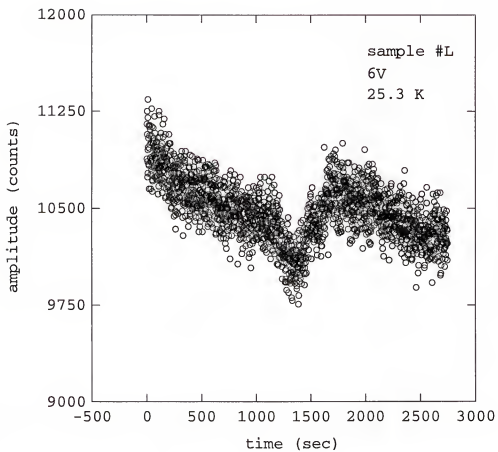
Figure 6-15 Time dependence of the scattering amplitude of the CDW peak $(13, -\epsilon, -6.5)$ after an electric field is applied.

the current vs. Ln(t). The curve clearly shows two time scales in the process.

A strange feature is shown by the data in figure 6-15, which plots the scattering amplitude measured in-situ as the electric current in figure 6-14. The early time behavior is normal in the sense that it monotonically decreases in time besides some noise. But near T=1000 sec, there is a giant jump in the amplitude, which lasted about 200 seconds. After this, the amplitude continues to drop in time. This peculiar phenomenon was never reported before. It is also very hard to understand. I think that it might be due to possible sample movement during the scanning process. This needs further experimental studies to verify whether it arises from experimental error or it has some intrinsic nature.

CHAPTER 7
CONCLUSIONS/FUTURE WORK

Through x-ray scattering experiments and electrical transport measurements, we find the following results:

1. Application of a dc electric field in the chain direction of blue bronze broadens the CDW scattering peak profiles along the chain direction and makes the lineshape split into two small peaks in the transverse direction that is perpendicular to the layers.

2. The CDW scattering lineshape of the disordered state suggests that the applied electric field breaks up the CDW condensate into micro domains in a transverse direction, and that two possibilities exist for the chain direction: either the coherence length gets shorter or the CDW domain gets smaller after application of a big dc field.

3. Electric fields of different polarities cause CDW peak profiles that are mirror images of each other.

4. Strong anharmonic interactions are needed to explain the peak splitting in the transverse direction using the Ginzburg-Landau free energy argument.

5. The time evolution of the CDW lattice disordering by an electric field is correlated with the transient of the bulk electric current. The change in both quantities arise from a polarization process.

6. CDW relaxation can not be described by a simple power law or a stretched exponential over the whole time domain the data were acquired. It can, however, be described very well by a percolation model, which assumes independent relaxations of different CDW domains.

For the future, there are a lot of work that need to be done. As we already mentioned in the previous chapter, one should further investigate the oscillations in the intensity when the polarity of the external field was reversed. The other thing one should do is to study the effects of impurities on the CDW peak lineshape and the relaxation, especially how they would affect the peak splitting observed in the transverse direction. Furthermore, one can study how the phonon spectra change after application of a field. It is believed that the Kohn anomaly observed above T_c completely softens and gives rise to long wavelength phasons as a result of long range order. But as observed in this work, the correlation length gets shorter in the chain direction after an electric field is applied and the long range order gets destroyed. Therefore, it is reasonable to expect the phonon spectra to change because of the field. Last of all, as strongly suggested by the kinetics studies of the present work, one can and should verify if other transport properties are due to structural disordering. For example, one can study the CDW response to an ac field; study the CDW relaxation after a temperature quench. These

areas so far have mainly been studied with transport measurements.

The present work also encourages researchers who have been working on spin density waves to search for correlations between the structural data (such as neutron scattering data) with transport measurements (such as magnetization experiments).

To conclude this dissertation, I would like to say that CDW systems remain to be a very active area currently. I has many sessions open during the APS March Meeting and there a lot of excellent work that are being done on these systems.

In the scattering cross section (3.4), besides the dominant term f_0, there are three other terms. The second term f_m given by (3.6) represents the contribution from the interaction between the magnetic field of the incident photon and the spin of the electrons in the solid [87]. This term gives an extra contribution to the total scattering cross section by having a cross term with the charge part if one ignores other terms (this is reasonable since other terms are normally very small compared with the charge part if the cross term does not vanish): $2|f_0 \cdot f_m|$. Such a term is smaller than the Thompson scattering by a factor of $\frac{\hbar \omega}{mc^2}$. Because of the factor i in front of (3.6), such an interference can occur only if the polarization factors are complex (circular polarization). A ferromagnet satisfies such a condition, and experiments have been done [88]. Since the magnetic peaks are at the same spots as the charge scattering, one can confirm the magnetic signal by changing the polarity of the externally applied magnetic field to see if the signal changes. If it does, the change will be purely from the magnetic moments.

When the charge component vanishes at some **K**, one is left with the other terms. These terms can be evaluated

alone. For example, when the incident photon energy is much
greater than the energy level separations $|E_a - E_c|$ of the
solid, it can be shown [59,89] that the contribution to the
scattering by these terms can be written as:

$$f_{mag} = i r_0 (\hbar\omega/mc^2) \left[\frac{1}{2}\mathbf{L(K)} \cdot \mathbf{A} + \mathbf{S(K)} \cdot \mathbf{B}\right] \tag{A1}$$

where $\mathbf{L(K)}$ and $\mathbf{S(K)}$ are the Fourier transform of the orbital
and spin angular momentum respectively; $\mathbf{A}$ and $\mathbf{B}$ are
functions of the polarization vectors of the incident and
the scattered photons.

The third term in (3.4) is often called the resonant
scattering since it can have a significant contribution to
the scattering when the denominator vanishes; i.e., when the
energy of the incident photon is equal to the energy
difference between two states of the solid. An extra term
Γ_c has been added to take into consideration of the fact
that the energy levels all have certain widths (as required
by the uncertainty principle), which eliminates the
singularity. When the incident photon energy satisfies this
special condition, this term can have a scattering intensity
as large as 1% of that of the Thompson scattering [90,91].
For an electric dipole transition, this term can be
simplified to the following [92,93,94]:

$$f_3^{res} = \frac{3}{4}\lambda\{\mathbf{e}_f^* \cdot \mathbf{e}_i [F_{11}^e + F_{1-1}^e] - i(\mathbf{e}_f^* \times \mathbf{e}_i) \cdot \hat{\mathbf{z}}_J [F_{11}^e - F_{1-1}^e]$$
$$+ (\mathbf{e}_f^* \cdot \hat{\mathbf{z}}_J)(\mathbf{e}_i \cdot \hat{\mathbf{z}}_J)[[2F_{10}^e - F_{1-1}^e - F_{11}^e] \tag{A2}$$

where $\mathbf{e}_f$ and $\mathbf{e}_i$ are the polarization vectors of the
scattered and the incident photons; the coefficients F_{LM}

(M=0,±1) depend on the radiative transition probability between a core level and an excited state (There are three major ways to eliminate the unstable state which is formed by exciting an electron from a core level to a higher energy level: radiative, Auger and Coster-Kronig deexcitations [95]).

To estimate the heating problem that might occur when
an electric field is applied, we assume a field of 10.2
V/cm, which corresponds to a voltage of 3 V and an current
of 7 μA:

The input heating power of the electric field is:

$Q_{in}=V \cdot I=3v \cdot (7.0 \times 10^{-6})A=36$ μW;

The cooling power by the thin copper wires affixed to the
sample is:

$Q_{out}=|\kappa \vec{\nabla} T|*A$

where κ is the thermal conductivity of copper, $\vec{\nabla} T$ is the
temperature gradient on the sample and A is the cross
section of the copper wires. Using 1K/cm for the
temperature gradient $|\vec{\nabla} T|$, $\kappa=3.85$ W/cm·°K for copper [21] and
$A=2\pi \times (0.0055$ cm$)^2=1.9 \times 10^{-4}$ cm^2 for the cross section of the
copper wires, one obtains:

$Q_{out}=(1K/cm) \times (3.85$ W/cm·°K$) \times (1.9 \times 10^{-4}$ cm$^2)=732$ μW

which is a factor of 20 more than the input heating power by
the electric field. Furthermore, this only takes into
account the cooling caused by the copper wires. In fact,
the sample was sitting on a sapphire rod, which is a very
good thermal conductor and probably conducts away a lot more
heat than the copper wires do during the process because it

has a much larger contact surface with the crystal (about a factor of thirty larger than the copper wires). So, overall speaking, heating should not be a problem in any of the above experiments. For the kinetics experiments, the heating problem was further dealt with by using He gas in the sample chamber to improve the thermal conduction.

APPENDIX C
FREE ENERGY ARGUMENT

The size of the shift for the case of domain boundary pinning can be obtained using the Ginzburg-Landau free energy argument [40,74,96]. The free energy of a CDW system in the presence of an external dc electric field should have three terms:

1> The first term is the elastic energy:

$$H_{elas} = \int dv \, \frac{\overline{v}_f}{2a_xa_y} [(\frac{\partial \phi}{\partial z})^2 + \frac{\xi_y^2}{\xi_z^2}(\frac{\partial \phi}{\partial y})^2 + \frac{\xi_x^2}{\xi_z^2}(\frac{\partial \phi}{\partial x})^2] \tag{C1}$$

where, $\overline{v}_f = \frac{\hbar v_f}{2\pi}$ with v_f being the Fermi wave vector of the system. Here, pure harmonic interactions are assumed, which we will see may not be quite accurate in these extremely anisotropic systems. The basic physics represented by this term is the following: the CDWs are ordered at a ground state before application of an electric field. If one suppresses the ions on a chain or moves one chain of ions relative to the neighboring chain using an electric field, there will be a restoring force due to the Coulomb interactions to pull the lattice back to the ground state. Equation (C1) assumes three elastic spring constants in the

162

three directions. These three directions can be thought as, in the case of blue bronze: the chain direction (the $\mathbf{b}^*$ direction), the normal direction to the layers (the $2\mathbf{a}^*-\mathbf{c}^*$ direction) and the direction perpendicular to these two (the $\mathbf{a}+2\mathbf{c}$ direction).

2> The second term in the free energy arises from the pinning potential of the impurities:

$$
\begin{aligned}
H_{imp} &= \sum_i \int dv \; V_{im}(\mathbf{r}-\mathbf{r}_i) \cdot \rho(\mathbf{r}) \\
&= \sum_i \rho_o \cdot V_{im}(\mathbf{r}-\mathbf{r}_i)\cos(\phi + \mathbf{Q}\cdot\mathbf{r}) \\
&= \int dv \; V_b(\mathbf{r})\cos(\phi + \mathbf{Q}\cdot\mathbf{r})
\end{aligned}
\tag{C2}
$$

where $V_b(\mathbf{r}) = \sum_i \rho_o \cdot V_{im}(\mathbf{r}-\mathbf{r}_i)$, and $V_{im}(\mathbf{r}-\mathbf{r}_i)$ is the impurity potential. $\rho(\mathbf{r})=\rho_o\cdot\cos(\phi + \mathbf{Q}\cdot\mathbf{r})$ is the charge density of the condensate (there is no need to consider the uniform charge distribution of the noncondensed electrons since it does not depend on ϕ). This term is just the electrostatic energy of the CDWs in the presence of an impurity (electric) potential.

3> The last term in the free energy is the contribution from the external electric field:

$$
H_{elec} = \int dv \; \frac{eE\phi}{\pi a_x a_y}
\tag{C3}
$$

where E is the total electric field acted on the condensed electrons. In low temeperatures, the screening by the free

electrons is small, E can be considered equal to the externally applied field.

Rescaling the spatial variables and the CDW wave vector as follows:

$$x \to \frac{\xi_x}{\xi_z}x, \quad y \to \frac{\xi_y}{\xi_z}y \text{ and } Q_x \to \frac{\xi_z}{\xi_x}Q_x', \quad Q_y \to \frac{\xi_z}{\xi_y}Q_y'$$

and the system Lagrangian can be written as (note: despite these variable changes, the scalar product of $\mathbf{Q}$ and $\mathbf{r}$ does not change under the transformation):

$$L(\phi) = \frac{\xi_x \xi_y}{\xi_z^2} \int dv \{ \frac{v_f}{2a_x a_y}(\frac{m^* \dot\phi^2}{mv_f^2} - |\nabla\phi|^2) - V_b(\mathbf{r})\cos(\phi + \mathbf{Q}' \cdot \mathbf{r}) + \frac{eE}{\pi a_x a_y} \} \qquad (C4)$$

which yields the following equation of motion:

$$\alpha\dot\phi + \beta\ddot\phi + \nabla^2\phi - \frac{a_x a_y}{\overline{v}_\ell}V_b(\mathbf{r})\sin(\phi + \mathbf{Q} \cdot \mathbf{r}) = \frac{eE}{\pi\overline{v}_\ell} \qquad (C5)$$

where a damping term has been added.

The term containing $\ddot\phi$ can be shown to be negligible [97]. For a given electric field E, the damping term is position independent if we assume that the electrical contacts are perfect or the electric current flow is completely uniform. With this simplifying condition, the equation of motion becomes the following:

$$\nabla^2\phi - \frac{a_x a_y}{\overline{v}_\ell}V_b(\mathbf{r})\sin(\phi + \mathbf{Q} \cdot \mathbf{r}) = f(E) \qquad (C6)$$

where $f(E) = \frac{eE}{\pi\overline{v}_\ell} - \alpha\dot\phi$ is a position independent function if one assumes a uniform current flow throughout the sample. This function f(E) is actually the phase-slip voltage except for

a term which arises from impurity pinning and is proportional to the threshold field, $\dfrac{eE_T}{\pi \overline{v}_f}$ [77]. The above equation should be solved with a boundary condition: $\phi|_\Sigma$ $=g(\mathbf{r})|_\Sigma$.

To solve the above equation, people usually assume that the impurity potential is short ranged and can be replace by a δ function. This treatment becomes more accurate in high temperatures as the screening to the potential by normal electrons becomes stronger. To do a crude estimate, we use such a simplification. So,

$$V_b(\mathbf{r}) = V_o \sum_i \delta(\mathbf{r} - \mathbf{r}_i)$$

With this, one can rewrite the second term in equation (5) as follows:

$$
\begin{aligned}
&-\frac{a_x a_y}{\overline{v}_f} V_b(\mathbf{r}) \sin(\phi + \mathbf{Q} \cdot \mathbf{r}) \\
&= -\frac{a_x a_y V_o}{\overline{v}_f} \sum_i \delta(\mathbf{r} - \mathbf{r}_i) \cdot \sin[\phi(\mathbf{r}_i) + \mathbf{Q} \cdot \mathbf{r}_i] \\
&= -\frac{a_x a_y V_o}{\overline{v}_f} \sum_i \nabla^2 \frac{-1}{4\pi|\mathbf{r} - \mathbf{r}_i|} \cdot \sin[\phi(\mathbf{r}_i) + \mathbf{Q} \cdot \mathbf{r}_i] \\
&= \nabla^2 \{ \frac{a_x a_y V_o}{4\pi \overline{v}_f} \sum_i \frac{\sin[\phi(\mathbf{r}_i) + \mathbf{Q} \cdot \mathbf{r}_i]}{|\mathbf{r} - \mathbf{r}_i|} \} \\
&= \nabla^2 h(\mathbf{r})
\end{aligned}
$$

This allows us to write eqn. (5) in a more compact form:

$$\nabla^2 \Phi = f(E)$$

with boundary condition $\Phi|_\Sigma = \{ h(\mathbf{r})|_\Sigma + g(\mathbf{r}) \}|_\Sigma = u(\mathbf{r}) \}|_\Sigma$, and

$$\Phi = h(\mathbf{r}) + \phi(\mathbf{r})$$

The solution to Φ inside a domain can be written using the Green's function as the following:

$$\Phi(\mathbf{r}) = \int_v G(\mathbf{r}, \mathbf{x}) \cdot g(E) d^3 x - \frac{1}{4\pi} \iint_\Sigma u(\mathbf{x}) \cdot \frac{\partial}{\partial n} G(\mathbf{r}, \mathbf{x}) dS_x$$

where the Green's function $G(\mathbf{r}, \mathbf{x})$ is given by the following:

$$\begin{cases} \nabla^2 G(\mathbf{r}, \mathbf{x}) = 4\pi\delta(\mathbf{r} - \mathbf{x}) \\ G(\mathbf{r}, \mathbf{x})|_{\mathbf{x} \in \Sigma} = 0 \end{cases}$$

If we assume a rectangular shape for the CDW domains, the Green's function is simply:

$$G(x, x') = \frac{32}{\pi abc} \times \sum_{l,m,n=1}^{\infty} \frac{\sin(l\pi x'/a) \cdot \sin(l\pi x/a) \cdot \sin(m\pi y'/b) \cdot \sin(m\pi y/b) \cdot \sin(n\pi z'/c) \cdot \sin(n\pi z/c)}{l^2/a^2 + m^2/b^2 + n^2/c^2}$$

For small electric fields, we ignore the change of the phase on impurity sites since they are smaller than that in the other region (This is not a very accurate approximation because as long as $E > E_T$, the CDW will be depinned and its phase of course does change everywhere in time. However, the spatial variation of the phase is certainly smaller at the impurity sites due to pinning). So we only consider the change of the phase due to the applied electric field E:

$$\Delta\phi(\mathbf{r}) = \Phi(E) - \Phi(0)$$

$$= \int_v G(\mathbf{r}, \mathbf{x}) \cdot g(E) d^3 x$$

$$= \frac{256 \cdot g(E)}{\pi^4} \times \sum_{l,m,n=odd}^{\infty} \frac{\sin(l\pi x/a) \cdot \sin(m\pi y/b) \cdot \sin(n\pi z/c)}{lmn(l^2/a^2 + m^2/b^2 + n^2/c^2)}$$

The change in the wave vector is: $\Delta \mathbf{Q} = \nabla \Delta \phi(\mathbf{r})$. This allows us to calculate the line shape of the profile:

$$S(\mathbf{q}) \propto A \cdot \int \exp\left(-\frac{[\mathbf{q} - \Delta \mathbf{Q}(\mathbf{r})]^2}{\sigma^2}\right) d^3Q$$

where we have used a gaussian. One can choose a lorentzian or other canonical functions.

ACQUISITION PROGRAMS

Many programs are written to control the instruments used in this work and to analyze the data. Most of the controlling programs were written in ASYST, a semi-assembly language. They mainly control the following instruments: keithly multimeters, wide-wave function generator, lakeshore temperature controller. Although several programs written for the Ortec counter/timer and the Klinger MC-4 stepping motor controller are not used for data acquisition in this work, they are also listed in this appendix for future reference. These programs work very well with low resolution set-up of the diffractometer, but with the high resolution, they are not much faster than the C programs which have been used for a long time in our laboratory. The PSD controller (PAR 1461) is also controlled by programs written in ASYST. Some of the programs are listed in the dissertation of Curtis R. Harkless and they are not cited here. The following briefly discusses some of the ASYST programs I write for instrument controls. I-V

This function does a DC current-voltage curve measurement. It uses two Keithly multimeters as a voltmeter and an ammeter respectively.

get-I-T

    This function records the temperature and the electric current. It uses a Lakeshore 81-C controller to measure the temperature, and a Keithly multimeter to record the electric current (or voltage). This program is used in this work to trace any change in temperature and the electric current in sample after sudden application of an electric field.

look

    This function plots the measured result of the current-voltage curve on the computer screen.

start-func

    This function sets up the wide wave function generator in the mode of dc voltage.

appl_3V

    This function causes a 3 V voltage output of the function generator.

basic-array

    This function converts an ASCII data file "basic.ary" (which only consists of numbers) into an ASYST array, called "data".

    The following is the code written in ASYST. The field is called current.pgm.

File: Current.pgm

```
dp.real dim[ 2501 ] array Vsampl
dp.real dim[ 201 ] array Isampl
real dim[ 512 ,512 ] array DATA
dp.integer scalar M
dp.integer scalar N
dp.real scalar voltage
dp.real scalar increment
dp.integer scalar NP
64 string response
20 string file
dp.real scalar temper
6 string tempor

15 gpib.device function
13 eos.character
eos.on
eoi.on
3000 timeout

12 gpib.device lake
13 eos.character
eos.on
eoi.on
30000 timeout

20 gpib.device keithA
13 eos.character
eos.on
eoi.on
10000 timeout

29 gpib.device keithV
13 eos.character
eos.on
eoi.on
10000 timeout


: I-V
send.interface.clear
remote.enable.on
\ cr ." How many points do you want to have in the IV curve? " cr cr
\ #input NP := cr cr
cr ." input the highest voltage you wanna go here:" cr
." Voltage maximum=" #input dup voltage := cr
\ NP 1. * 4. / / increment :=
200. 1. * 4. / / increment :=
keithV
" R3X" gpib.write
voltage 16 > if " R4X" gpib.write then
" G1X" gpib.write
keithA
" R1X" gpib.write
cr ." Do you think the current may exceed 200 micro-amperes? (y/n)" cr
"input
" yY" "within if " R4X" gpib.write then
cr
" G1X" gpib.write
function
```

```
" fnc 0" gpib.write
0 voltage :=
stack.clear

cr ." here are all the dciv data files" cr " dir dciv*.dat" "exec cr cr
cr
cr ." Please give the output file a name here w/ prefix DCIV like
dciv001.dat:"
cr cr "input
" defer> out>file" "exec
cr ." The time is now" 3 spaces "time "type 3 spaces "date "type
cr
cr
." voltage" 3 spaces ." KeithV" 2 spaces
." KeithA" cr cr

NP 2 + 1 do
function
" ofs 0" gpib.write
4000 msec.delay
" ofs " voltage "." "cat gpib.write
1500 msec.delay
-1 4 fix.format
cr voltage . 2 spaces
16 10 fix.format
voltage increment + voltage :=

keithV
response gpib.read

response "len 5 < if
response gpib.read then

response 32 "number Vsampl [ I ] :=
Vsampl [ I ] .   3 spaces

keithA
response gpib.read

response "len 5 < if
response gpib.read then

response 32 "number Isampl [ I ] :=
Isampl [ I ] . CR
I 49 > if
increment abs -1. * increment := then
I 149 > if
increment abs increment := then
stack.clear
loop
out>file.close
cr ." I-V measurement done. Results are in the last file below:"
" d dir c:\asyst\dciv*.dat" "exec
cr
cr
cr cr ." Type look to see the I-V curve" cr cr cr
console
;


: get_i_T
send.interface.clear
remote.enable.on
keithV
" G1X" gpib.write
```

```
" R1X" gpib.write
stack.clear

cr ." here are all the current data files" cr " dir curn*.dat" "exec cr
cr cr
cr ." Please give the output file a name here w/ prefix CURN like
curn001.dat:"
cr cr "input
" defer" out>file "exec
cr ." The time is now" 3 spaces "time "type 3 spaces "date "type
cr
cr
25 1 do
16 10 fix.format
keithV
response gpib.read

response "len 5 < if
response gpib.read then
0
response 32 "number Vsampl [ I ] :=

lake
response gpib.read

response "len 5 < if
response gpib.read then
0
response tempor ":= tempor 32 "number temper :=
response gpib.read
"time "type 5 spaces Vsampl [ I ] . temper . cr
stack.clear
1000 msec.delay
loop
out>file.close
cr ." voltage on the 10k ohms resistor are in the last file below:"
" dir c:\asyst\curn*.dat" "exec
console
;

: look
dotted
Vsampl Isampl xy.auto.plot
;

: start-func
function
" ifc" gpib.write
" dcl" gpib.write
" sdc" gpib.write
" llo" gpib.write
CR CR CR
." The functional generator is ready to take your commands now. Please:"
CR CR
;

: appl_3V
out>file func.out
start-func
" fnc 0"
cr ." the time now is:" rel.time 1200000 / . cr
" ofs 3" gpib.write
CR ." the time now is:" rel.time 1200000 / . CR
." and 0.3v applied now" CR
cr 1200000 msec.delay CR
```

```
CR ." the time now is:" rel.time 1200000 / . CR
." field off now" CR
out>file.close
;

: BASIC-ARRAY
BASIC.OPEN BASIC.ARY
1 M :=

BEGIN
BASIC.READ
N :=
N 0 <> IF
N .
N 1 + 1 DO
    DATA [ M , N I - 1 + ] :=
LOOP
M 1 + M :=
THEN
?BASIC.EOF
UNTIL

BASIC.CLOSE
;
```

APPENDIX E
RESOLUTION EFFECTS

During the discussion of figures 5-1 and 5-2, I claim that the difference in the peak widths between the Bragg peak and the CDW peak along the chain direction is due to the resolution effect, but in the (2a*-c*) direction, the difference cannot be a pure resolution effect. Let us explore this argument here.

The system resolution depends on many things: beam size, beam divergence, mosaic spread and Darwin widths of the monocromator and the analyzer crystals [98,99]. For a well collimated beam (by using slits and long beam path, say), if one uses GE or Si crystals as the monocromator and the analyzer, the major factor in the system resolution is the Darwin width of these crystals. In this case, the system resolution depends on the magnitude of the scattering vector, as shown in figure E-1, where the HWHM of the system resolution is plotted in two directions, one of which is parallel to the scattering wave vector $\mathbf{Q}$, and the other is perpendicular to $\mathbf{Q}$. Figure E-1 is for the case of a Cu K_α^1 rotating anode source (x-ray wave length is 1.5402 $\overset{\circ}{A}^{-1}$) and a triple axis diffractometer (which we will use for the discussion below).
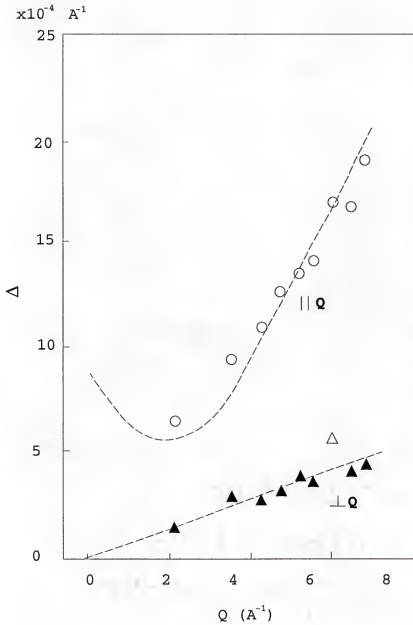
Figure E-1 Resolution widths (HWHM) vs. magnitude
of the scattering vector **Q** with perfect Ge (111)
crystals as the monochromator and the analyzer. The
circles and triangles are experimental data.   The
curves are predictions using a Darwin width which
is 30% larger than the theoretical value, 0.0043^0.

Figure 5-1 and 5-2 compare the Bragg peak (14,2,-7) and the CDW peak (15,-0.7447,-7.5). These two vectors have approximately the same magnitude ($Q_{Bragg} \approx 5.7$ $\overset{\circ}{A}^{-1}$; $Q_{CDW} \approx 5.9$ $\overset{\circ}{A}^{-1}$). From figure E-1, one can see that the resolution widths at these two scattering vectors are approximately the same. We shall use $\Delta Q_{//}$ and $\Delta Q_{\perp}$ for the resolution widths along $\mathbf{Q}$ and perpendicular to $\mathbf{Q}$ respectively. Assuming that the widths of the Bragg peak solely arise from the system resolution, we can calculate $\Delta Q_{//}$ and $\Delta Q_{\perp}$ using the measured widths of the Bragg peak. Figure E-2 shows the resolution ellipse in the plane containing the b* and the (2a*-c*) directions in reciprocal space near a peak (2q·cosα ,qsinα ,-qcosα), where q is the magnitude of the scattering wave vector $\mathbf{q}$ and α is the angle of $\mathbf{q}$ relative from the (2a*-c*) direction. The measured HWHM of this peak in the b* direction is represented by ΔQ_{b*} in figure E-2. ΔQ_{b*} is related to the resolution widths through the equation of the ellipse:

$$\frac{\Delta Q_{b*}^2 \cos^2 \alpha}{\Delta Q_{//}^2} + \frac{\Delta Q_{b*}^2 \sin^2 \alpha}{\Delta Q_{\perp}^2} = 1 \qquad (E1)$$

where the angle α is the angle of the scattering wave vector relative to the (2a*-c*) direction, as shown in figure E-2. Equation (E1) yields an expression for the measured width of the peak (2q·cosα ,qsinα ,-qcosα) in the
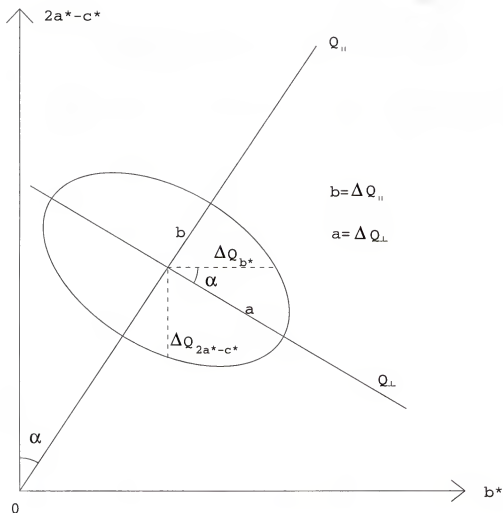
Figure E-2 Resolution ellipse in reciprocal space on the plane containing the (2a*-c*) and the b* directions. The major and the minor axes of the ellipse a and b are the system resolution widths in the transverse and the radial directions.

b* direction in terms of the resolution widths and the angle
α :

$$\Delta Q_{b*} = \frac{\Delta Q_\perp \cdot \Delta Q_{//}}{\sqrt{\Delta Q_\perp^2 \sin^2 \alpha + \Delta Q_{//}^2 \cos^2 \alpha}} \qquad \text{(E2)}$$

Similarly, the measured width in the (2a*-c*) direction
is given by the following (changing α to $\alpha + \pi/2$ in eqn.
E2):

$$\Delta Q_{2a*-c*} = \frac{\Delta Q_\perp \cdot \Delta Q_{//}}{\sqrt{\Delta Q_{//}^2 \sin^2 \alpha + \Delta Q_\perp^2 \cos^2 \alpha}} \qquad \text{(E3)}$$

Equations (E2) and (E3) enable us to get $\Delta Q_{//}$ and $\Delta Q_\perp$
using the data taken on the Bragg peak (14,2-7) in the case
of figures 5-1 and 5-2 if we include the finite-grain-size
effect in the system resolution. The measured widths of
this Bragg peak are $\Delta Q_{b*}=3.7\times10^{-4}$ $\overset{\circ}{A}{}^{-1}$ and $\Delta Q_{2a*-c*}=7.7\times10^{-4}$ $\overset{\circ}{A}{}^{-1}$,
and the angle

$$\alpha = \tan^{-1}\left(\frac{2 b*}{5.7 \overset{\circ}{A}{}^{-1}}\right) = \tan^{-1}\left(\frac{2 \times 0.83 \overset{\circ}{A}{}^{-1}}{5.7 \overset{\circ}{A}{}^{-1}}\right) = 16.23° \qquad \text{(E4)}$$

Substituting these values into eqn. (E2) and (E3) yields the
following:

$$\Delta Q_{//} \approx 9.3\times10^{-4} \overset{\circ}{A}{}^{-1} ; \quad \Delta Q_\perp \approx 3.6\times10^{-4} \overset{\circ}{A}{}^{-1} \qquad \text{(E5)}$$

With these values, we can calculate the resolution-
caused widths in the zero field scattering profile of the
CDW peak (15,-0.7445,-7.5) by simply setting α to be $-6.1°$
in equations (E2) and (E3), and using eqn. (E5). The result
is that the scattering profile of the CDW peak, due to the
system resolution alone, will have a width of $HWHM_{b*}=3.6\times10^{-4}$

$\overset{\circ}{A}{}^{-1}$ in the b* direction, and a width of $HWHM_{2a*-c*}=9.0\times10^{-4}$ $\overset{\circ}{A}{}^{-1}$ in the (2a*-c*) direction. The measured values shown by figure 5-1 and 5-2 are, $HWHM_{b*}=3.5\times10^{-4}$ $\overset{\circ}{A}{}^{-1}$ in the b* direction, and $HWHM_{2a*-c*}=1.9\times10^{-3}$ $\overset{\circ}{A}{}^{-1}$. So, in the chain direction, the width of the scattering profile is completely due to the system resolution and finite grain size; while in the (2a*-c*) direction, there are other effects contributing to the width of the profile.

REFERENCES

1   R. E. Peierls, *Quantum Theory of Solids*, ed. by N. F. Mott and E. C. Bullard (Oxford, Clarendon Press, 1955)

2   H. Frohlich, Proc. Royal. Soc. A**223**, 296 (1954) (proposed CDW superconducting)

3   P. Monceau, *et al.*, Phys. Rev. B., **25**, 931 (1982)

4   A. Zettl, *et al.*, Phys. Rev. B.,**26**, 5760 (1982) and A. Zettl, *et al.*, Phys. Rev. B.,**26**, 5773 (1982)

5   J. Dumas *et al.*, Phys. Rev. Lett., **50**, 757 (1983)

6   S. Tomic, *et al.*, Solid State Commun., **38**, 109 (1981)

7   R. Brusetti, *et al.*, *Recent Development in Condensed Matter Physics*, Vol. 2, ed. by J.T. Devreese, *et al.* (Plenum Press, New York, 1981)

8   A. Briggs, *et al.*, J. Phys. C, **13**, 2117 (1980)

9   R. M . Fleming, D.E. Moncton, and D.B. McWhan, Phys. Rev. B **18**, 5560 (1978)

10 R. M . Fleming, L. F. Schneenmeyer, D.E. Moncton, Phys. Rev. B **31**, 899 (1985)

11 J.P. Pouget and R. Comes, in *Charge Density Waves in Solids*, ed. by L. Gor'kov and G. Gruner (Amsterdam, the Netherlands, 1989).

12 G. Travaglini, *et al.*, Solid State Commun. **37**, 599 (1981)

13 J. Y. Veuillen, *et al.*, Solid State Commun. **63**, 587 (1987)

14 S. Girault, *et al.*, Phys. Rev. B **38**, 7980 (1988)

15 J.P. Pouget, *et al.*, J. Physique **46**, 1731 (1985)

16 T. Tamegai, *et al.*, Solid State Commun. **56**, 13 (1985)

17   R.M. Fleming, R. G. Dunn and L. F. Schneenmeyer, Phys
      Rev. B, **31**, 4099 (1985)

18   R.G. Palmer, *et al.*, Phys. Rev. Lett. **53**, 958 (1984)

19   L. Mihaly and G.X. Tessema, Phys. Rev. B.**33**, 5858
      (1986)

20   L. Mihaly, K. B. Lee and P. W. Stephens, Phys.   Rev.
      B, **36**, 1793 (1987)

21   N. W. Ashcroft and N. D. Mermin, *Solid State Physics*,
      (Saunders College, Philadelphia, PA, 1976)

22   J. Solyom, Adv. Phys. **28**, 101 (1979)

23   V.J. Emery in: *Highly Conducting One Dimensional.
      Solids,* ed. by J. T. Devreese, *et al.* (Plenum Press,
      New York, 1979)

24   J. W. Lynn, *et al.*, Phys. Rev. B, **12**, 1154 (1975)

25   M. Sato, H. Fujishita and S. Hoshino, J. Phys. C:
      16, L877 (1983)

26   B. Renker, *Et al.*, Phys. Rev. Lett. **32**, 836 (1974)

27   P. Butaud, *et al.*, Phys. Rev. Lett, **55**, 253 (1985)

28   D.S. Perloff, *et al.*, J. Phys. Chem. Solids **30**, 1071
      (1969)

29   A. Meerschaut, *et al.*, Acta Crystallogr. Sect. B **35**,
      1747 (1979)

30   C. Roucau, *et al.*, Phys. Status Solidi **62**, 483 (1980)

31   P. Haen, *et al.*, Lect. Notes Phys. **95**, 323 (1978)

32   J. Chaussy, *et al.,* Solid State Commun. **20**, 759 (1976)

33   N.P. Ong and J.W. Brill, Phys. Rev. B **18**, 5265 (1978)

34   P.A. Lee, T.M. Rice and P.W. Anderson, Solid State
      Commun., **14**, 703 (1974)

35   Escribe-Filippini, et al.,Synth. Met. **19**, 931 (1987)

36   J. P. Pouget: *Low-dimensional Electronic Properties
      of Molybdenum Bronzes and Oxides,* ed. by Claire
      Schlenker (Kluwer, Dordrecht, 1989).

37   G. Travaglini, I. Morke and J.B. Torrance, Solid State Commun. **45**, 289 (1983)

38   G. Mozurkewich and G. Gruner, Phys. Rev. Lett **51**, 2206 (1983)

39   P.B. Littlewood, in *Charge Density Waves in Solids,*331, ed. by L. Gor'kov and G. Gruner (Amsterdam, the Netherlands, 1989)

40   H. Fukuyama and P.A. Lee, Phys. Rev. B **17**, 535 (1978)

41   C.H. Chen, L.F. Schneemeyer, R.M. Fleming, Phys. Rev. B, **29**, 3765 (1984)

42   S.M. DeLand, *et al.*, Phys. Rev. Lett **66**, 2026 (1991)

43   G. Mihaly and P. Beauchene, Solid State Commun., **63**, 911 (1987)

44   R.M. Fleming, *et al.*, Rev. B, **33**, 5450 (1986)

45   Z.Z. Wang, *et al.*, J. Phys. Lett. **44**, L-311 (1983)

46   A. Janossy, G. Mihaly & G. Kriza, Solid. State Commun. **51**, 63 (1984)

47   R.M. Fleming and C.C. Grimes, Phys. Rev. Lett. **42**, 1423 (1979)

48   A. Zettl, and G. Gruner, Phys. Rev. B **29**, 755 (1984)

49   H. Mutka, *et al.*, J. Physique **48**, 425 (1987)

50   L. Mihaly and G. Gruner: *Nonlinearity in Condensed Matter*, ed. by A.R. Bishop, *et al.*, Springer Series in Solid-State Sciences, **69**, 308 (1987)

51   W.Y. Wu, *et al.*, Phys. Rev. B **33**, 2444 (1986)

52   K. Yamaya and Y. Abe, Mol. Cryst. & Liq. Cryst. **81**, 133 (1982)

53   H. Mutka, *et al.*, J. Physique Lett. **45**, L-113 (1984)

54   H. mutka, *et al.*, Mol. Cryst. Liq. Cryst. **121**, 133 (1985)

55   L. C. Bourne and A. Zettl, Solid State Commun. **60**, 789 (1986)

56   J. Graham and A.D. Wadsley, Acta Cryst. **20**, 93 (1966)

57   M.H. Wangbo and L.F. Schneemeyer, Inorg. Chem. **25**, 2424 (1986)

58   K. Tsutsumi, *et al.* in *Charge Density Waves in Solids*, ed. by Gyula Hutiray and Jeno Solyom (Springer-Verlag, Berlin, Heidelberg, 1985)

59   M. Blume, J. Appl. Phys. **57**, 3615 (1985)

60   G. Baym, *Lectures on Quantum Mechanics*, (Benjamin /Cummings Publishing Company, Menlo Park, CA, 1973)

61   E. Merzbacher, *Quantum Mechanics*, (John Wiley and Sons, Inc., New York, 1961)

62   B.E. Warren, *X-ray Diffraction*, page 252 (Addison-Wesley Publishing Company, Reading, MA, 1969)

63   P. Scherrer, *Nachr. Gottinger Gesell.*, 98 (1918); *Zsigmondy's Kolloidchemie*, 3rd Ed., p. 394

64   A. Guinier, *X-ray Diffraction*, (W.H. Freeman and Company, San Francisco, 1963)

65   W.L. Bragg, *The crystalline State*, **1**, P. 189 (Bell, London, 1919)

66   E. Bertaut, in *International Tables for X-ray Crystallography*, **III**, page 318, edited by C.H. Macgillavry and G.D. Rieck (D. Reidel Publishing Company, Boston, USA, 1983)

67   S. Girault, A.H. Moudden and J.P. Pouget, Phys. Rev. B **39**, 4430 (1989)

68   G.F. Giuliani and A.W. Overhauser, Phys. Rev. B **26**, 1660 (1982)

69   L.V. Keldysh and Yu.V. Kopaev, Fiz. Tverd. Tela **6**, 2791 (1964)

70   B. Horovitz, H. Gutgreund and M. Weger, Solid State Commun. **39**, 541 (1981)

71   D.S. Perloff and A. Wold, J. Phys. Chem. Solids, Suppl. **28**, 361 (1967)

72   G. Bang and G. Sperlich, Z. Phys. B **22**, 1 (1975)

73   G.D. Rieck, in *International Tables for X-ray Crystallography*, **III**, page 59, edited by C.H. Macgillavry and G.D. Rieck (D. Reidel Publishing Company, Boston, USA, 1983)

74   P.A. Lee and T.M. Rice, Rev. B, **19**, 3970 (1979)

75   S.N. Coppersmith, Phys. Rev. Lett. **65**, 1044 (1990)

76   D. DiCarlo, *et al.*, Phys. Rev. Lett. **70**, 845 (1993)

77   S. Ramakrishna, *et al.*, Phys. Rev. Lett. **68**, 2066 (1992)

78   P. Heller and G.B. Benedek, Phys. Rev. Lett. **8**, 428 (1962)

79   H. Eugene Stanley, *Introduction to Phase Transitions and Critical Phenomena*. (Oxford University Press, New York) (1971).

80   S. Girault, A.H. Moudden and J.P. Pouget, Phys. Rev. B **39**, 4430 (1989)

81   S.E. Barnes and A. Zawadowski, Phys. Rev. Lett. **51**, 1003 (1983)

82   I. Tutto and A. Zawadowski, Phys. Rev. B. **32**, 2449 (1986)

83   L. Mihaly and G.X. Tessema, Physical. Review B, **33**, 5858 (1986)

84   R. V. Chamberlin and D. N. Haines, Phys. Rev. Lett., **65**, 2197 (1990)

85   R. V. Chamberlin and F. Holtzberg, Phys. Rev. Lett., **67**, 1606 (1991)

86   T.C. Lubensky and A. McKane, J. Phys. A : Math. Gen. **14** L157 (1981)

87   P.M. Platzman and N. Tzoar, Phys. Rev. B **2**, 3566 (1970)

88   K. Namikawa, *et al.*, J. Phys. Soc. of Japan **54**, 4099 (1985)

89   M. Blume and D. Gibbs, Phys. Rev. B, **37**, 1779 (1988)

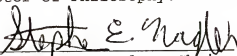90   D.B. McWhan, *et al.*, Phys. Rev. B. **42**, 6007 (1990)

91   E.D. Isaac, *et al.*, Phys. Rev. Lett. **62**, 1671 (1983)

92   G.T. Trammell, Phys. Rev. **126**, 1045 (1962)

93   J.P. Hannon, *et al.*, Phys. Rev. Lett. **61**, 1245 (1983)

94   J.P. Hannon and G.T. Trammell, Phys. Rev. **186**, 306 (1969)

95   Keski-Rahkonen and Krause, Atomic Data and Nulcear Data Tables, **14**, No. 2, 140 (1974)

96   F.Ya. Nad', in *Charge Density Waves in Solids,* ed. by L. Gor'kov and G. Gruner (Amsterdam, the Netherlands, 1989).

97   S.N. Coppersmith and P. B. Littlewood in *Charge Density Waves in Solids,* ed. by Gyula Hutiray and Jeno Solyom (Springer-Verlag Berlin Heidelberg 1985)

98   C.A. Lucas, E. Gartstein and R.A. Cowley, Acta Cryst. A**45**, 416 (1989)

99   R.A. Cowley, Acta Cryst. A **43**, 825 (1987)

BIOGRAPHICAL SKETCH

Junqing Zhang was born into a farmer's family in China in April 1966, when the Great Culture Revolution started. His childhood was not quite pleasant because his family was poor. Besides math, he was also taught how to become a good child of Chairman Mao during his elementary school. Although his parents sent him to school with only one wish that he would not be cheated in the free markets when he grew up, he greatly surprised them in 1983: he was admitted into one of the top five universities in China, Nankai University, where he received his BS degree in electronics in 1987 and came to Florida the same year to pursue a Ph.D. degree in physics through the CUSPEA program.

Junqing loves Florida: the palm trees, the beautiful beaches, etc. Despite the famous Disney World in Orlando, Gainesville, the quiet, clean and friendly little city, is his favorite place in Florida. Here, he has many dear friends and good memories. Looking back at the six years in Gainesville, he sees smiles and tears, efforts and failures, satisfaction and disappointment. Overall, he is very thankful to the Lord for leading him through this special period of his life.

I certify that I have read this study and that in my opinion it conforms to acceptable standards of scholarly presentation and is fully adequate, in scope and quality, as a dissertation for the degree of Doctor of Philosophy.

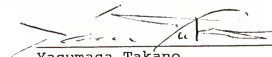Stephen E. Nagler, Chair
Professor of Physics

I certify that I have read this study and that in my opinion it conforms to acceptable standards of scholarly presentation and is fully adequate, in scope and quality, as a dissertation for the degree of Doctor of Philosophy.

Neil S. Sullivan
Professor of Physics

I certify that I have read this study and that in my opinion it conforms to acceptable standards of scholarly presentation and is fully adequate, in scope and quality, as a dissertation for the degree of Doctor of Philosophy.

James W. Dufty
Professor of Physics

I certify that I have read this study and that in my opinion it conforms to acceptable standards of scholarly presentation and is fully adequate, in scope and quality, as a dissertation for the degree of Doctor of Philosophy.

Yasumasa Takano
Associate professor of Physics

I certify that I have read this study and that in my opinion it conforms to acceptable standards of scholarly presentation and is fully adequate, in scope and quality, as a dissertation for the degree of Doctor of Philosophy.

Christopher Batich
Professor of Materials Science and Engineering

This dissertation was submitted to the Graduate Faculty of the Department of Physics in the College of Liberal Arts and Sciences and to the Graduate School and was accepted as partial fulfillment of the requirements for the degree of Doctor of Philosophy.

December, 1993

_____
Dean, Graduate School